Universitat Politécnica de Valencia
Escuela Superior de Ingeniería de Diseño
Von Karman Institute for Fluid Dynamics

Development of a selective Proper Orthogonal Decomposition for post-processing unsteady flows in turbomachinery

Master Thesis
Master Degree in Aeronautics

Author: Adrián Hernández Forte
Supervisor: Pr. Fabrizio Fontaneto

Valencia, September 2019

Abstract

Nowadays, the progress in technology has made possible increase the computational power and thus it has made possible the improvement of flow solvers. This allows to compute with higher spatial and temporal resolutions as well as save a larger quantity of variables. This together with the Big-Data revolution, also present in the experimental field, has created a necessity of post-processing techniques. These are essential in order to treat such a quantity of data.

Data-driven decompositions have become one of the most common methods. These can be used in experimental or numerical cases in fluid dynamics, with the main purpose of identifying coherent structures, patterns or building reduced order models (ROM). The identification of patterns is interesting from the point of view of the turbulence. A flow of this type is composed by eddies and also by characteristic structures in specific regions of the domain such as walls. On the other hand, the possibility of building models with reduced degrees of freedom makes easier the analysis of results, independtly if the source of the data is an experiment or a CFD simulation.

The decomposition is made via projecting the data into a series of temporal and spatial basis, also called modes, that are computed following different criteria. In this project, the novel technique called Multi-scale Proper Orthogonal Decomposition (mPOD) has been developed. This derives from the Proper Orthogonal Decomposition (POD) which is a energy-based technique. In POD the modes obtained in the decomposition are optimal in terms of energy content. However, this can lead to problems when the flow is composed by largely different scales with similar energy content. In this case, POD is not capable of distinguishing between the different scales and it gives as a result spectral mixing.

As a solution, mPOD is an hybrid technique that combines the energy optimality of POD and the spectral purity. The principle of mPOD consists on splitting the data into scales via filtering banks. In each scale, POD is applied giving as a final result a series of modes optimal in terms of energy without frequency overlapping between them. The definition of the scales is made by the user who stablishes the frequency bandwidth of each one. The limiting case is when each scale is constrained to a single frequency because this is the basis of the Dynamic Mode Decomposition (DMD). In this project, a theoretical introduction to the POD and mPOD is given as well as the formulation of its matrix form. This is essential since the mPOD has been developed in MATLAB *and this software is a computing environment based on matrixes.*

The technique is tested with different numerical cases and a comparision between the results obtained with the POD is done. This allows to know the main advantages of the technique and also the limitations of POD. The final purpose of the project is apply the mPOD over experimental data of an axial turbine. The data was acquired in tests conducted in the facilities of the German Aerospace Center (DLR).

Considering that these techniques are widely used in different fields, a brief example of its use with PIV measures has been included. This experimental case corresponds to the velocity field of an impinging jet onto a flat surface.

Resumen

Hoy en día, la evolución tecnológica ha hecho posible el incremento de potencia computacional permitiendo la mejora de los programas de simulación . Esto permite calcular con mayor resolución espacial y temporal así como almacenar mayor cantidad de datos. Esto junto a la revolución del Big-Data, también presente en el campo experimental, ha creado la necesidad de técnicas de post-proceso. Estas son esenciales a la hora de tratar tales cantidades de datos.

Los métodos de descomposición basados en datos, se han convertido en una de las técnicas más comunes. Estos pueden ser usados tanto en casos numéricos como experimentales en el ámbito de la mecánica de fluidos, siendo el principal objetivo la identificación de estructuras, patrones y la construcción de modelos de orden reducido (ROM). La identificación de patrones es interesante desde el punto de vista de la turbulencia. Un flujo de estas características está compuesto por torbellinos y estructuras características de ciertas regiones del campo fluido, como por ejemplo las paredes. Por otro lado, la posibilidad de generar modelos con un número reducido de grados de libertad hace más fácil el análisis de los resultados, independientemente de si los datos son obtenidos en experimentos o simulaciones CFD. Con un número finito y reducido de modos, el comportamiento del campo fluido puede ser modelado.

La descomposición se hace mediante la proyección de los datos sobre una serie de bases temporales y espaciales llamadas modos, los cuales se obtienen siguiendo diferentes criterios. La llamada Multi-scale Proper Orthogonal Decomposition (mPOD) es una nueva técnica de descomposición basada en datos. Ésta deriva de la denominada Proper Orthogonal Decomposition (POD), la cual está basada en criterios energéticos. En POD, los modos obtenidos en la descomposición son óptimos en términos de energía. Sin embargo, esto puede conducir a ciertos problemas cuando el campo fluido está compuesto por escalas de diferente tamaño energéticamente similares. En estos casos, POD no es capaz de distinguir entre las diferentes escalas dando lugar a la denominada mezcla espectral.

Como solución, mPOD es una técnica híbrida que combina la optimización energética del POD y la pureza espectral. La base de esta técnica consiste en separar los datos en diferentes escalas mediante bancos de filtrado. En cada una de esas escalas, se aplica POD dando como resultado una serie de modos óptimos en términos de energía sin solapamiento en el espectro de frecuencias. La definición de las escalas se hace por el usuario, que establece el ancho de banda asignado a cada una. El caso limitante sería aquel en el que cada escala está limitada a una única frecuencia, ya que esta es la base de la técnica Dynamic Mode Decomposition (DMD). En este proyecto, se ha hecho una introducción teórica a las técnicas POD y mPOD, así como su formulación matricial. Esto es muy útil ya que la técnica se ha programado en MATLAB *que es un software basado en matrices.*

La técnica ha sido probada con diferentes casos numéricos, además se ha hecho una comparación con los resultados obtenidos con POD. Esto permite demostrar las principales ventajas de mPOD y las limitaciones de POD. El objetivo final del proyecto es aplicar la técnica mPOD sobre datos experimentales de una turbina axial. Estos datos fueron obtenidos mediante diferentes tests llevados a cabo en las instalaciones del Centro Aeroespacial Alemán(DLR).

Teniendo en cuenta que estas dos técnicas son ampliamente usadas en otros sectores, un breve ejemplo de su uso sobre medidas PIV ha sido incluido. En dicho experimento se obtuvieron medidas de velocidad de un chorro impactando sobre una superficie plana.

Resum

Actualment, l'evolució tecnològica ha fet possible l'increment de potència computacional permetent la millora dels programes de simulació. Això permet calcular amb més resolució espacial i temporal, aixi com emmagatzemar més quantitat de dades. Això al costat de la revolució del Big-Data, també present en el camp experimental, ha creat la necessitat de tècniques de post-procés. Aquestes són essencials a l'hora de tractar aquestes quantitats de dades.

Els mètodes de descomposició basats en dades, s'han convertit en un de les tècniques més comuns. Aquests poden ser utilitzats tant en casos numèrics com experimentals en l'àmbit de la mecànica de fluids, sent el principal objectiu la identificació d'estructures, patrons i la construcció de models d'ordre reduït (ROM). La identificació de patrons és interessant des del punt de vista de la turbulència. Un flux d'aquestes caracterıstiques està compost per remolins i estructures característiques de certes regions del camp fluid, com ara les parets. D'altra banda, la possibilitat de generar models amb un nombre reduït de graus de llibertat fa més fàcil l'anàlisi dels resultats, independentment de si les dades són obtingudes en experiments o simulacions CFD.

La descomposició es fa mitjançant la projecció de les dades sobre una sèrie de bases temporals i espacials denominades modes, que s'obtenen seguint diferents criteris. L'anomenada Multiscale Proper Orthogonal Decomposition (mPOD) és una tècnica de descomposició basada en dades. Aquesta deriva de l'anomenada Proper Orthogonal Decomposition (POD), la qual està basada en criteris energètics. En POD, els modes obtinguts en la descomposició són òptims en termes d'energia. No obstant, això pot conduir a certs problemes quan el camp fluid està compost per escales de diferent grandària energèticament similars. En aquests casos, POD no és capaç de distingir entre les diferents escales donant lloc a l'anomenada barreja espectral.

Com solució, mPOD és una tècnica híbrida que combina l'optimizacion energética del POD i la puresa espectral. La base d'aquesta tècnica consisteix a separar les dades en diferents escales mitjançant bancs de filtrat. En cadascuna d'aquestes escales, s'aplica POD donant com a resultat una sèrie de modes òptims en termes d'energia sense solapament en l'espectre de freqüències. La definició de les escales es fa per l'usuari, qui estableix l'ample de banda assignat a cada una. El cas limitant seria aquell en el qual cada escala està limitada a una única freqüència, ja que aquesta és la base de la tècnica Dynamic Mode Decomposition (DMD). En aquest projecte, s'ha fet una introducció teòrica a les tècniques POD i mPOD, aixı com la seua formulació matricial. Això és molt útil ja que la tècnica s'ha programat en MATLAB *que és un programari basat en matrius.*

La tècnica ha estat provada amb diferents casos numèrics, a més s'ha fet una comparació amb els resultats obtinguts amb POD. Això permet demostrar els principals avantatges de mPOD i les limitacions de POD. L'objectiu final del projecte és aplicar la tècnica mPOD sobre dades experimentals d'una turbina axial. Aquestes dades van ser obtingudes mitjançant diferents tests duts a terme a les instal·lacions del Centre Alemany Aeroespacial (DLR) .

Tenint en compte que aquestes dues tècniques són àmpliament utilitzades en altres sectors, un breu exemple del seu ús sobre mesures PIV ha estat inclòs. En aquest experiment es van obtenir mesures de velocitat d'un doll impactant sobre una superfície plana.

Acknowledgements

I would like to use these lines to express my thankfulness to all the people that has made possible this project. First of all, thanks to my supervisor Fabrizio Fontaneto for giving me the chance to work with him in the Von Karman Institute for Fluid Dynamics for six months and for giving me all the support and advice needed during the project. I must thank to Miguel Alfonso Méndez for introducing me in the modal decomposition world and helping me selflessly to develop the code. Thanks to all my coleagues in the VKI with whom I have expended most of the time, I will never forget our coffee breaks. I want to make an special mention of all my spanish friends with whom I have travelled, enjoyed my spare time and explored every corner of the city. Thanks to them and our adventures, now I love Brussels. I cannot forget my family, they always have been the most important pillar in my life and in this experience they have supported me without hesitation. Thanks to them now I am who I am.

Contents

List of Figures

List of Tables

List of Symbols

Acronyms

BPF Blade Passage Frequency

CFD : Computational Fluid Dynamics

DFT Discrete Fourier Transform

DLR German Aerospace Center

DMD Dynamic Mode Decomposition

DWT Discrete Wavelet Transform

FACTOR Full Aero-thermal Combustor Turbine interactiOns Research

FFT Fast Fourier Transform

mPOD Multi-scale Proper Orthogonal Decomposition

MRA Multi-Resolution Analysis

PIV Particle Image Velocimetry

POD Proper Orthogonal Decomposition

ROM Reduced Order Models

SPOD Spectral Proper Orthogonal Decomposition

SVD Singular Value Decomposition

VKI Von Karman Institute for Fluid Dynamics

Symbols

ΔT Time step

κ Spatial frequency

$\mathcal{A}$ Matrix of areas

$\mathcal{H}_r$ 2D transfer function of r scale

ω Temporal frequency

Φ	Matrix of spatial structures
ϕ_r	Spatial structure of r mode
Ψ	Matrix of temporal structures
ψ_r	Temporal structure of r mode
Σ	Matrix of energy content
σ_r	Energy content of r mode
D	Data matrix
F_s	Sampling frequency
F_v	Frequency splitting vector
K	Correlation matrix
N_m	Number of modes
N_t	Number of temporal samples
N_θ	Number of discretizations in pitch direction
N_{rad}	Number of discretizations in radial direction
St	Strouhal number
V_θ	Tangential component of velocity
V_r	Radial component of velocity

Subscripts

$(\,)_{\mathcal{M}}$	Referring to mPOD
$(\,)_{\mathcal{P}}$	Referring to POD

Part I

Report

Chapter 1

Introduction

1.1 Motivation

Turbomachines play an important role not only in aircraft propulsion but also in other sectors such as the energy, automotive and naval industries. In the last years, the number of aircrafts have increased and the requirements to accomplish in terms of pollution and performance have become really demanding for the engine aircraft motivating the evolution of them. This evolution gives rise to the necessity of developing new and more efficient techniques. These methods not only make more accurate the numerical simulations but also facilitate the experimental testing and the acquired data post-processing.

Turbomachines are an essential part of the core engine and consequently its improvement requires its evolution. In the last decades, new techniques and methods have arisen for the purpose of increasing the efficiency and reducing the flow leakage in compressors and turbines. Some of these techniques are the clearance control done by managing the refrigeration system, or the use of variable bleed valves and variable stator vanes.

The operating clearances in turbomachines are an important source of leakage flow. Sealing management is fundamental to reduce that flow leakage from pressure side to suction side in compressors. New technologies such as shrouded stators are being used in compressors in contrast with the cantilevered stators. In this case, the integration is really complex but the benefit is that the flow recirculation is limited and therefore the pressure ratio can be raised. In addition to the difficulties in the design phase and the mechanical construction, the unsteady aerodynamic behaviour of the flow field in the proximities of the seal has to be considered since it can affected the turbomachine performance.

A detailed comprehension of the unsteady aerodynamic phenomena is crucial for determining the less-driving mechanisms. On the base of this information, different strategies can be derived to improve the aerodynamic design of turbomachinery components and further exploit the available efficiency join. On the other hand, a precise knowledge of the flow dynamic behaviour is a key parameter for the structural design of components with a possible weight reduction as an outlook.

Computational Fluid Dynamics (CFD) techniques are really useful tools to study the aerodynamic of blades passages in turbomachinery. In combination with the high capacity of the computers, a higher quantity of data can be obtained in numerical simulations as well as in real experiments. In these cases, the post-processing techniques are required to treat and analyse that amount of data. Besides, data-driven techniques can be used to identify patterns in both large numerical studies and experimental cases. One of the most useful application of these techniques consists on obtain Reduced Order Models (ROM) that are capable to model the flow field in a simpler way using a reduced number of modes. This process makes easier the interpretation of the results and the analysis of phenomena. Phasing of flow phenomena, energy level and spatial resolution are all relevant information at such extent.

This project has been conducted in the Turbomachinery Department of the Von Karman Institute for Fluid Dynamics (VKI). The main aim consisted on developing the Multi-scale Proper Orthogonal Decomposition (mPOD) in MATLAB to process experimental data of axial turbomachines. The code has been designed to post-processing the pressure field but it can be easily adapted to treat the velocity field or the temperature field, and also to treat experimental data from other kind of turbomachines. The data used in this work was acquired in the facilities of the German Aerospace Center (DLR) for previous projects. This technique combines the Multi-Resolution Analysis (MRA) via the Discrete Wavelet Transform (DWT) with the Proper Orthogonal Decomposition (POD) giving as a result an hybrid technique. The POD is the preceding technique of the mPOD and its foundation is the same for both techniques. The main difference is that in the mPOD the correlation matrix that describes the flow field is decomposed into different scales each retaining a non-overlapping portion of the spectra of the original correlation matrix, then the POD is applied to each scale. In this way, the modes obtained to represent the flow field are optimal in terms of representative energy, but also multi-scale phenomena having similar energy content is distinguished.

1.2 Previous projects

This project is focused on the development of the mPOD technique and its application to analyse the flow field of an axial transonic turbomachine. This technique derives from the POD so it is necessary to consider a thorough research in this.

Previous projects focused on POD method have been reviewed. Grau [7] gives the mathematical basis behind this method and validates it with three synthetic cases. Some other projects like Kenneth et al. [5] employed POD to compute the unsteady aerodynamic and aeroelastic behaviour of an isolated transonic airfoil and a two-dimensional cascade of airfoils. Cizmas et al. [1] also used this technique to study the rotor-stator interaction in a turbine through numerical simulations, very similar study did Rochuon [18] to extract the dominant modes in this type of interaction.

According to the mPOD method, Mendez projects [15] and [16] are really relevant. The first one is more focused on the mathematical basis of the technique and its connection with the Discrete Fourier Transform (DFT) and Dynamic Mode Decomposition (DMD) and a comparision between the three methods is done through three particular cases. The second project is mainly focused on the flow field of an impinging jet obtained by time-resolved optical measurements and the comparision between the POD and the mPOD applied over the velocity field.

Countless researchs related to the aerodynamic and turbulent phenomena into axial compressors and their influence in the performance of the compressor have been done, also in turbines.

Marty [11], Wellborn [20] and Farkas [3] among others have studied this topic numerically with CFD techniques.

Focused on the flow interface between the combustor and the high-pressure turbine the FP7 project FACTOR should be mentioned. Both experimental [8] and numerical results [4] are really interesting and data acquired in those experiments is used in this project.

1.3 Objectives

Taking into account that the mPOD technique is a novel post-processing method, it is essential to approach its study from the base. The mPOD derives from the POD, so the best way to approach the study is to begin with it. This is the key to define the objectives of the project.

- Understand the POD principles and its mathematical basis. Familiarize with its application and its MATLAB codification.
- Understand the mPOD principles and its mathematical basis. Understand the differences with POD and the limitations of the last one. Familiarize with its application and limitations in comparison with the predecessor.
- Develop a MATLAB code with the implementation of the mPOD and test it in differenct cases.
- Apply the created code to experimental data acquired in real conditions of an state-of-art axial turbine.
- Understand the physical meaning of some phenomena that takes place into the turbomachine.

These objectives allow to determine the different steps to take during the development the project. These steps or phases are described in the next section.

1.4 Methodology

Given that the objectives have been clearly defined, defining a methodology is essential to determine the path to follow during the project.

First of all, a literature survey is needed in order to fmiliarize with the application of POD and mPOD as well as to review the methodology followed in some of the previous projects mentioned in §1.2. Besides, this literature survey eases to familiarize with the modal analysis and multiresolution analysis applying the wavelet transform to flow fields with the purpose of obtain reduced order models. Therefore it is needed to review the theory behing the wavelet transform and its application to image processing due to the similarity between this and the processing of experimental data.

Since the main objective of the project is apply the mPOD to experimental data of state-of-art transonic axial turbomachines, the literature survey should cover the knowledge of the facilities where the experiments were conducted as well as the comprehension of some unsteady phenomena that occur during the operation.

Once the literature survey is finished, a systematic methodology, whose steps are described below, is defined. It is worth mentioning that the software employed in the project is MATLAB, so all the allusions to programming or running codes are refered to this software.

1. Programme the POD and apply it to a typical synthetic case. This case is being modified in order to identify the limitations of the method.

2. Programme a filtering routine in both one-dimensional and two-dimensional synthetic cases.

3. Programme the mPOD and apply it to the same synthetic cases to compare the results and limitations between both techniques.

4. Apply the mPOD to exprimental data.

5. Analyze the results to understand the physics behind the aerodynamics and unsteady phenomena in turbomachines.

Chapter 2

Theoretical Basis

Nowadays, the higher capacity of computers makes that in computational simulations the number of variables and data is sharply increasing, as well as in experiments. With the current big-data revolution, post-processing techniques are necessary to treat and analyze the variables and they can be used in a large number of different industries.

An useful application of these techniques consists on obtaining models of the flow field with a reduced number of degrees of freedom, what is called Reduced Order Modelling. In some cases, the number of degrees of freedom in flow solvers can be reduced from a thousand of them to a few ten and this gives as a result a reduced computational cost and an improvement of the convergence. The models obtained not only are able to represent the flow field but also are used to recognize patterns in turbulent flows that in advance resemble chaotic, this patterns are known as coherent structures and are defined as *the deterministic function which is best correlated on average with the realizations* [10].

A data-driven decomposition applied on a flow field is able to model its behaviour by means of a series of basis elements called modes. Each of these modes is characterized by a temporal and a spatial structure with a fixed energy contribution. Several post-processing techniques are currently being developed like Dynamic Mode Decomposition (DMD), Proper Orthogonal Decomposition (POD), Discrete Fourier Transform (DFT) or Multi-scale Proper Orthogonal Decomposition (mPOD).

In this chapter, the fundaments of the POD and the mPOD are going to be explained in detail as well as their relation with the DFT. First of all, as the POD is the preceding technique of mPOD this one is the first in being developed and analysed. Besides, the limitations of both techniques are going to be explained and demonstrated in the following chapters with results from different synthetic and experimental cases.

Since the application of the mPOD requires the definition of a filter bank a slight introduction of filtering process has been done in this chapter. Besides, some fundaments of the bank filter construction are reviewed to provide the basis required to the implementation in the mPOD code thorough some simple synthetic cases.

The finality of the project is apply the mPOD to experimental data obtained from axial turbomachines, and therefore a deep literature survey should be done. As part of this survey, a review of the most important flow features in a shrouded compressor is done at the end of this chapter. Through a slight literature review, the behaviour of the flow in the different areas around the stator stage is reviewed and explained. Also, brief comments about the influence over the compressor performance are given.

2.1 Proper Orthogonal Decomposition (POD)

As it has been mentioned, POD is a very useful post-processing technique to treat and analyze large quantities of data to extract synthetic information. This data can be computationally or experimentally obtained. It can be presented in two different ways, the continuous form applicable to time-functions and the discrete form to process realizations of variables. Commonly, POD is applied to treat turbulent flows trying to identify coherent structures among the apparent chaos. However, this technique is known by several names like Karhunen-Loeve decomposition since it has been widely applied in different disciplines like image processing or signal analysis.

The POD establishes an optimal set of orthogonal basis composed by functions estimated from a typical eigenvalue problem. That set of basis constituted a series of modes that are energically optimal considering that a finite number of those modes are able to capture a significant quantity of energy of an infinite-dimensional process. Besides, the POD basis is unique since no other decomposition of the same order is able to capture an equivalent quantity of energy. This is the consequence of the choice of the spatial functions $\phi^{(k)}(x)$ in the descomposition of a vector-valued function $u(x,t)$ showed below. POD is based on the fundament that the spatial terms of the finite sum are intrinsically determined from the function to approximate. Given that the sequence of the temporal functions depends on the spatial functions chosen unless they were orthonormal, orthonormality is a mandatory requirement in POD to have an unique decomposition.

$$u(x,t) = \sum_{k=1}^{K} a^{(k)}(t)\phi^{(k)}(x) \tag{2.1}$$

Hereafter, all the explanations and mathematical developments are associated with the *Snapshot POD* that is the discrete form that has been commented. Thanks to the connection between the POD and the Singular Value Decomposition (SVD), the POD modes can be calculated as a simple matrix factorization.

Let's assume that the time realizations or snapshots are arranged in a matrix $D(x_i, t_k) = D[i,k]$ in which each column correspond with a temporal discretization of the whole spatial grid.

$$D(x_i,t_k) = D[i,k] = \begin{bmatrix} d_1[1] & ... & d_k[1] & ... & d_{n_t}[1] \\ . & . & . & . & . \\ . & . & . & . & . \\ d_1[n_s] & ... & d_k[n_s] & ... & d_{n_t}[n_s] \end{bmatrix} \tag{2.2}$$

The way the spatial points are arranged in a two-dimensional vector is irrelevant as long as it was organized, because the results are extracted applying the same procedure. Let imagine

that the samples are obtained from a two-dimensional grid where $x \in [x_i, x_f]$ and $y \in [y_i, y_f]$. All this data has to be arranged in a two-dimensional matrix so all the spatial points have to be organized in a row.

The main point of a discrete decomposition is to represent the data matrix as a finite sum of a series of contributions in a similar way than in the equation 2.1.

$$D[i,k] = \sum_{r=1}^{rk(D)} \sigma_r \phi_r[i] \psi_r[k] \tag{2.3}$$

The construction of a Reduced Order Model (ROM) lies in the truncation of the finite sum of the expression above at $rc < rank(D)$. Furthermore, the discrete decomposition can be expressed as a matrix factorization of the form 2.4. The matrices Φ and Ψ contain the spatial and the temporal structures of the modes while Σ is a diagonal matrix in which each element is the energy content of each mode. The fact that the matrix Σ was diagonal implies that defining either Φ or Ψ the other one is fixed and unique.

$$D[i,k] = \sum_{r=1}^{rk(D)} \sigma_r \phi_r \psi_r^T = \Phi \Sigma \Psi^T \tag{2.4}$$

The next step is clearly defined and it consists on obtaining the matrix of one of the structures, either the temporal or the spatial. Although there are different manners to proceed, the POD that is developed and used in this project firstly computes the temporal structures Ψ through the eigenvectors of the correlation matrix.

The correlation matrix can be obtained applying the expression 2.5 in which the symbol $(\bullet)^\dagger$ represents the *Hermitian transpose*. This operation is transposition whether the correlation matrix is real. The second part of the 2.5 is certain as long as the data matrix is real.

$$K = D^\dagger D \rightarrow K = \Psi \Lambda \Psi^T = \sum_{r=1}^{rk(D)} \lambda_r \psi_r \psi_r^T \tag{2.5}$$

The energy content of the whole dataset can be calculated through the Frobenius norm whose expression is shown in 2.6 where the different λ_r values are the eigenvalues of the correlation matrix.

$$\|D\|^2 = Tr(D^\dagger D) = Tr(K) = \sum_{r=1}^{rk(D)} \lambda_r \tag{2.6}$$

By merging the expressions 2.4 and the definition of the correlation matrix as done in the first part of 2.5, it can be demonstrated the orthonormality of the temporal and spatial structures. From 2.7 it is clear that $\Lambda = \Sigma \Phi^T \Phi \Sigma$ and since Σ is a diagonal matrix it can be deduced that $\Phi^T \Phi = I$, and therefore $\Lambda = \Sigma^2$. The previous steps implies that the spatial structures are also real and orthonormal.

$$K = D^{\dagger}D = (\Phi\Sigma\Psi^T)^{\dagger}(\Phi\Sigma\Psi^T) = \Psi\Sigma\Phi^T\Phi\Sigma\Psi^T \tag{2.7}$$

Once the Singular Value Decomposition of the correlation matrix is done and the temporal structures are obtained, the next step is the projection of the data in this temporal structures via the right multiplication as it is shown in 2.8. Since the spatial structures are orthonormal $\|\phi_r\| = 1$, the norm of this projection is a direct way to obtain the energy content of each mode.

$$\begin{aligned} D\Psi &= \Phi\Sigma\Psi^T\Psi = \Phi\Sigma \\ \|D\Psi\| &= \|\Phi\Sigma\| = \|\Sigma\| \rightarrow \sigma_r = \|D\Psi\| \end{aligned} \tag{2.8}$$

Only when the matrix Σ is known, the calculation of the spatial structures is possible as in 2.9. In order to save computational cost, avoiding the matrix inversion is necessary, leading to an element-by-element operation.

$$\Phi = D\Psi\Sigma^{-1} \tag{2.9}$$

Now that both the temporal and the spatial structures are known as well as the energy content of each mode, the next step is to choose the number of modes to retain for the construction of the reduced order model. There are many ways to proceed but the most common options are related to energy criteria. Some of these criteria consists on only retain those M modes that contain more than certain value of the total energy commonly about the 90 %, and some others are linked with the evolution of the slope of the energy plot.

A significant idea to take into account is that the vectors of the spatial Φ and temporal Ψ structures are organized in the same way than the data matrix. The different structures are reshaped back following the same procedure as in the data matrix.

After having detailed the general POD process, it is necessary to remark that in this project the technique is going to be applied to a non-cartesian grid. The POD technique explained above makes use of the Euclidian definition of the inner product to define the correlation matrix. Since the spatial grid is cylindrical due to the path followed to measure the data, it originates a mesh where are largely different areas whereas in a cartesian grid this problem does not exist. It is therefore necessary to average the Euclidean inner product to weight the contribution of each point of the mesh to the total energy. The complete averaging process is detailed with a sample case in §2.1.1.

Although the results of applying the POD to a synthetic case as well as to a experimental case will be showed and extensively discussed in following chapters, some limitations of this technique can be already commented. The POD is an energy-based decomposition, and this means that the decomposition is optimal in a least-square sense as well as in terms of the representation of the energy present within the data. However, there are some situations where it becomes really difficult the detection of coherent structures applying this criteria like the treatment of unsteady phenomena in flows . For example, let's imagine that different phenomena ocurring at different frequencies have similar energy content so an energy-based method cannot distinguish these contributions and this leads to the phenomena called spectral mixing.

The so called spectral mixing is a really significant problem if the purpose of the POD is detecting patterns in unsteady flows. This occurs when phenomena are spanned along the whole frequency and energy spectra, and due to all the POD modes share the full set of frequencies the distinction of these is not possible. Actually, the spectral mixing is quite difficult to avoid since in most of the signals obtained in experiments the noise is present and it usually has a large frequency content. Other possible situation is that the most energetic modes do not always have relevant meaning so it is difficult to identify physical phenomena. Because of these limitations it is necessary to find a proper technique to reduce them.

2.1.1 POD averaged

As explained before, not only in the experimental case but also in the synthetic case the spatial grid is non-cartesian. It is therefore necessary to weight all the inner products of the POD process. To exemplify the averaging process, a simple synthetic case is explained below. Concerning the experimental case, the averaging process is identical but the spatial grid is an annulus sector, so the main difference lies on the way the areas are computed.

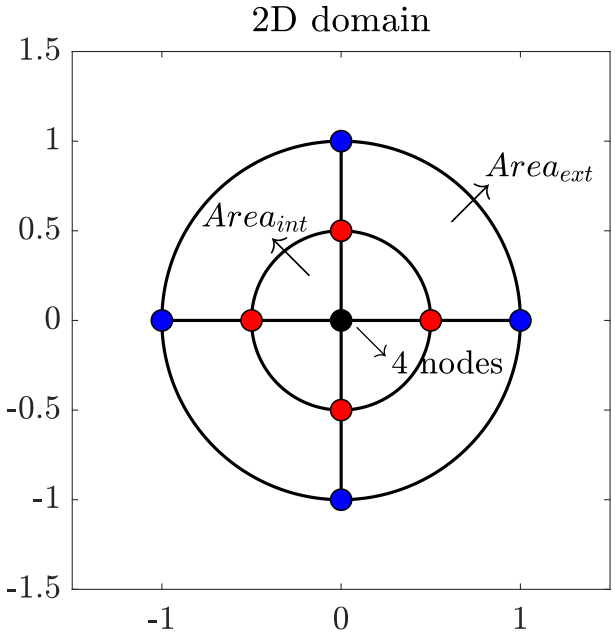

Figure 2.1: Spatial grid of the synthetic case

Let C be the circular domain shown in the Figure 2.1, that actually is a simplification of the real domain which is composed by more spatial points. The averaging process consists on assigning an area to each node to balance its contribution to the total energy. Each node represents a measure point in the experimental case, and in the synthetic one it represents a spatial point where the flow field is computed.

The area assigned to each node is obtained averaging the areas in which each node is contained. The areas of the sample domain A_{ext} and A_{int} are computed dividing the area of the annulus obtained with the radial discretization into the number of sectors formed from the circumferencial discretization.

The four red nodes contained in the middle of the circumference are averaged with the four areas $Area_{int}$ and the four areas $Area_{ext}$ because each node belongs to two different $Area_{int}$ and $Area_{ext}$. Therefore, the area assigned to each red node is the mean value showed in 2.10.

$$A_{Red\,Nodes} = \frac{2A_{ext} + 2Aint}{4} = \frac{1}{2}(A_{int} + A_{ext}) \tag{2.10}$$

In the case of the internal and external nodes, the black nodes and the red ones respectively are only contained in two $Area_{int}$ or two $Area_{ext}$. In this case, the area assigned to these nodes are obtained from 2.11.

$$\begin{aligned} A_{Black\,Nodes} &= \frac{2A_{int}}{2} = A_{int} \\ A_{Blue\,Nodes} &= \frac{2A_{ext}}{2} = A_{ext} \end{aligned} \tag{2.11}$$

This averaging process is done in each inner product of the POD process by a matrix multiplication. The matrix of areas $\mathcal{A}$ has to be arranged in the same way as the samples have been organized in the data matrix $D[i,k]$. Each column of the data matrix corresponds to the measures in a certain node but at different times, since this nodes don't change the columns of the matrix of areas are the same.

In the experimental case, the domain is an annulus sector. Although the averaging process affects the inner products and therefore the same steps, the way the areas are computed slightly differs from the one explained above.

The steps listed below are those in which the averaging is done. The symbol ($\odot$) represents the *Hadamard product* that corresponds to a element-by-element matrix multiplication.

- In the calculation of the temporal correlation matrix.

$$K = (D \odot \mathcal{A})^T \cdot D \tag{2.12}$$

- In the projection of the data matrix into the temporal structures.

$$\Phi\Sigma = (D \odot \mathcal{A})^T \cdot \Psi \tag{2.13}$$

- In the calculation of the energy content of each mode and its spatial basis.

$$\Sigma = \left\| \frac{\Phi\Sigma}{\mathcal{A}} \right\| \rightarrow division\,element\,by\,element \tag{2.14}$$

$$\Phi = \frac{\Phi\Sigma}{\mathcal{A} \cdot \Sigma_p} \rightarrow division\,element\,by\,element \tag{2.15}$$

2.2 Multi-scale Proper Orthogonal Decomposition

According to the limitations of the POD commented in the previous section §2.1 it is necessary to develop a new technique able to overcome those problems. In addition to the energy-based data-driven decomposition, there is another approach that is the frequency-based criteria.

The frequency-based methods are based on the Discrete Fourier Transform (DFT) and they assign a single frequency to each mode of the decomposition. A series of pure harmonic modes are unable to represent phenomena like frequency modulation or frequency and phase jitter. The most well-known frequency-based method is the Dynamic Mode Decomposition (DMD) that suits for data-driven stability analysis, but this is not the object of this project.

It is therefore evident that the spectral purity is not a proper approach in the data-driven decomposition, as well as the energy maximization employed by the POD. One possible approach developed by Sieber is the Spectral Proper Orthogonal Decomposition (SPOD) and it consists on pre-filtering the data before computing the traditional POD. However, this method can modify the correlation matrix specially in unsteady processes causing the non-orthogonality of the different basis.

The Multi-scale Proper Orthogonal Decomposition (mPOD) is the technique that combines both approaches. Instead of pre-filtering the correlation matrix, mPOD applies the Multi-resolution Analysis (MRA) to split the correlation matrix into different scales and then the typical eigenvalue problem of the classical POD is computed in each scale. The splitting process can be done via the 2D Wavelet Transform or in a more general way applying a filter bank, in both cases each scale contains a non-overlapping portion of the spectra of the correlation matrix.

In this section, the mathematical basis of the mPOD technique as well as its steps are explained and developed in detail according to the path followed by Méndez [15]. In the following chapters, the results of applying it to the different synthetic cases and the experimental data are detailed accompained by the comparison of the results between the POD and the mPOD.

The Multi-resolution Analysis is applied in the frequency domain. This means that the Fourier Transform of the correlation matrix is needed. This transformation can be done by a matrix multiplication with the Fourier Matrix $\Psi_{\mathcal{F}}$ defined in 2.16, where $w = exp(2\pi i/N_t)$. Hereafter, $\Psi_{\mathcal{F}}$ is refered to the Fourier Matrix whereas $\Psi_{\mathcal{P}}$ makes reference to the temporal basis of the POD.

$$\Psi_{\mathcal{F}} = \frac{1}{\sqrt{N_t}} \begin{bmatrix} 1 & 1 & 1 & \cdots & 1 \\ 1 & w & w^2 & \cdots & w^{N_t-1} \\ \vdots & \vdots & \ddots & \vdots & \vdots \\ 1 & w^{N_t-1} & w^{2(N_t-1)} & \cdots & w^{(N_t-1)^2} \end{bmatrix} \tag{2.16}$$

$$\hat{K} = \overline{\psi_{\mathcal{F}}} K \overline{\psi_{\mathcal{F}}} \tag{2.17}$$

The Discrete Fourier Transform of the correlation matrix 2.17 is necessary to define the frequencies of the filter bank. The filter bank requires the previous definition of the frequency splitting vector $F_v = [f_1^c, f_2^c, ...f_{M-1}^c]$. The values of these frequencies is chosen according to the analysis of the frequency content of the correlation matrix.

The filter bank is made up of low-pass filter with f_1^c as cut-off frequency, a high-pass filter with f_{M-1}^c as cut-off frequency and $M-2$ band-pass filters. The maximum value that f_{M-1}^c can take is limited ($f_{M-1}^c = f_s/2$) by the Nyquist theorem. There are many ways to obtain the filters, such as calculating them from a series of low-pass filters or using the functions implemented in the Signal Processing Toolbox of MATLAB. The process of retaining a part of each scale is shown in the Figure 2.2.

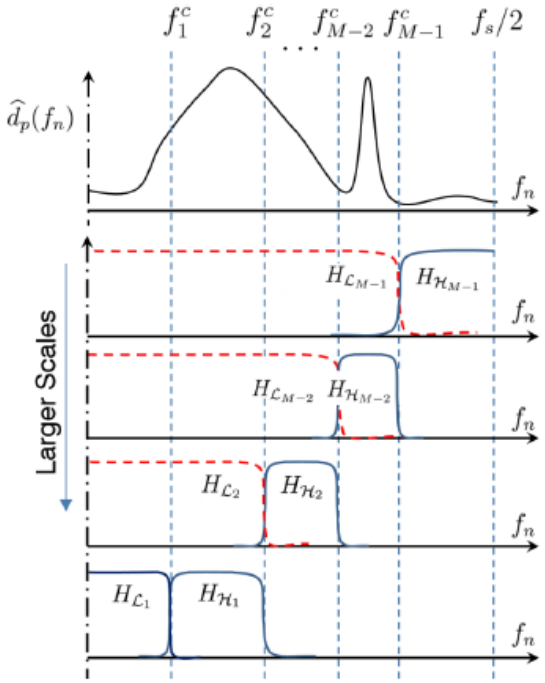

Figure 2.2: Multi-Resolution Analysis of a signal in the frequency domain [15]

Each filter has associated a transfer function $\mathcal{H}_m$. Since the filtering process is done in the frequency domain, it is applied via the Hadamard product between matrices. Since the filters are defined via 1D transfer functions, to apply the filtering process is necessary to replicate this functions to 2D matrices having all the row equal to the 1D transfer function. Let's denote H'_m the 2D transfer function of one of the filters, the filtering of the data matrix is can be computed as in 2.18.

$$\hat{D}_m = \hat{D} \odot H'_m = (D\Psi_{\mathcal{F}}) \odot H'_m \rightarrow D_m = \left[(D\Psi_{\mathcal{F}}) \odot H'_m\right] \Psi_{\mathcal{F}} \tag{2.18}$$

Introducing 2.18 in the definition of the correlation matrix, it can be computed the correlation matrix of the scale m.

$$K_m = D_m^{\dagger} D_m = \bar{\Psi}_{\mathcal{F}} \left[(\hat{D} \odot H'_m)^{\dagger} (\hat{D} \odot H'_m)\right] \Psi_{\mathcal{F}} = \bar{\Psi}_{\mathcal{F}} \left[(\hat{D}^{\dagger}\hat{D}) \odot ((H'_m)^{\dagger} \odot H'_m)\right] \Psi_{\mathcal{F}} \tag{2.19}$$

$$K_m = \bar{\Psi}_{\mathcal{F}} \left[K_{\mathcal{F}} \odot \mathcal{H}_m\right] \Psi_{\mathcal{F}} \tag{2.20}$$

In the expression 2.20 the matrix $K_{\mathcal{F}} = \hat{D}^{\dagger}\hat{D}$ makes reference to the cross-spectral density matrix whereas $\mathcal{H}_m = (H'_m)^{\dagger} H'_m$ is the 2D transfer function of the filter. The cross-spectral

density matrix $K_{\mathcal{F}}$ has the same eigenvalues of the corresponding correlation matrix in that scale K_m.

An important fact of the filtering process is that if the filter of the scale allows a certain frequency content, the POD modes at that scale are constrained to that interval of frequencies.

$$\begin{aligned} K_{\mathcal{F}} = \hat{D}^{\dagger}\hat{D} = \Psi_{\mathcal{F}}[D^{\dagger}D]\bar{\Psi}_{\mathcal{F}} = \Psi_{\mathcal{F}}K\bar{\Psi}_{\mathcal{F}} \rightarrow \\ \rightarrow \hat{K} = \bar{\Psi}_{\mathcal{F}}[\bar{\Psi}_{\mathcal{F}}K_{\mathcal{F}}\Psi_{\mathcal{F}}]\bar{\Psi}_{\mathcal{F}} = \bar{\Psi}_{\mathcal{F}}\bar{\Psi}_{\mathcal{F}}K_{\mathcal{F}} \end{aligned} \tag{2.21}$$

$$K_m = \Psi_{\mathcal{F}}[\hat{K} \odot \mathcal{H}_m]\Psi_{\mathcal{F}} \tag{2.22}$$

According to the expression 2.22, filtering the original correlation matrix with the appropiate 2D filter gives as a result the correlation matrix at certain scale K_m.

The mPOD is a technique that depending on the definition of the splitting vector frequency F_V allows to change from POD to DFT. This means that it can move from the energy optimality to the spectral purity. Defining an empty splitting vector frequency means that the mPOD is computed in only one scale in which all the discrete frequencies are allowed for the eigenvectors. In this case, it would be spectral mixing as it was commented in the previous section 2.1.

On the contrary, the limiting case in which the frequency splitting vector is chosen as $F_v \rightarrow rF_s/(\Delta t N_t)$ corresponds to the DFT technique. In this case, each scale is restricted to a unique frequency and pure harmonic modes are considered. The DFT has some limitations most of which would be adopted by the mPOD such as the poor convergence. However, the possibility of changing from POD to DFT is one of the most significant advantages of the mPOD.

Between these two limiting cases, there are many different options. With a limited number of scales, each scale has a single correlation matrix without overlapping spectra. Let imagine that two different phenomena occur at different scales, this phenomena would therefore be assigned to different modes.

$$K \approx \Psi_{\mathcal{F}}[\hat{K} \odot \mathcal{H}_{\mathcal{L}_1}]\Psi_{\mathcal{F}} + \sum_{m=1}^{M} \Psi_{\mathcal{F}}[\hat{K} \odot \mathcal{H}_{\mathcal{H}_m}]\Psi_{\mathcal{F}} \approx K_{\mathcal{L}_1} + \sum_{m=1}^{M-1} K_{\mathcal{H}_m} \tag{2.23}$$

Once the frequency splitting vector is defined, according to the analysis of the Fourier Transform of the matrix correlation, the original correlation matrix can be estimated as 2.23. Each of these scale has its own temporal and spatial basis as showed in 2.24.

$$K \approx \Psi_{\mathcal{L}_1}\Sigma^2_{\mathcal{L}_1}\Psi^T_{\mathcal{L}_1} + \sum_{m=1}^{M-1} \Psi_{\mathcal{H}_m}\Sigma^2_{\mathcal{H}_m}\Psi^T_{\mathcal{H}_m} \tag{2.24}$$

In the ideal case in which the order of the filters could be infinite, there would not be frequency overlapping between the scales so there would be N_t non zero eigenvalues as maximum. However, due to the limit in the size of the filters the non zero eigenvalues is higher than N_t. In this case, mPOD only has to retain the first N_t dominant eigenvalues. To do this, the full set of eigenvalues is sorted according to the energy content in decreasing order. The new arrangement of the eigenvalues has to be transferred to the temporal and spatial basis independtly of

the original scale. Let call $\Psi^0_{\mathcal{M}}$ the new matrix containing all the new temporal basis in an ordered way.

Since the perfect spectral separation is really complicated to achieve, the temporal matrix resultant of the re-arrangement can be non-orthonormal. The reduced QR factorization is used to compensate the problem as in the expression 2.25.

$$\Psi^0_M = \Psi_{\mathcal{M}} R \rightarrow \Psi_{\mathcal{M}} = \Psi^0_{\mathcal{M}} R \tag{2.25}$$

After the QR factorization, the last step should be done. From the temporal basis the spatial ones can be computed and sorted again in descending order according to their energy content.

As well as it happened with the POD technique, the procedure explained above is the general one. In the case of apply it to a non-cartesian grid, the averaging process is necessary. Instead of using the Euclidean inner product, the mPOD requires the averaged version. The arrangement of the areas matrix $\mathcal{A}$ has to be done in the same way as the arrangement of the data matrix, and the steps in which the inner product has to be modified are the same as in the averaged POD explained in detail in §2.1.1.

To summarize, the steps of the averaged mPOD have been listed below in order to make easier its programming in a computational software like MATLAB.

1. Assemble the data matrix $D[i,k]$ from the snapshots
2. Obtain the correlation matrix via the averaged inner product of the data matrix $K = (D^\dagger \odot \mathcal{A})D$
3. Compute the Discrete Fourier Transform of the correlation matrix via $\hat{K} = \bar{\Psi}_{\mathcal{F}} K \bar{\Psi}_{\mathcal{F}}$
4. According to the spectra analysis of $\hat{K}$, define the frequencies of the filter bank, compute the transfer functions and divide K into different scales
5. Compute the Singular Value Decomposition of each scale $K_m = \Psi_m \Sigma^2_m \Psi^T_m$
6. Sort the full set of eigenvalues and re-arrange the temporal basis into $\Psi^0_{\mathcal{M}}$
7. Polish the loss of orthogonality thorugh QR factorization (see 2.25)
8. Obtain the spatial basis via the averaged inner product $\Phi_{\mathcal{M}} = D\Psi_{\mathcal{M}}\Sigma^{-1}_{\mathcal{M}}$
9. Finally, sort the modes according to a descending energy contrution and choose the number of modes to retain

As it has been commented before, the analysis of the power of this technique as well as the comparison with the POD is done in following chapters.

2.3 Filter Bank Design

In many different disciplines, the signal processing is required. To do this task, countless tools and techniques have been developed. For instance, filtering is one of them and it is useful to suppress the noisy content of a signal or to split the signal into different signals when it presents spectral mixing.

In this project, the mPOD requires a filtering process to be able to split the correlation matrix and therefore the phenomena into different scales to afterwards apply the POD. The filter bank designed requires the definition of the frequency splitting vector (see §2.2) to compute the different filters. After computing the two-dimensional transfer functions of them, the filtering is done via matrix multiplication.

To begin with the explanation of the design process, a sample 1D case is explained below. Since the transfer functions are computed from the one-dimensional filters, the underlaying principle is common. There are many different types of filters but in the mPOD and therefore in this example, the *Finite Impulse Response* filters are used.

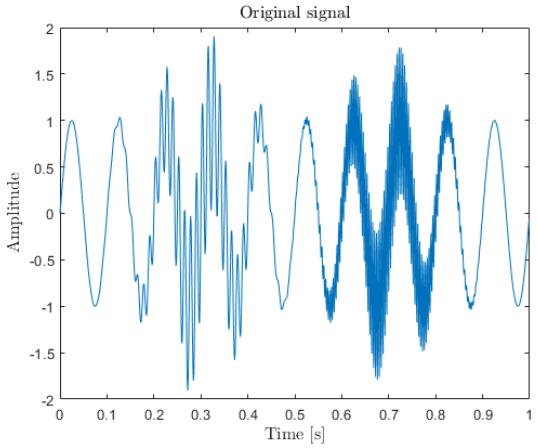

Figure 2.3: Synthetic signal

Let's start with a simple and harmonic signal composed by three different frequencies as can be see in the Figure 2.3. In this case, these frequencies are known because it is a synthetic signal composed by three modes so the splitting frequency vector can be directly defined. In a real case, like the experimental one this project deals with, it is necessary to apply a previous spectra analysis to identify the main frequencies.

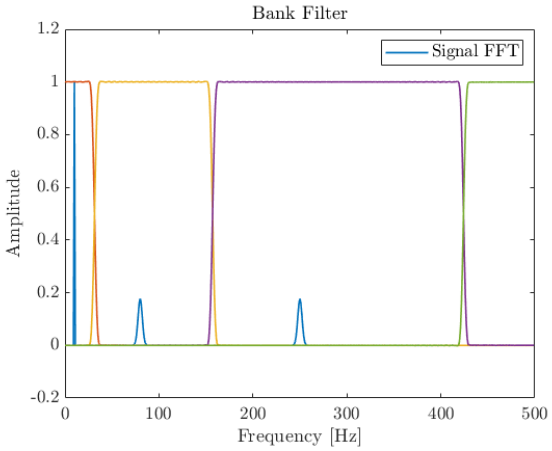

Figure 2.4: Spectra analysis and bank filter

The splitting frequency vector $F_v = [f_1^c,\ f_2^c,\ f_3^c]$ defines a low-pass filter, two band-pass filters and a high-pass one. The frequency selection is done according to have the peaks in the spectra analysis more or less centered in the filter. The Figure 2.4 shows the frequency content of the original signal as well as the windows created by each filter. As it can be observed, there is a small frequency overlapping between the filters since the windows are not perfectly square. In this synthetic case, the overlapping is not a problem due to the simplicity of the signal. As it has been mentioned before, for the implementation of the mPOD the *Signal Processing Toolbox* of MATLAB has been used.

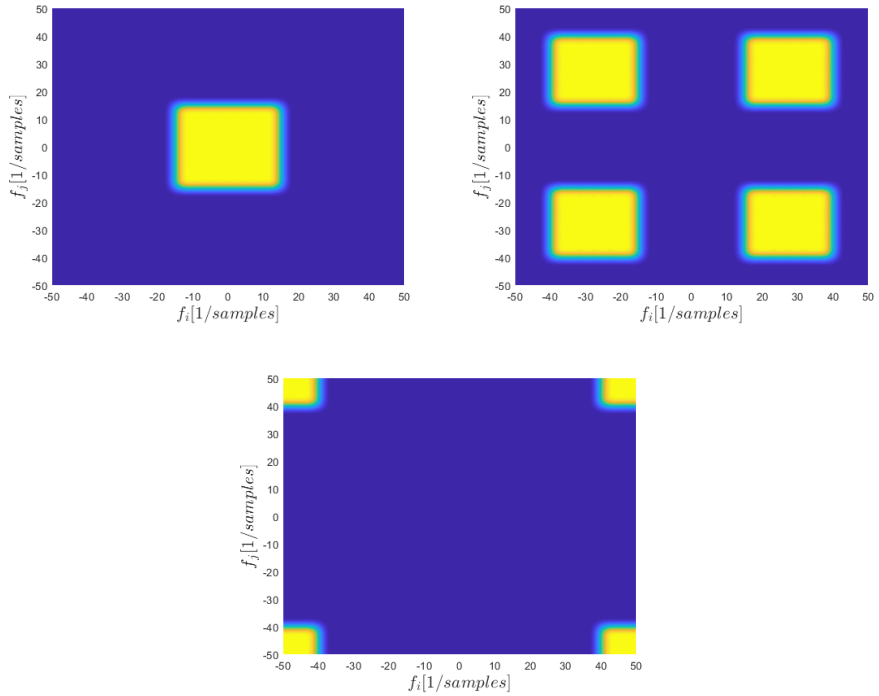

Figure 2.5: Two-dimensional filter bank

From the expression 2.19, the two-dimesional transfer functions of the filters in mPOD are computed applying the Hadamard product between the transfer function of the one-dimensional

filters. Defining a frequency splitting vector with two frequencies the resultant filters are like the ones showed in the Figure 2.5. The sharpness of the filters can produce frequency overlapping, but this problem can be reduced through choosing properly the order of the filters.

In the mPOD, an algorithm has been used to determine the proper order of each filter. The expression 2.26 shows that algorithm where $a = F_s/20$ and $b = -1/20$ which is applied to each frequency of the vector F_v. Sometimes, if the order obtained is higher than desired, it can be reduced applying a relaxation factor manually defined.

$$N_f = \begin{cases} N_t & F_v \leq F_s/100 \\ N_t \left(\frac{a}{F_v} + b \right) & F_v > F_s/20 \end{cases} \tag{2.26}$$

2.4 Flow analysis

One of the purposes of the application of the mPOD to experimental data from axial turbomachines and therefore one of the goals of this project, consists on detecting flow patterns in the flow field. These patterns can be the explanation to some unsteady phenomena occurring in the hub region of axial compressors or also in the flow interface between the combustor and the high-pressure turbine. VKI is currently involved in a project aiming at characterizing the effects of cavity flows on the performance of a modern high-pressure compressor, leading to the necessity of describing their unsteady and spatial evolution both in the cavity and the main stream. In the following, a brief review of these topologies will be provided.

First of all, it should be commented the two different available technologies for the sealing of the stator integration. On the one hand, the cantilevered stator is the integration used in the last decades and it offers a flow behaviour similar to the rotor tip flow topology. On the other hand, a shrouded stator is a more complex solution used recently since it allows leakage flow reduction and its management. Both techniques have their pros and cons, for example a general comment is that the cantilevered stator improves the stall margin of the stage but the pressure rise capabilities are lower than the shrouded stator. Moreover, the shrouded stator not only has a more complex integration but also the mechanical design.

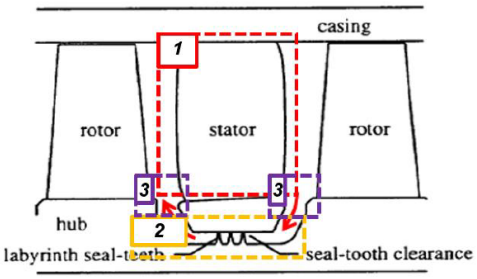

Figure 2.6: Regions of the analysis

In the following paragraphs, a review of the most significant flow features in a shrouded stator is done as well as some comments about their impact on the performance of the axial compressor. The analysis is done by parts dividing the stator stage in different areas like is showed in the Figure 2.6.

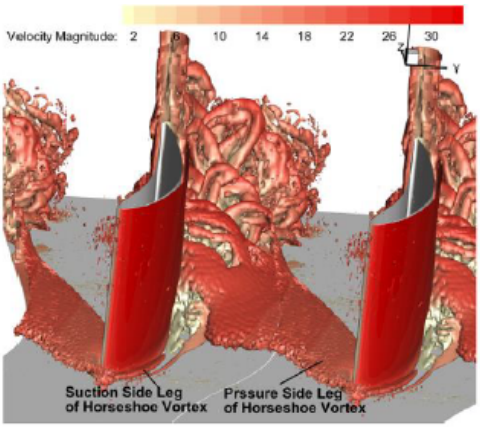

Figure 2.7: Horseshoe vortex evolution

In the first section or the blade passage, the main flow feature is the horseshoe vortex which pattern can be observed in the Figure 2.7. Its origin is caused by the hub boundary layer detachment originated by the adverse gradient forces. This gradient also originates the so called cross flow from the blade pressure side to the adjacent blade suction side. This horseshoe vortex is splitted into two legs downstream of the leading edge whose development is influenced by the pressure gradient and the cross flow. The leg placed at the suction side remains attached to the blade whereas the leg placed at the pressure side meets with the suction side of the adjacent blade. This generates the interaction between both horseshoes vortex and results in increasing the loss generation.

Another important flow feature originated in the blade passage is the phenomena called *hub corner stall* [9] and it is due to the simultaneous detachment of the blade boundary layer and the end wall boundary layer. Its formation is triggered by: the adverse pressure gradient originated in the blade passage, the cross flow and the skewness of the row inlet boundary layer. The inlet conditions are strongly affected by the operating point of the compressor since the incident angle is directly related with the loading operating point. Besides, this incidence also affects to the cross flow formation.

The sencond area to be analysed is the cavity and the flow through it. According to the existing literature, some authors claim that the stator cavity flow can be studied with three quantities: the leakage fraction, the leakage flow tangential velocity and the increasing in the total temperature in the cavity. The leakage fraction is a relation between the recirculating flow in the cavity and the main flow field. Otherwise, the leakage flow tangential velocity is created by the dragged flow due to viscous effects. Finally, the increase in the total temperature also called windage heating is generated by the flow pass through the cavity. The Figure 2.8 corresponds to CFD results that confirm the jet contraction and the vortices developed between the seal teeth. The windage heating phenomenon is associated with the seal gap so that smaller clearances increase the temperature in the cavity.

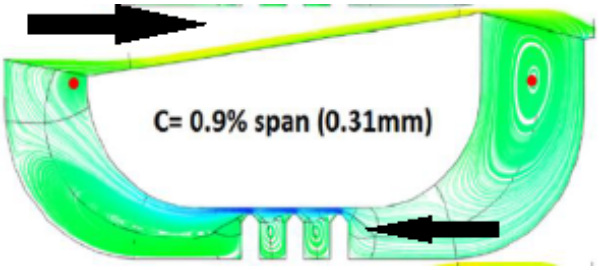

Figure 2.8: Contraction of the jet flow at the rim seal

In the region close to the beginning and the end of the cavity, a vortex appears as a result of the interaction between the cavity flow and the main stream. According to the Figure 2.9, the upstream vortex seems to be influenced by the seal gap and therefore by the leakage fraction. A higher seal gap means a higher leakage fraction and it results in the ejection of the main vortex outside of the trench. Contrarily, the vortex located downstream is not affected by the seal gap.

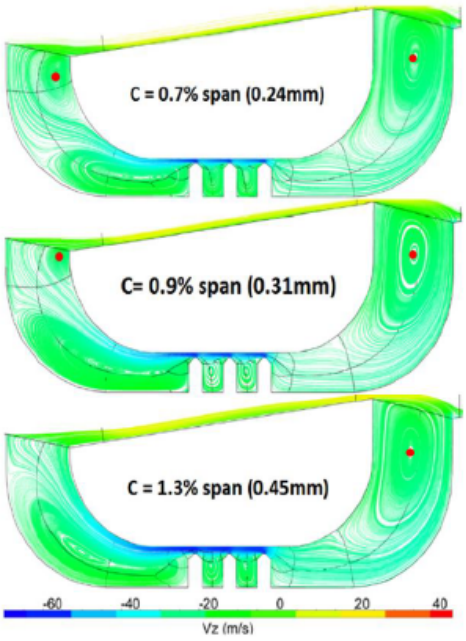

Figure 2.9: Interaction vortex

The behaviour of the upstream vortex directly influences the inlet conditions of the stator since it provokes skewness in the boundary layer of this region. This is critical for the blade passage performance and related to the cross flow formation. The leakage flow also induces blockage in the inlet low span region mainly due to the vortex. Just as some authors claim a higher seal gap a higher leakage fraction and this results in an increase in the blockage at the blade trailing edge. The influence of the leakage fraction quantity in the compressor performance is clear and in some results were found that a 1% increase in the seal tooth clearance it can be expected a 3% pressure rise penalty and a point drop in stage efficiency.

All the comments given above were connected to a single stage, but a real compressor can contain up to ten stages and therefore the loss propagation should be considered. The outlet conditions of one of the stages directly affect to the inlet conditions of the next stage. The

following stages losses have a component due to the non-matching inlet conditions and the losses of their own cavity. According to the literature, the efficiency drop are usually splitted into three different components: the efficiency drop to the non-matching inlet conditions in the rotor, the drop due to the pressure loss in the stator, and the efficiency drop due to the windage heating.

It is evident that the brief review done above is not enough to understand all the flow features around a compressor stage. Besides, the origin of most of these features is a complex combination of different phenomena. However, this slight introduction to the flow topologies is necessary for the later analysis of the mPOD results of the experimental case.

Chapter 3

Results

In the previous chapter §2, the fundamentals of POD and mPOD have been introduced. From this theoretical introduction, some key aspects of both techniques have been presented and explained such as some limitations that should be taken into account. It have also been presented some procedures to treat the data needed to properly apply POD or mPOD, since these data-driven decompositions require the data arranged in an orderly way.

In this chapter, the results obtained from the application of the POD and the mPOD are presented. With these results it will be possible to identify the weaknesses of the energy-based procedures like POD and the necessity of hybrid techniques that combine the energy-based principles with the frequency analysis. Both techniques have been applied to the same synthetic cases. These cases have been purposely defined to test the applicability of both techniques in different situations and conditions.

After the synthetic cases, POD and mPOD have been used with the actual pressure field on an axial turbine. These data has been obtained in different experiments conducted in the DLR facilities. Since in this case, the decomposition has been made over the pressure field instead of the velocity field some little modifications have been done in the code. Before computing the decompositions a pre-processing procedure had to be done as well as a deep analysis of the frequency content of the signal acquired in order to improve the results and its analysis.

In order to analyse from a different perspective the data-driven decompositions, a completely different experimental case has been included even though it is not related with the purpose of the project. The case studied is an experiment where the velocity field of an impinging jet onto a flat surface was measured with the PIV technique. A brief analysis of the results obtained after applying POD and mPOD is done. It should be mentioned that any of these techniques can be used as well with numerical data from computational simulations like CFD, in fact at the beginning of the project it was one of the objectives but the large time of these simulations made impossible its use.

3.1 POD: synthetic cases

Just as it has been commented before, the first step consists on testing the POD with a series of synthetic cases. Firstly, POD will be applied to this series of cases and in the next section mPOD will be applied to underline the differences in the results. This series of synthetic cases derives from an original one which has been modified with the purpose of testing some aspects and provide the best explanation of some phenomena to take into account before using the techniques.

The synthetic case consists on a circular domain described in two-dimensional polar coordinates. This domain is a simple model of an axial compressor transversal section. In fact, a more accurate model of the axial compressor section would be an annulus but in this section the importance lies on the comparison between the different models obtained from the modal decomposition and the real solution previously defined.

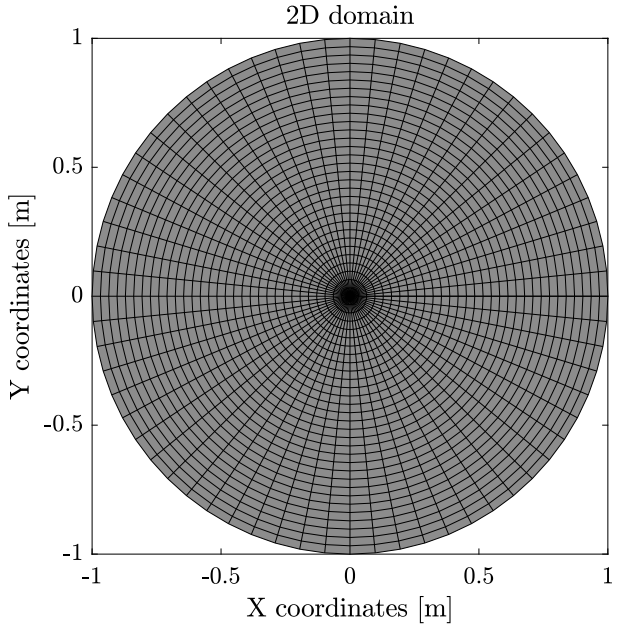

Figure 3.1: two-dimensional domain

The domain used in the synthetic cases is showed in the Figure 3.1. In this domain, the velocity field of the flow is known and the POD and mPOD have been applied to reconstruct that flow field with a finite number of modes.

N_θ	$2^6 + 1$
N_{rad}	2^5
N_{nodes}	2080
R	$1\,m$
t_{end}	$2\,secs$

Table 3.1: Domain data

The parameters that define the domain are shown in the Table 3.1 where N_θ and N_{rad} are referred to the number of discretizations done in each coordinate. In this table, the time of the simulation is also displayed. With the geometry information, the matrix of areas is computed to do the averaging process.

$$
\begin{aligned}
V_\theta &= A \cdot r \cdot cos(\kappa_1 \theta + \omega t) \\
V_r &= A \cdot sin^2\left(\frac{\theta}{2} + \omega t\right)
\end{aligned}
\tag{3.1}
$$

The velocity field is composed by the tangential and the radial components $\vec{V} = (V_\theta, V_r)$. The expressions of each component in 3.1 are known and dependent on the coordinates of the domain. The constants A, κ_1 and the frequency ω are chosen in each case according to what has to be demonstrated.

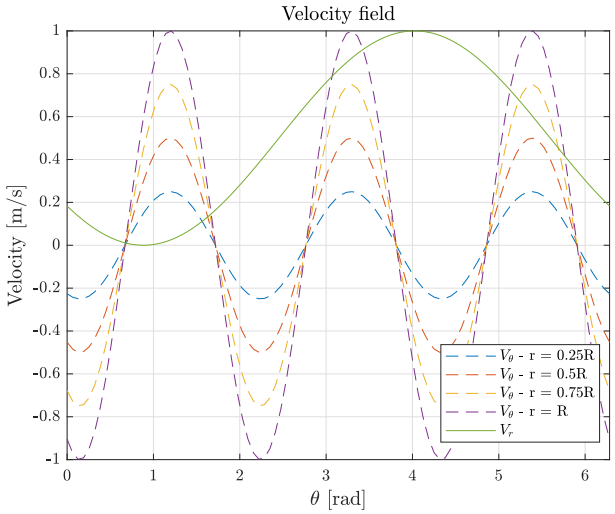

Figure 3.2: Velocity field

In the Figure 3.2, the velocity components of a certain case have been plotted in a polar coordinates graph for a certain time. It can be appreciated the dependence on the radial coordinate of the radial velocity V_r which has been plotted for four different radial positions. However, the tangential velocity V_θ is only dependent on the angular position.

3.1.1 Data arrangement

As it was mentioned in the Chapter §2, the way followed to arrange the data would be the same to follow to reshape back the spatial and temporal basis. The procedure followed in the synthetic case is quite different to the one followed with the experimental data, that is the reason why a section is dedicated to explain it.

In this case, for each time both components of the velocity field are computed in the whole domain and stored in a two-dimensional matrix in which each position corresponds to a point of the spatial grid. For example, for the time t_j of the simulation the matrix of the tangential velocity V_θ is like the one showed in 3.2. For the matrix of the radial velocity V_r the shape is identical.

$$
D_{V_\theta}^{t_j} = \begin{bmatrix}
V_\theta[r_1, \theta_1] & V_\theta[r_2, \theta_1] & \cdots & V_\theta[r_{N_R}, \theta_1] \\
V_\theta[r_1, \theta_2] & \ddots & & \vdots \\
\vdots & & \ddots & \vdots \\
V_\theta[r_1, \theta_{N_\theta}] & \cdots & \cdots & V_\theta[r_{N_R}, \theta_{N_\theta}]
\end{bmatrix}_{N_\theta \times N_R}
\tag{3.2}
$$

The next step is arrange the matrix $D_{V_\theta}^{t_j}$ and its equivalent $D_{V_r}^{t_j}$ in one column to finally have a two-dimensional matrix in which each column was a time sample. The matrix in 3.3 shows the procedure followed for a generic time sample t_j. The vector generated has a length equal to the number of spatial points $N_{samples} = N_{rad}N_\theta$.

$$D_{V_\theta}^{t_j} = \begin{bmatrix} V_\theta[r_1, \theta_1] \\ \vdots \\ V_\theta[r_{N_R}, \theta_1] \\ V_\theta[r_1, \theta_2] \\ \vdots \\ V_\theta[r_{N_R}, \theta_2] \\ \vdots \\ V_\theta[r_{N_R}, \theta_1] \\ \vdots \\ V_\theta[r_{N_R}, \theta_{N_\theta}] \end{bmatrix}_{N_{samples} \times 1} \tag{3.3}$$

From the expressions showed above, the final data matrix is shaped by as many columns as time samples, and each column is the vertical concantenation of $D_{V_\theta}^{t_j}$ and $D_{V_r}^{t_j}$ like in 3.4. The dimensions of the final data matrix are $(2N_{samples} \times N_t)$ due to the velocity field is composed by two components. Let's imagine in the velocity field three components are considered, the dimensions of the D matrix would therefore be $(3N_{samples} \times N_t)$.

$$D = \begin{bmatrix} \begin{bmatrix} D_{V_\theta}^{t_1} \end{bmatrix} & \cdots & \begin{bmatrix} D_{V_\theta}^{t_{N_t}} \end{bmatrix} \\ \begin{bmatrix} D_{V_r}^{t_1} \end{bmatrix} & \cdots & \begin{bmatrix} D_{V_r}^{t_{N_t}} \end{bmatrix} \end{bmatrix}_{2N_{samples} \times N_t} \tag{3.4}$$

3.1.2 Normal case

The first case to be solved applying the POD is a normal case in which the flow field is composed by a tangential and a radial component. Both expressions of the velocity are described by the equations 3.1. The constants that define the velocity field are presented in the Table 3.2.

A	50
ω	$40\,rad/s$
κ	$35\,rad/m$

Table 3.2: Constants of the flow field

The first step consists on analyzing the energy content of the basis obtained from computing the Singular Value Decomposition of the correlation matrix. The criteria followed for this case and the following ones take into account the energy contribution of each mode in comparison with the first one, that is the most energetic. This statement is always true since both techniques sort the computed modes in descending order of energy. The graphics used for these analyses plot the results of the ratio σ_r/σ_1 for $r = 1, 2, \ldots N_m$, where N_m makes reference to the total number of modes obtained in the Singular Value Decomposition.

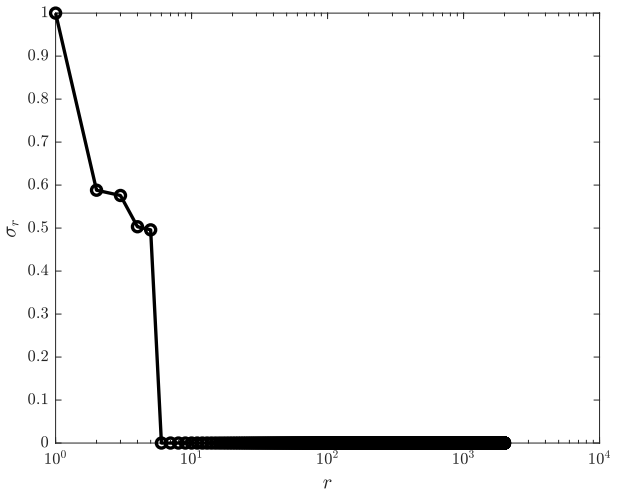

Figure 3.3: Energy content

The Figure 3.3 shows that for this case the first five modes contain most of the energy of the system. Actually, these modes represent almost the 99% of the total energy.

Once the number of modes is selected, the temporal and structural basis are computed. The figures below show the temporal structures, the figures on the right represent the temporal evolution whereas the figures on the left represent the frequency content of each mode obtained with the Fast Fourier Transform (FFT). It should be mentioned that both graphics have been normalized and therefore the ordinate axis is dimensionless.

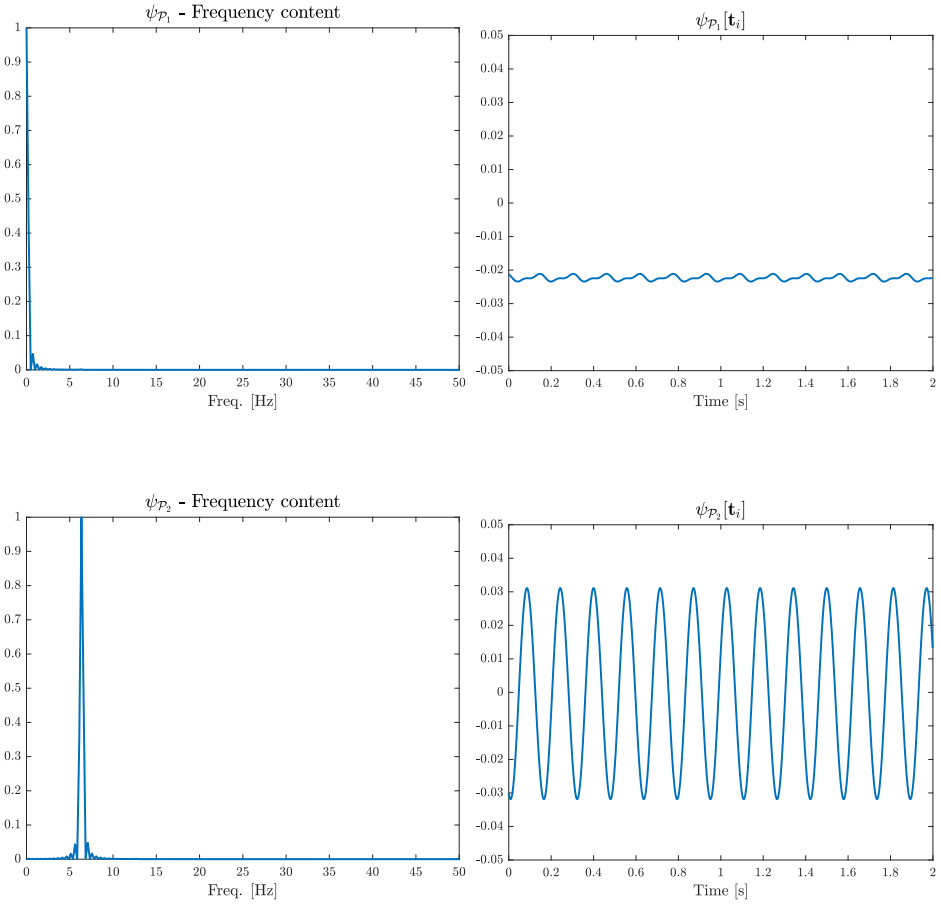

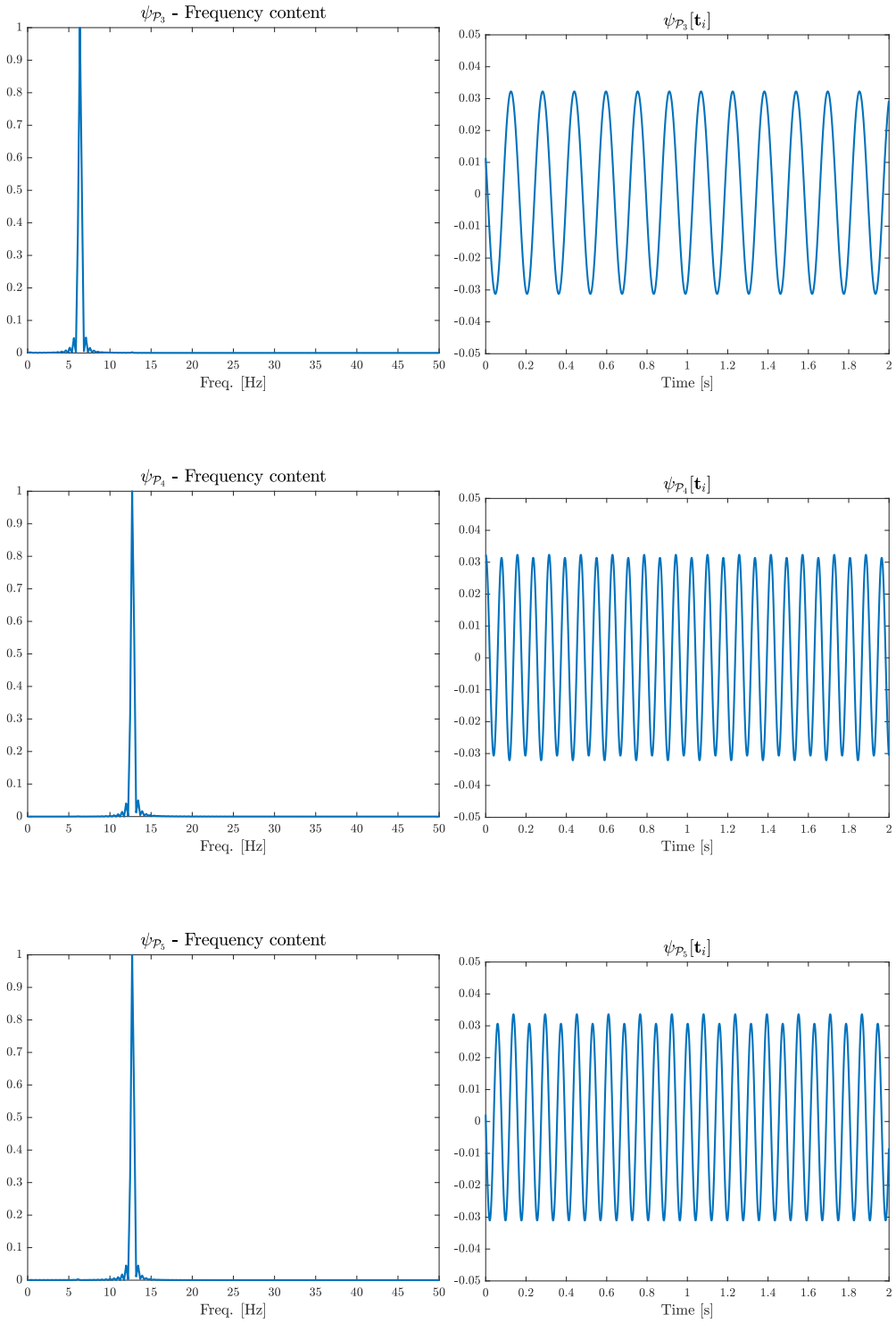

Figure 3.4: Modes

In the figure corresponding to the first mode, it can be observed that it represents the mean value of the velocity field since the frequency is null and the oscillations are very small around a constant value.

Also, it can be observed that the rest of the modes has a sinuosoidal evolution and they are paired. The second and third mode have the same frequency content located at $f \simeq 6\,Hz$ which

corresponds with the frequency ω imposed. However, the temporal evolution shows a $\pi/2$ delay because this mode is related to traveling structures. This phenomena can be clearly observed in the Figure 3.5 where the modes $\psi_{\mathcal{P}_2}$ and $\psi_{\mathcal{P}_3}$ have been plotted in the same graphic. The $\pi/2$ delay is evident and it also is present in the fourth and fifth mode. However, its frequency is $f \simeq 13\,Hz$ which leads to think that these two modes are harmonics of the previous ones.

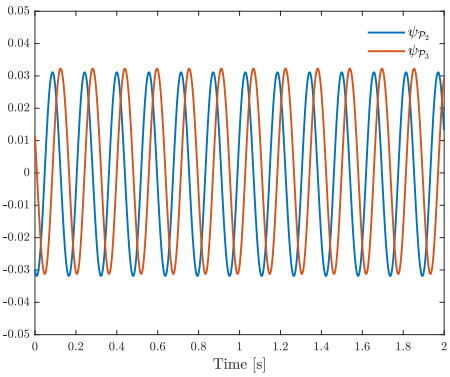

Figure 3.5: Spectral mixing in $\psi_{\mathcal{P}_2}$ and $\psi_{\mathcal{P}_3}$

If the sixth mode is considered, even though is not necessary, it can be observed that this mode contains frequency content in the whole spectra and in comparison with the rest of the modes, the temporal evolution seems to be noisy or chaotic. But as it shows the Figure 3.3, its energy content is almost fifteen magnitude orders lower so the influence in the decomposition of the system is negligible.

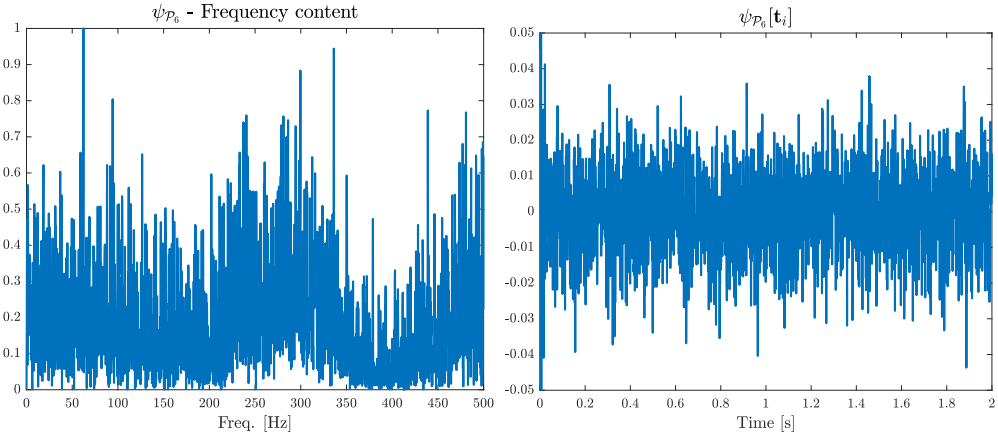

Figure 3.6: Sixth mode

The spatial structures of the first five modes are showed below. It can be observed that the second and third mode are paired as well as the fourth and fifth. These two pairs of modes are related to traveling structures and the $\pi/2$ delay commented before is also presented in the spatial structures.

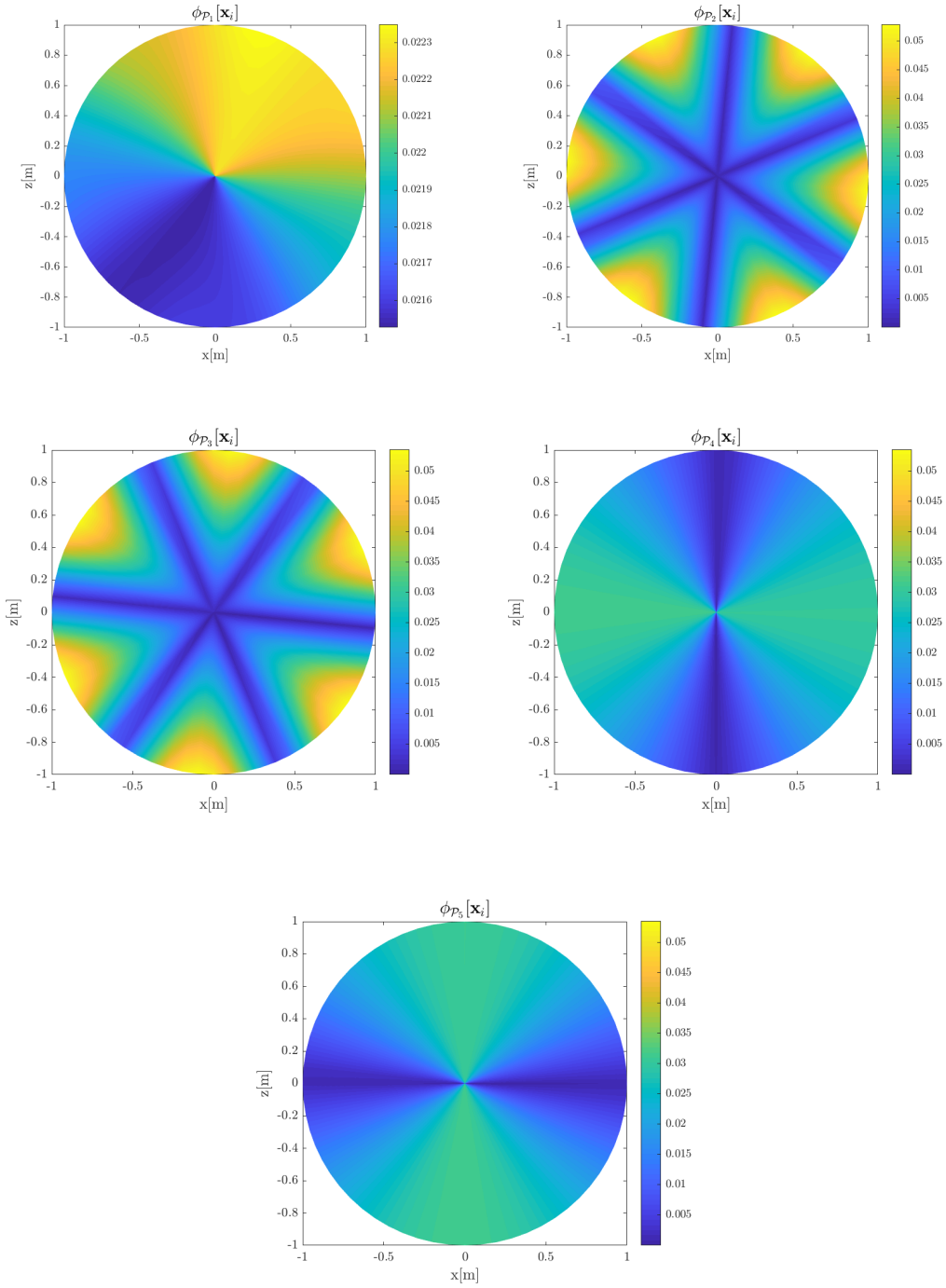

Figure 3.7: Spatial structures

One possible additional step could be the reconstruction of the flow field from the modes computed to obtain a Reduced Order Model (ROM). This is one of the most useful applications that this type of techniques have. Following the expression 3.5, where N_m makes reference to the number of modes to retain, and then arranging the data in the same way as the computed basis, it can be obtained a contour plot of the flow at a given time.

$$\bar{D} \simeq \sum_{r=1}^{N_m} \Psi_p \Sigma_p \Phi_p \tag{3.5}$$

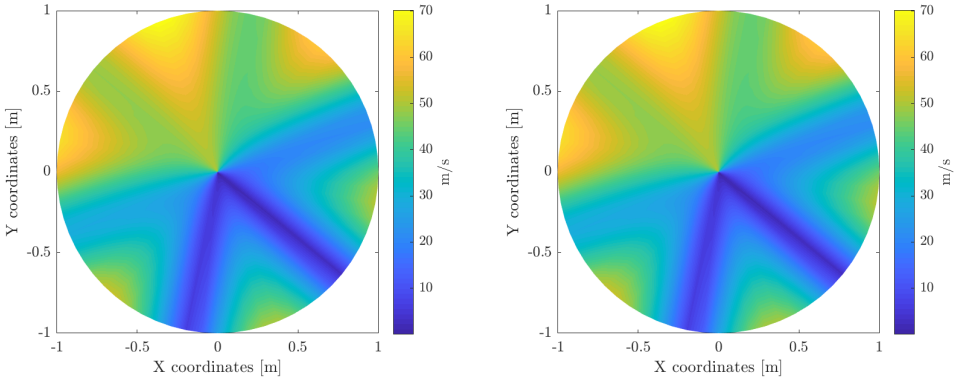

Figure 3.8: Original (left) versus approximated (right) flow field

In the Figure 3.8 are presented the contour plots of the flow field. On the left, it is the original flow field plotted from the original data matrix D whereas the approximation of the flow field is showed on the right. As it can be observed, both plots are identical and this can be confirmed with the results displayed in the Figure 3.9. This graphic evinces that considering the number of modes computed, the error commited is almost null.

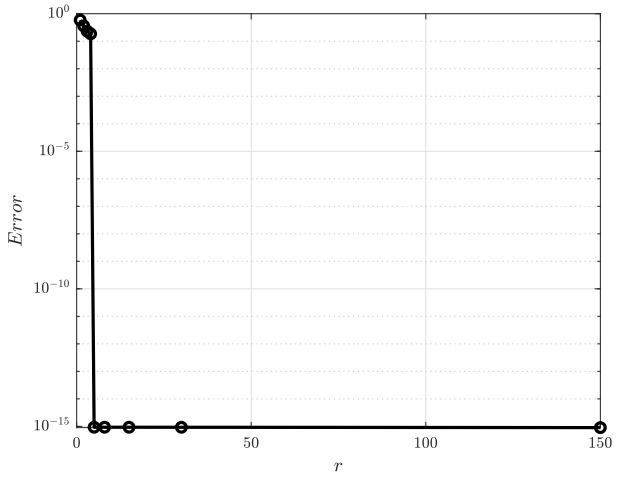

Figure 3.9: Convergence of the error

Due to the simplicity of this case the POD modes considered seem to reproduce quite well the flow behaviour in terms of velocity. The next cases put the POD throught its paces to analyse the limitations of the technique.

3.1.3 Noisy case

This second case consists on applying the Proper Orthogonal Decomposition over the same synthetic case than before but including a noise contribution to each component of the velocity field. The noise considered is a Gaussian noise characterized by an standard deviation of $\sigma = 80$. The energy content of the different modes is showed in the Figure 3.10 in the same way as in the previous case. It can be observed that starting at the sixth mode, the energy content decays and therefore the sixth first modes accumulate most of the energy.

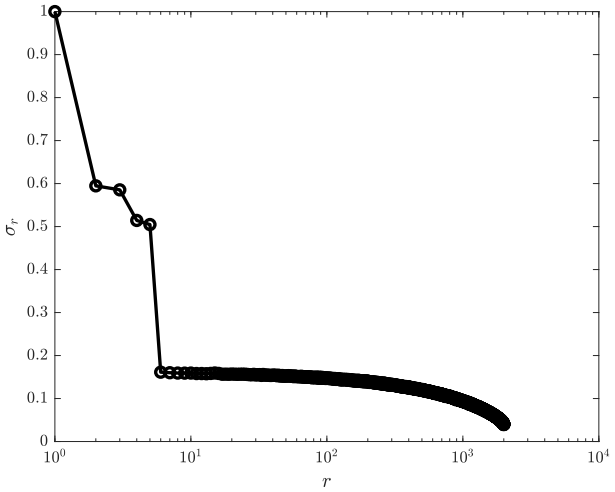

Figure 3.10: Energy content

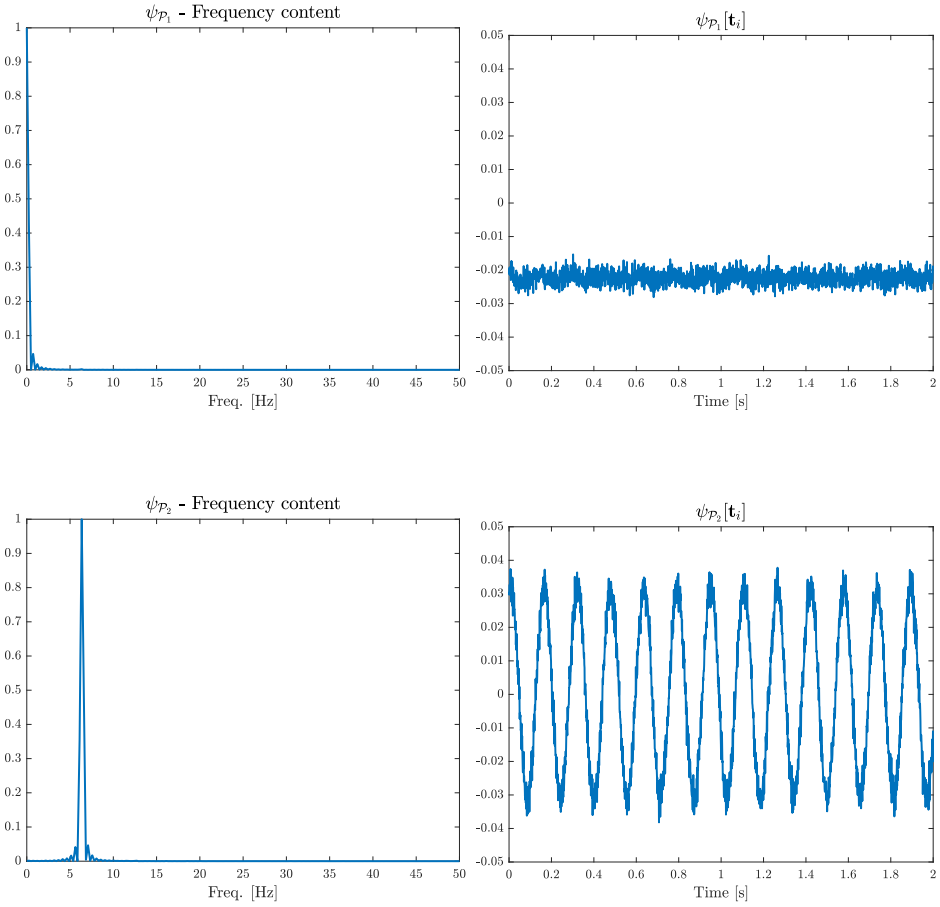

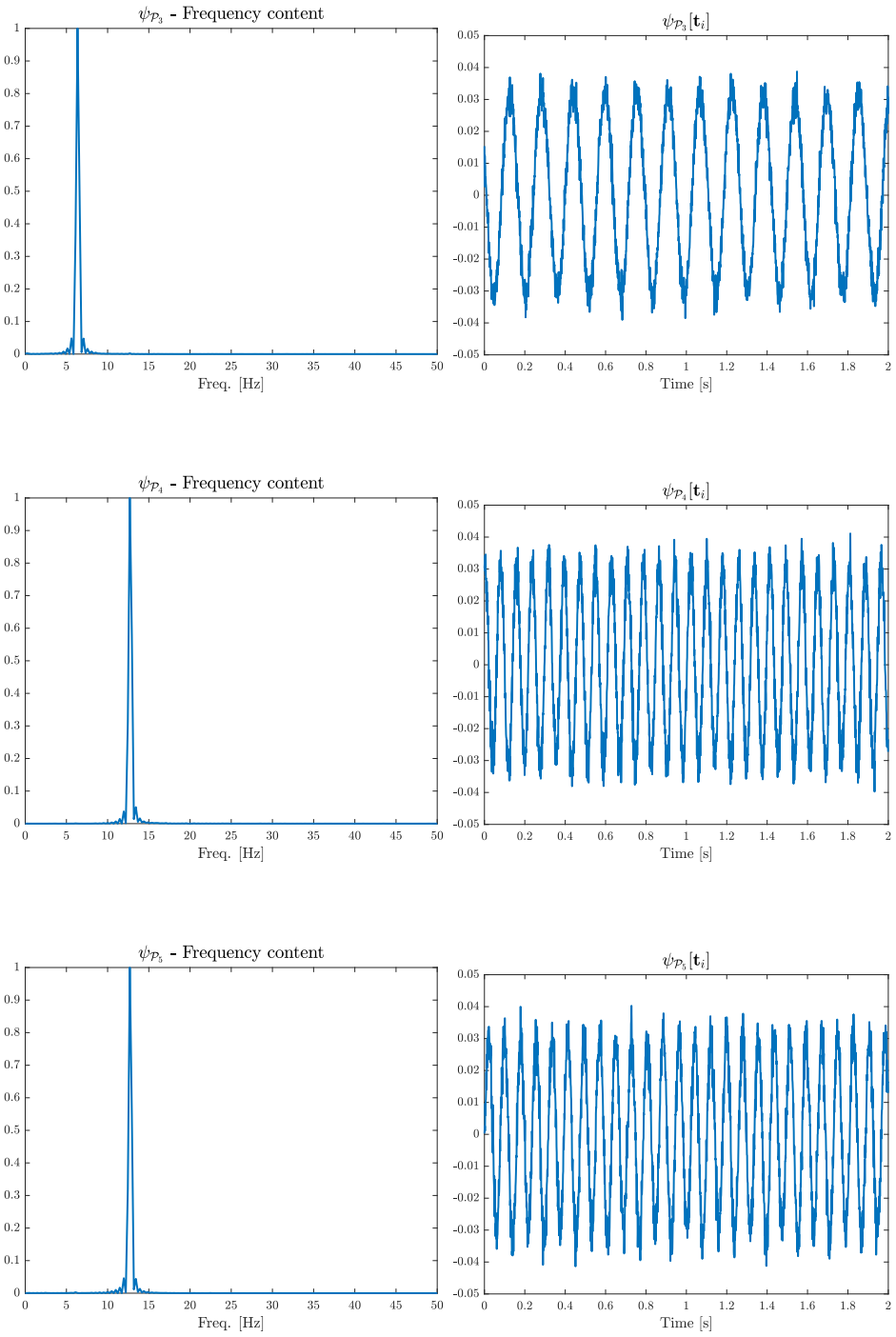

Figure 3.11: Temporal basis of the POD modes

In the Figure 3.11 are showed the results of the POD applied to the noisy case. As it can be observed, the results in terms of frequency content are the same as in the previous case: the second and third mode have the peak of frequency at $f \simeq 6Hz$, whereas the fourth and fifth mode at $f \simeq 13Hz$. This is because the flow field is described by the same velocity expressions. Otherwise, the temporal evolution of the modes are visibly affected by the noise. This is the problem commented in the Chapter §2: since the white noise is spanned along the full frequency range with the same energy spectra, the POD modes cannot filter it.

The pairing between the second and third mode, as well as between the fourth and fifth mode can be observed in both graphics as well as in the spatial structures. In this case, showing the spatial structures of the POD modes do not contribute specially to the understanding of the results because they are identical to the previous case with some distortion caused by the noise. This is the reason why these graphics are not presented. In the same way as in the previous case, the temporal series of the second $\psi_{\mathcal{P}_2}$ and third $\psi_{\mathcal{P}_3}$ mode have been togetherly plotted to clearly appreciate the delay commented.

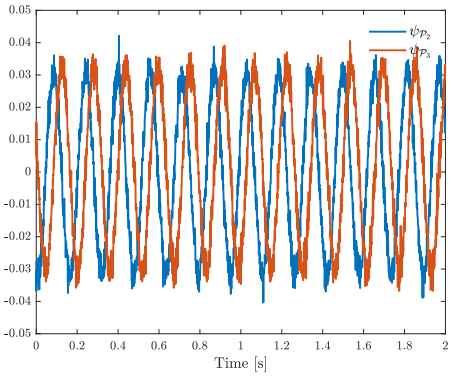

Figure 3.12: Spectral mixing in $\psi_{\mathcal{P}_2}$ and $\psi_{\mathcal{P}_3}$

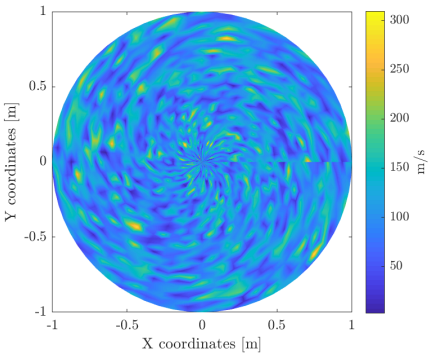

(a) Original flow field

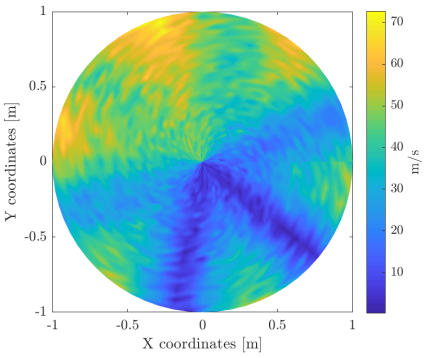

(b) Approximated flow field $N_m = 6$

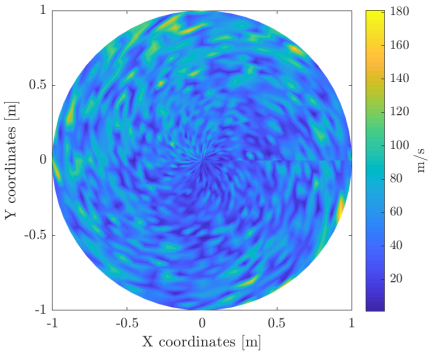

(c) Approximated flow field $N_m = 150$

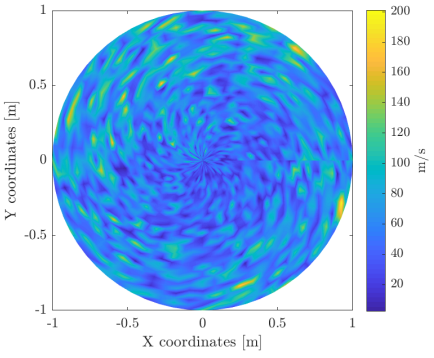

(d) Approximated flow field $N_m = 250$

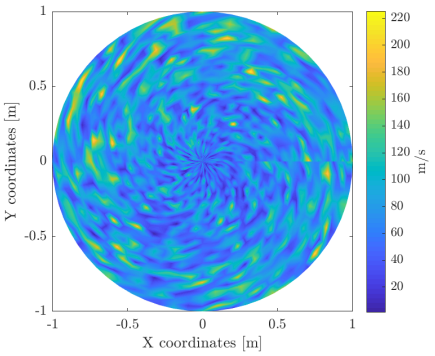

(e) Approximated flow field $N_m = 500$

Figure 3.13: Different reconstructions of the flow field

In the same way than in the previous case, the flow field can be reconstructed from the POD modes. The Figure 3.13 show the comparison between the original flow field and some of the reconstructions obtained. In this case, the reconstruction obtained from the six POD modes computed is really different than the original flow field. This is because the first five modes are the most energetically representative modes but altought they contain almost the 85% of the total energy, this is not enough to reproduce the original flow field.

Besides, the not considered modes are representative of the noise and considerably distort the flow field. In terms of energy, these modes are not significant since the evolution of the energy is very slow (see Figure 3.10). This can be demontrated with the rest of the graphics, they show different reconstructions with an increasing number of modes, and as it can be seen even with $N_m = 500$ the flow field is not equal. This is due to each mode contribute to the distortion of the flow field. What is more, the flow field modelled with $N_m = 5$ is very similar to the flow field of the previous case

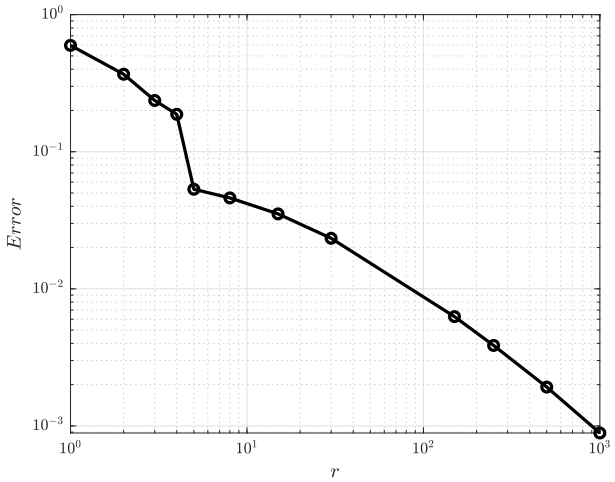

Figure 3.14: Convergence of the error

The graphic above explain the phenomena previously commented. As can be observed, considering a very high number of modes $N_m = 1000$, the error obtained is high in comparison with the results of the previous case. The noise added to the original signal is the cause of this. Although with a few modes the energy computed was high, the reconstruction of the flow field requires a higher number of modes even though its energy content was lower.

3.1.4 Same energy case

In the theoretical introduction of the POD in §2.1 has been explained the basis of this technique and that is a energy-based method. This principle leads to one of the main limitations of the method that consists on POD being incapable of distinguish between largely different scales with similar energy content. This problem usually causes spectral mixing in the different POD modes.

The next synthetic case has been developed to test and demonstrates this limitation. The velocity field in this case is composed by the tangential and radial component, each one defined by three contributions called *velocity modes* as in 3.6.

$$\begin{aligned} V_\theta &= \overbrace{A_{\theta_1} \cdot r \cdot cos(\kappa_1\theta + \omega_1 t)}^{V_{\theta_1}} + \overbrace{A_{\theta_2} \cdot sin(\omega_2 t)}^{V_{\theta_2}} + \overbrace{A_{\theta_3} \cdot cos^2(\omega_3 t + \kappa_3\theta)}^{V_{\theta_3}} \\ V_r &= \underbrace{A_{r1} \cdot sin\left(\frac{\theta}{2} + \omega_1 t\right)}_{V_{r_1}} + \underbrace{A_{r2} \cdot cos(\omega_2 t)}_{V_{r_2}} + \underbrace{A_{r3} \cdot r \cdot cos^3(\omega_3 t + \kappa_3\theta)}_{V_{r_3}} \end{aligned} \tag{3.6}$$

These modes are in turn characterized by largely different frequencies and constants showed in the Table 3.3.

A_{θ_1}	25	ω_1	$2\,rad/s$
A_{θ_2}	10	ω_2	$50\,rad/s$
A_{θ_3}	80	ω_3	$400\,rad/s$
A_{r_1}	5	κ_1	$35\,rad/m$
A_{r_2}	50	κ_2	$0\,rad/m$
A_{r_3}	25	κ_3	$12\,rad/m$

Table 3.3: Constants of the flow field

Each temporal contribution is arranged in a different data matrix whose linear combination gives as a result the final data matrix. In 3.7 is showed how it would be that process.

$$D = \begin{bmatrix} [D_{\theta_1} + D_{\theta_2} + D_{\theta_3}] \\ [D_{r_1} + D_{r_2} + D_{r_3}] \end{bmatrix} \tag{3.7}$$

The different contributions to the velocities expressions accomplish with the requirement of having different frequencies contributions but it is necessary to impose that all the contributions have a similar energy content. This energetic requirement has been achived modifying the norm of each data matrix. As a example of the process, in 3.8 is showed for two of the components D_{θ_1} and D_{r_2}.

$$\begin{aligned} D^*_{\theta_1} &= \frac{\|D_{\theta_1}\| + \|D_{\theta_2}\| + \|D_{\theta_3}\|}{3\,\|D_{\theta_1}\|} D_{\theta_1} \\ D^*_{r_2} &= \frac{\|D_{r_1}\| + \|D_{r_2}\| + \|D_{r_3}\|}{3\,\|D_{r_2}\|} D_{r_2} \\ D^* &= \begin{bmatrix} [D^*_{\theta_1} + D^*_{\theta_2} + D^*_{\theta_3}] \\ [D^*_{r_1} + D^*_{r_2} + D^*_{r_3}] \end{bmatrix} \end{aligned} \tag{3.8}$$

Once all the contributions have the same energy content, the data matrix is re-assembled and POD applied.

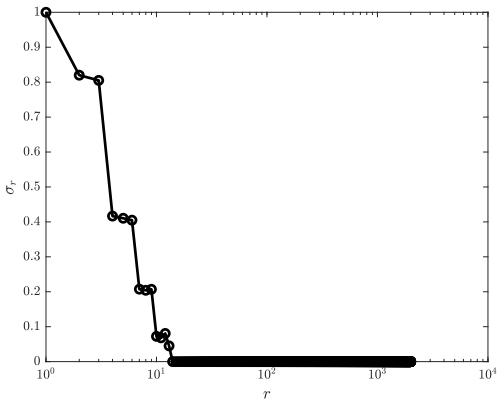

Figure 3.15: Energy evolution

The first step before deciding the number of modes is analyse the energy content of the POD modes obtained from the SVD of the correlation matrix. In the Figure 3.15 is showed the evolution of the energy according to the number of modes considered. As it can be expected in this case, due to the complexity of the velocity field and its contributions, the number of modes to consider has increased in comparison with the previous cases. The first thirteen modes contains almost the 95% of the total energy. With these number of modes computed, the results obtained are showed below. Due to the high number of modes obtained, only a limited number of them are presented in order to make easier the analysis and the comments.

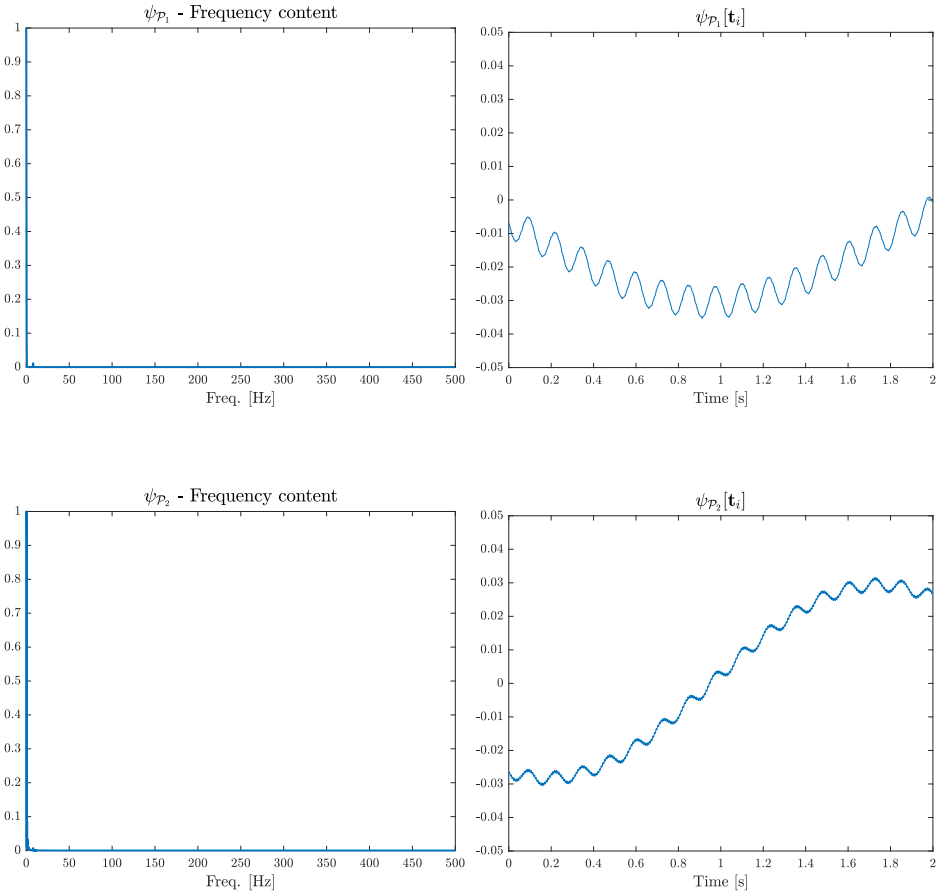

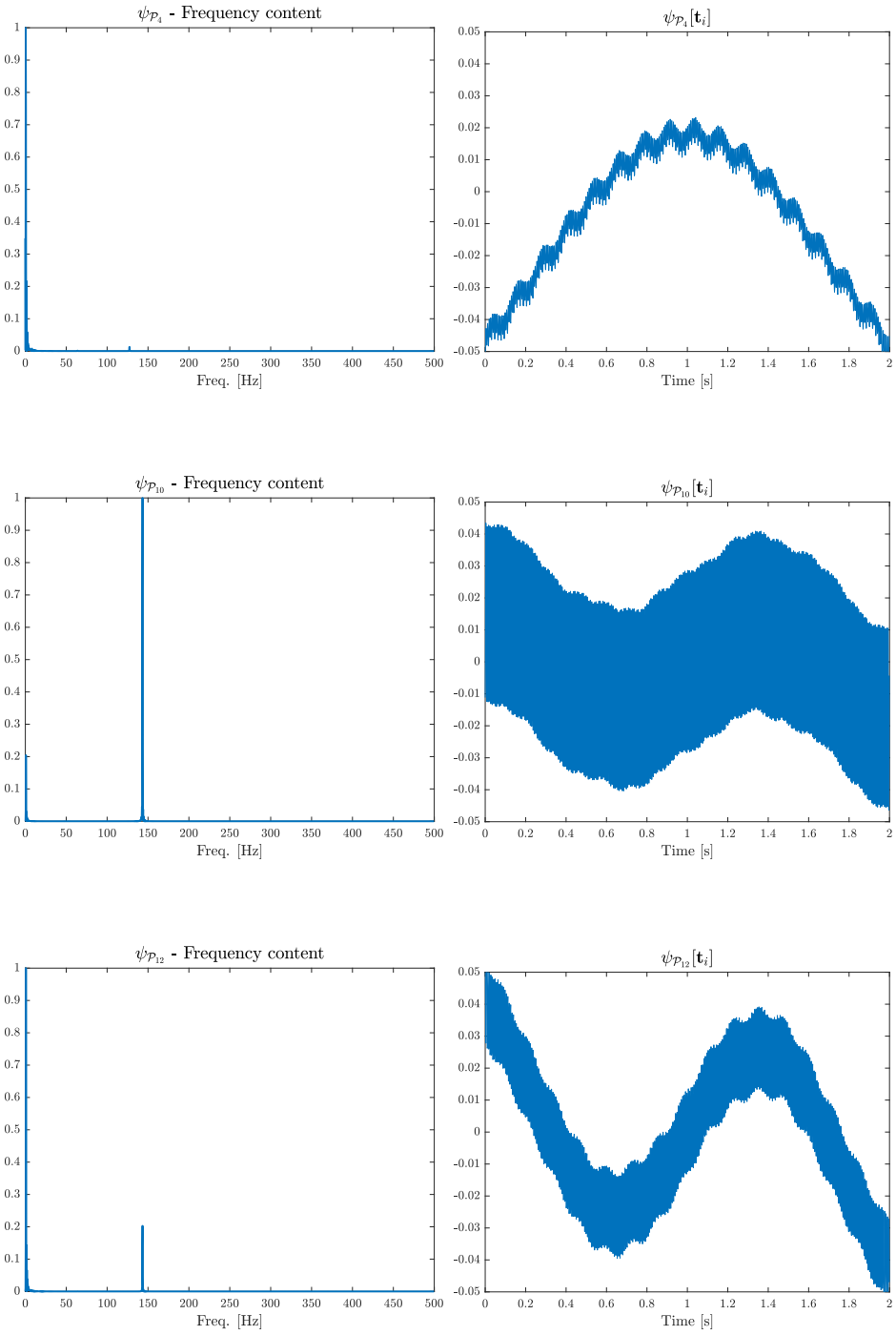

Figure 3.16: Temporal structures of POD modes

In the graphics above, the temporal structures of some of the POD modes are showed. In all of them it can be appreciated the spectra mixing phenomenon commented at the beggining. In some of these, the dominant frequency is the low one such as in the first, second, fourth and twelfth mode. Whereas in the tenth mode, the main frequency is the largest one. These differences can be observed in the frequency content graphic where the dominant frequency is represented by a higher peak, as well as in the time series plot.

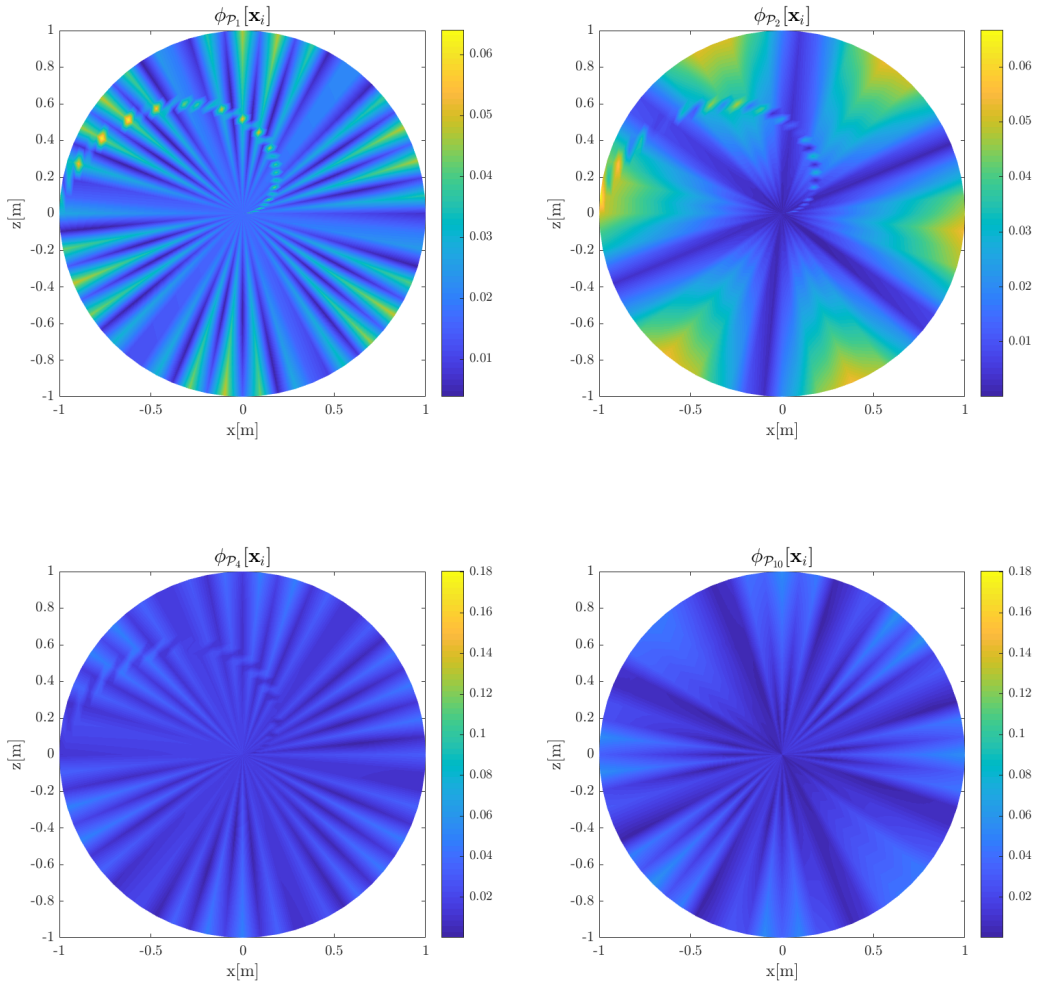

Figure 3.17: Spatial structures

For the interest of the reader, the spatial structures of some of the POD modes computed are showed in the Figure 3.17. Here, the spectral mixing it can be clearly observed since different phenomena are present in the spatial respresentations. This problem occurs since the data is projected along the temporal evolutions, and therefore the spectral mixing is propagated to the spatial structures.

As commented before, some of the modes are not showed to avoid an excess of graphics, but the results of these are quite similar. Some of the modes showed spectra mixing, whereas a few of them are represented by an harmonic related to the imposed frequencies. These results bring to light one of the most important limitations of POD consisting on being incapable of distinguishing between largely different scales with similar energy content. This can hinder the correct identification of interesting patterns or structures in some cases.

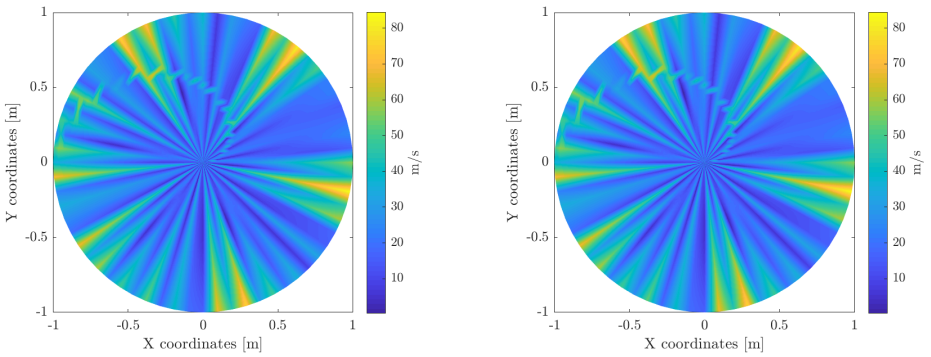

(a) Original flow field (b) Approximated flow field

Figure 3.18: Original versus reconstructed flow field

The reconstruction of the flow field showed in the Figure 3.18 is quite similar to the original one, also showed in the same plot. This is because though the POD modes present spectral mixing, and this can be a problem in some cases, the velocity field reconstructed from them is accurate.

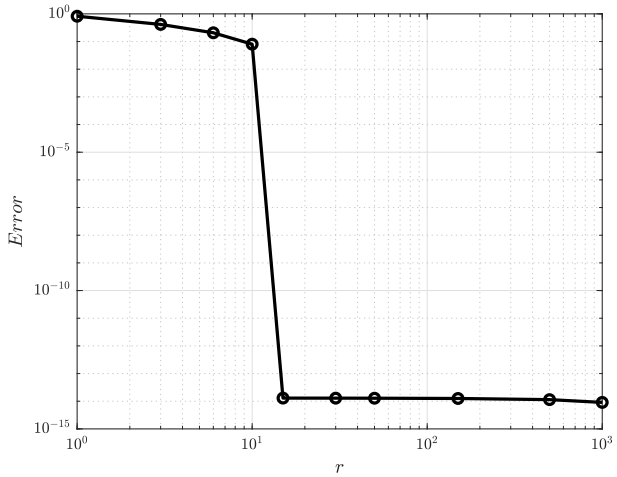

Figure 3.19: Error convergence

The Figure 3.19 shows the evolution of the error with the number of modes. The results reveal than the error abruptly decreases when more than ten modes are considered.

With this case, it has been able to demonstrate one of the most limiting problem that POD has. This technique is incapable of differenciating between different scales with a similar energy content. In the nature of the flows inside turbomachines, these phenomena are quite frequent and the limitation of the POD prevents the interpretation of the results.

3.2 mPOD: synthetic cases

After having studied some synthetic cases throught the POD, the next step is apply the mPOD to these same cases. The main objective is compare the results of both techniques and analyse the advantages of using mPOD instead of using POD. The first case is a normal case as, whereas the second and third case are a noisy case and a case in which the same energy content is imposed over the contributions of the velocity field.

3.2.1 Simple case

The first case in which the mPOD results are analysed is the normal case tested in §3.1.2 so the expressions of the velocities are the same. As a reminder, the Table 3.4 presents the different values of the constants that define the velocity field.

A	15
ω	$40\,rad/s$
κ	$35\,rad/m$

Table 3.4: Constants of the flow field

The arrangement of the data follows the same procedure as the explained in §3.1.1 since the flow field is described by the same expressions and the domain is also the same. In the case of mPOD, just as it was explained in the theoretical introduction of the method one of the first steps consists on analaysing the spectra of the correlation matrix to determine the frequencies of the filter bank.

The Figure 3.20 shows the spectra correlation matrix $\hat{K}$ and it can be observed that there are two dominant frequencies at $f \simeq (9,\, 12)\,Hz$. The filter bank has been designed to split the data into scales isolating these frequencies with the filter bank. The frequency splitting vector for the filter bank is $f_v = [10,\, 16]\,Hz$. With these frequencies, the correlation matrix is going to be splitted into three scales.

In the Figure 3.20 are also presented the transfer functions $\mathcal{H}_{\mathcal{L}_1}$ and $\mathcal{H}_{\mathcal{M}_1}$ used in this case. The first transfer function corresponds to the largest scale or what is the same to the low-pass filter, whereas the second one is the one referred to the first band-pass filter.

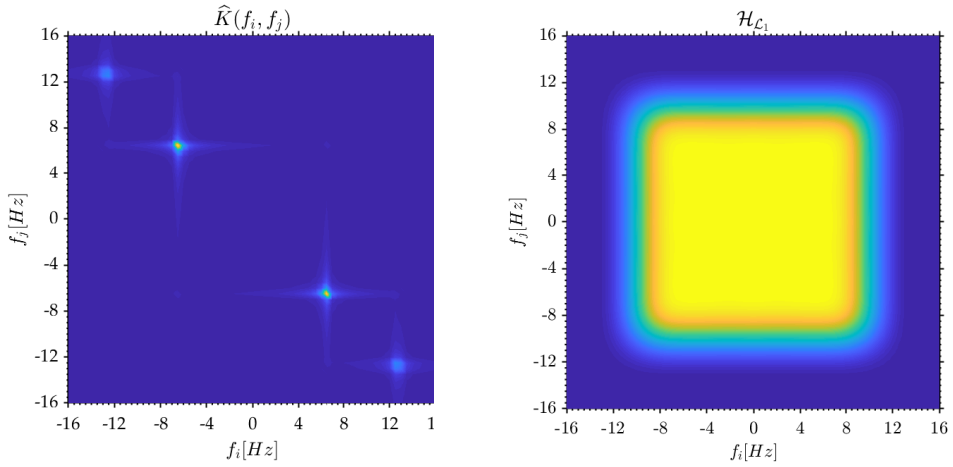

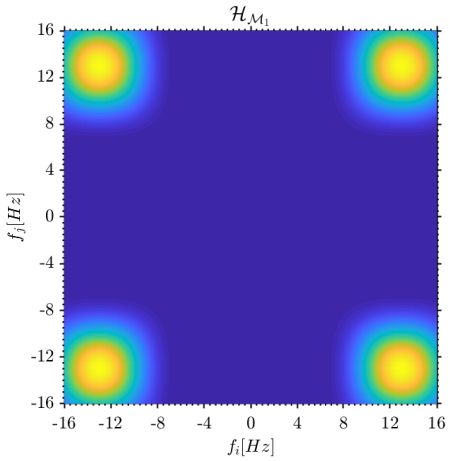

Figure 3.20: Spectra correlation matrix and transfer functions

The next steps of the technique after having defined the filter bank and have obtained the transfer function of the two-dimensional filters were described in §2.2. The number of mPOD modes to compute is defined after having analysed the evolution of the energy content showed in the Figure 3.21 which is very similar to the energy evolution of the POD analogous case. According to the graphic, the first five modes contain almost the 85% of the system energy so these are the modes to compute.

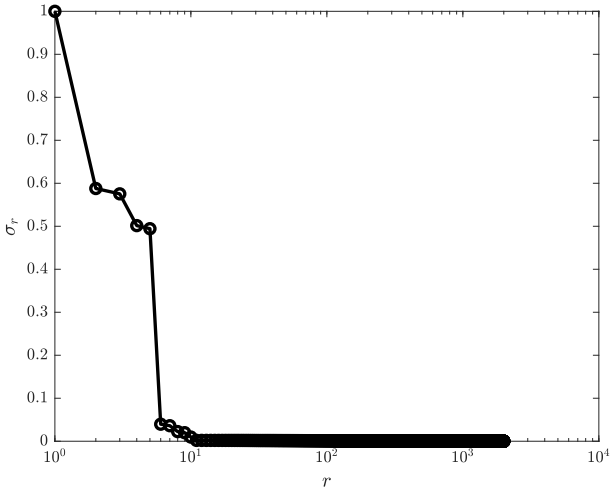

Figure 3.21: Energy content of the mPOD modes

In view of the results exposed above, it is clear that considering the first five modes contains most of the energy of the system. After having selected the number of mPOD modes to compute, the next step is obtain the structural and temporal basis of the decomposition. This basis have already been splitted into the different scales as well as sorted in terms of the energy content.

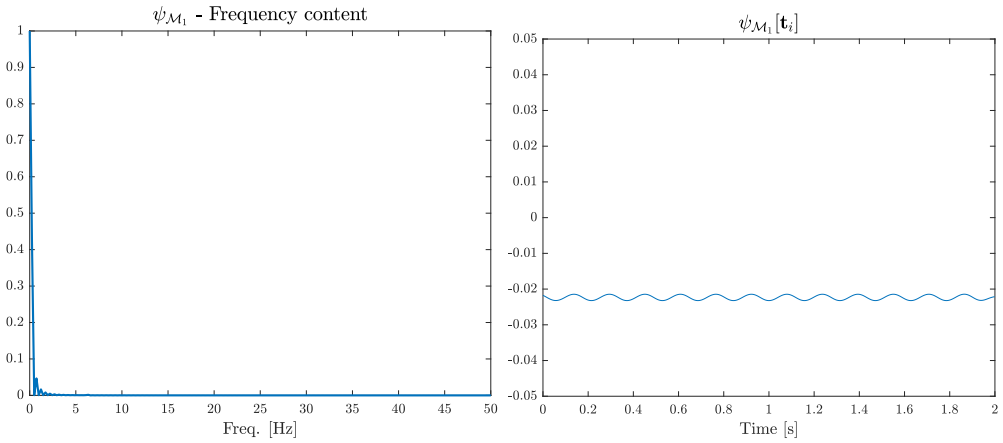
$\psi_{\mathcal{M}_1}$ - Frequency content
Freq. [Hz]
$\psi_{\mathcal{M}_1}[\mathbf{t}_i]$
Time [s]

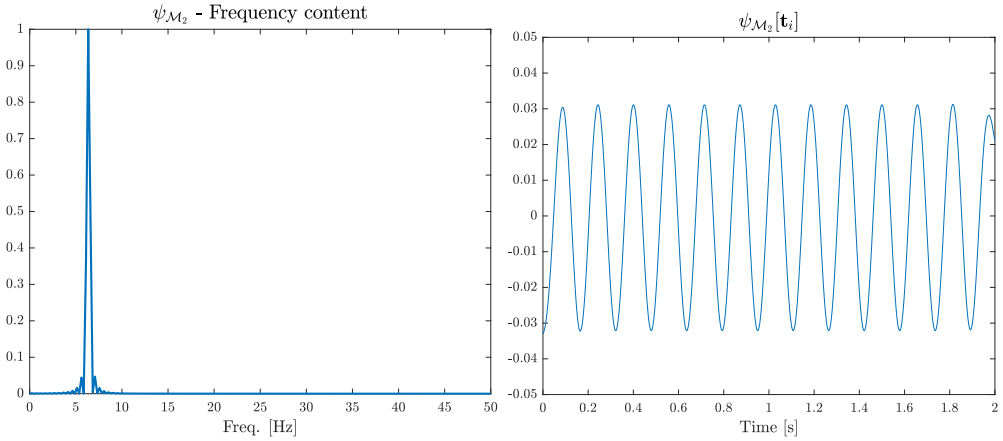
$\psi_{\mathcal{M}_2}$ - Frequency content
Freq. [Hz]
$\psi_{\mathcal{M}_2}[\mathbf{t}_i]$
Time [s]

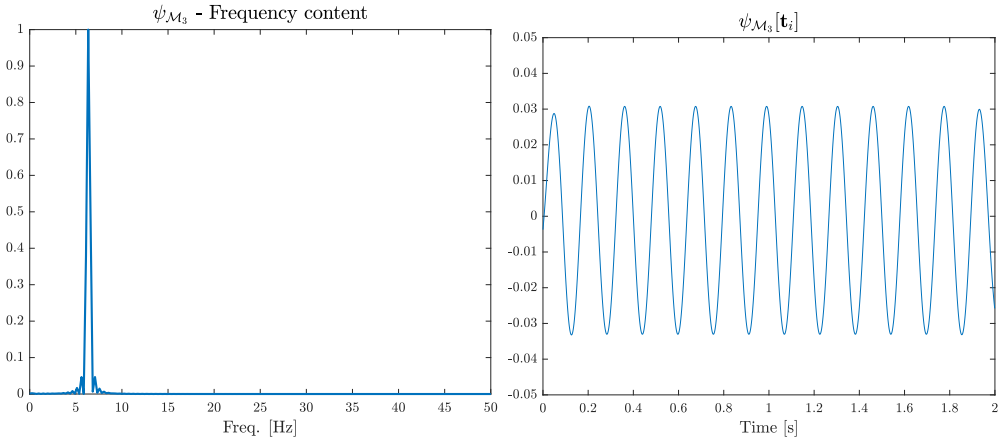
$\psi_{\mathcal{M}_3}$ - Frequency content
Freq. [Hz]
$\psi_{\mathcal{M}_3}[\mathbf{t}_i]$
Time [s]

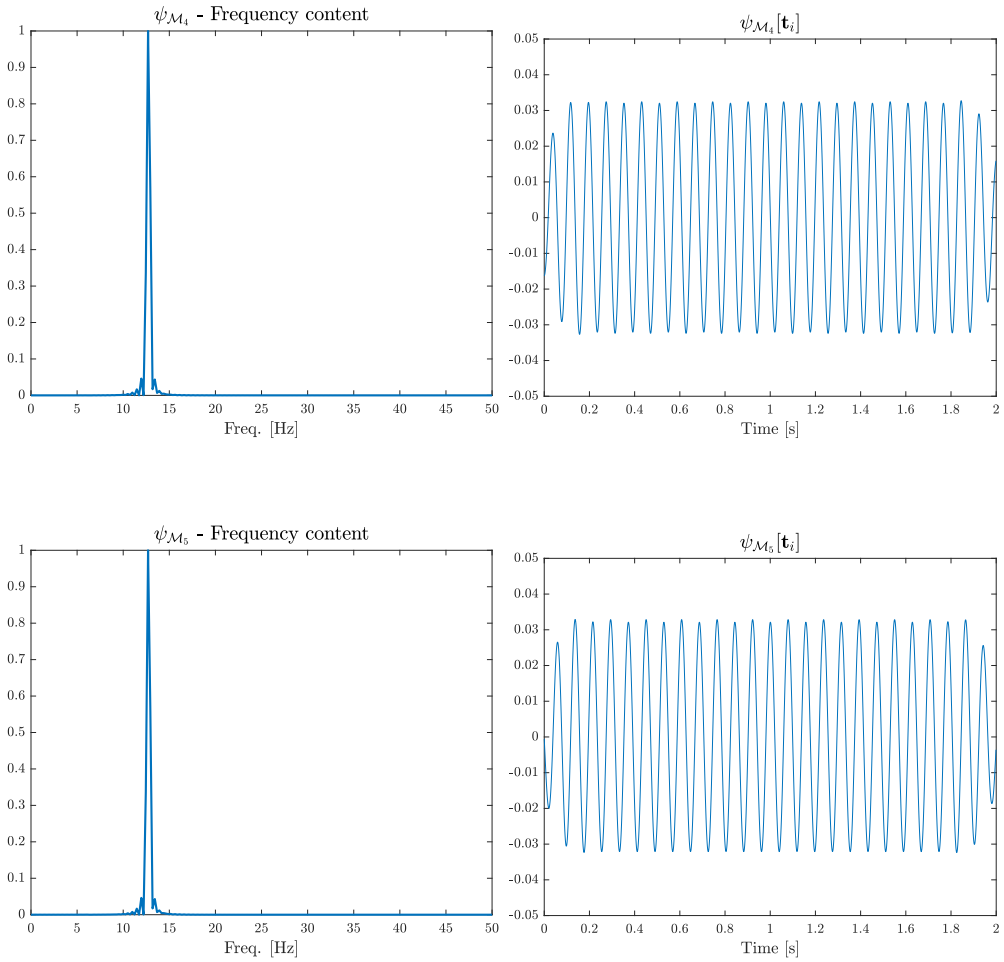

Figure 3.22: Temporal structures of the mPOD modes

The Figure 3.22 shows the temporal structures of the modes in terms of frequency content and the time series of each one. These basis are quite similar to the POD ones exposed in §3.1.2. The first mode corresponds to the mean value of the flow field since its frequency content is null. The second and third mode are paired since they have the same frequency content but they present the same delay than the POD modes. This phenomena also occurs in the fourth and fifth mode.

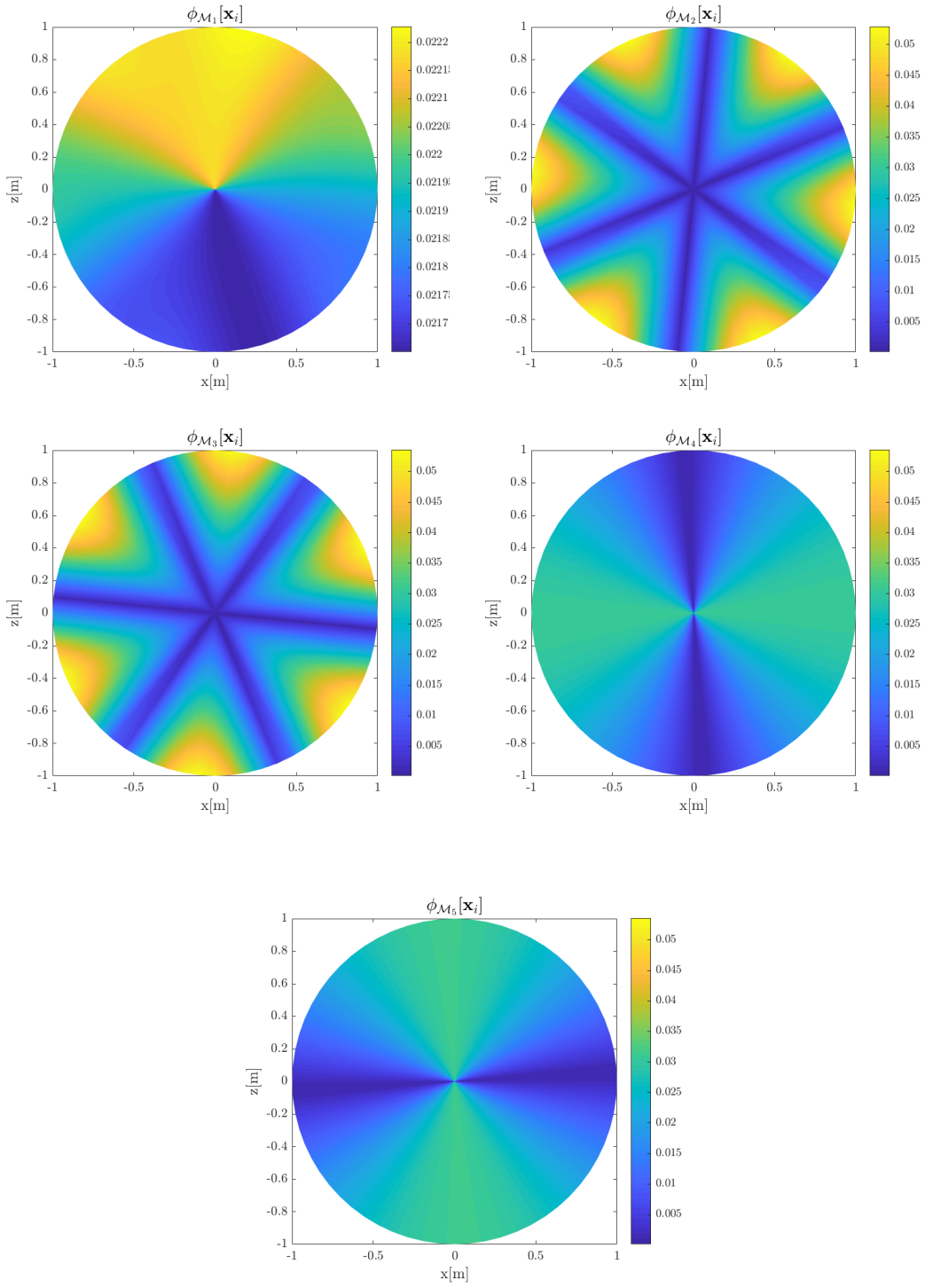

Figure 3.23: Spatial structures of the mPOD decomposition

The Figure 3.23 shows the spatial basis of each one of the modes. The pairing between modes commented previously can be observed in these graphics since they are identical but with an spatial delay of $\pi/2$. As it has been commented before, this phenomena is related to those modes that represent traveling structures.

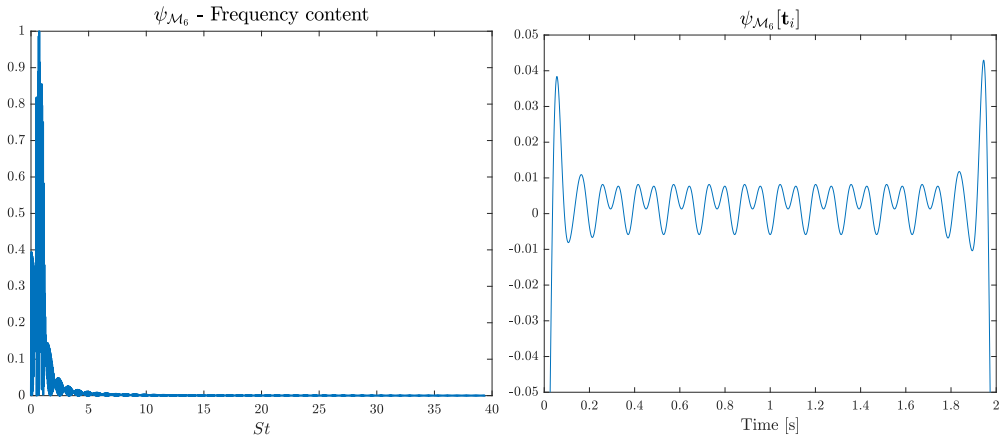

Figure 3.24: Temporal structures of the sixth mPOD mode

The Figure 3.24 shows the temporal basis of the sixth mode computed to demonstrate that the *irrelevant* modes have a non-harmonic behaviour. Since these modes are, from an energetic point of view unnecessary, their behaviour do not affect to the decomposition.

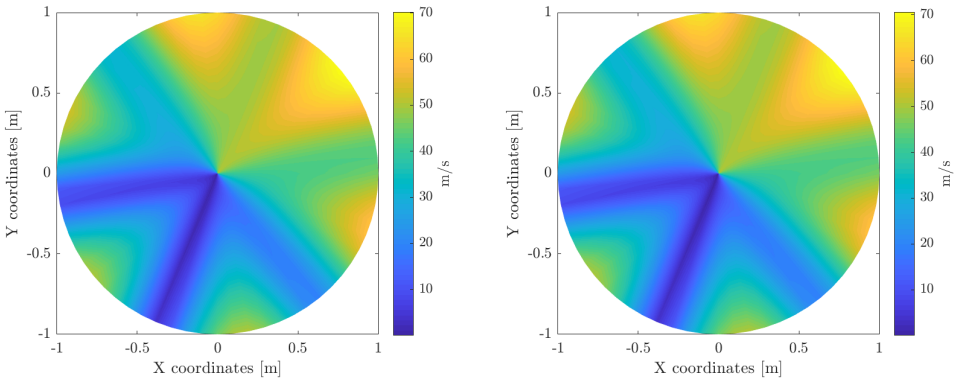

Figure 3.25: Original versus approximated flow field

Considering the first five modes, the reconstruction of the flow field is very accurate to the original one. This is demonstrated in the Figure 3.25 for a certain time step of the simulation. For this case and thanks to its simplicity, POD demonstrated being capable to differenciate properly the modes in §3.1.2 in spite of the velocity field had two different scales as it can be seen in the Figure 3.20 but with different energy content.

3.2.2 Noisy case

The next case to be solved is a modification of the previous one. The velocity field has been redefined adding a Gaussian noise with standard deviation of $\sigma = 80$, in the same way as it was done in the POD analogous case. Alike every previous case, the first step consists on analysing the energy content of the modes. Considering the same criteria than before, it has been selected the first five modes since they contain most of the total energy of the system as it is showed in the Figure 3.26.

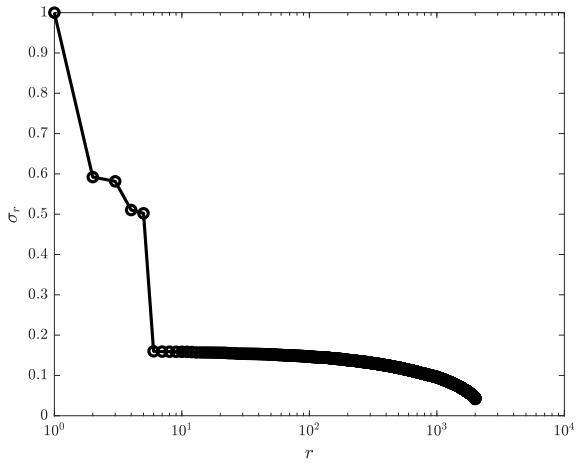

Figure 3.26: Energy content of the mPOD modes

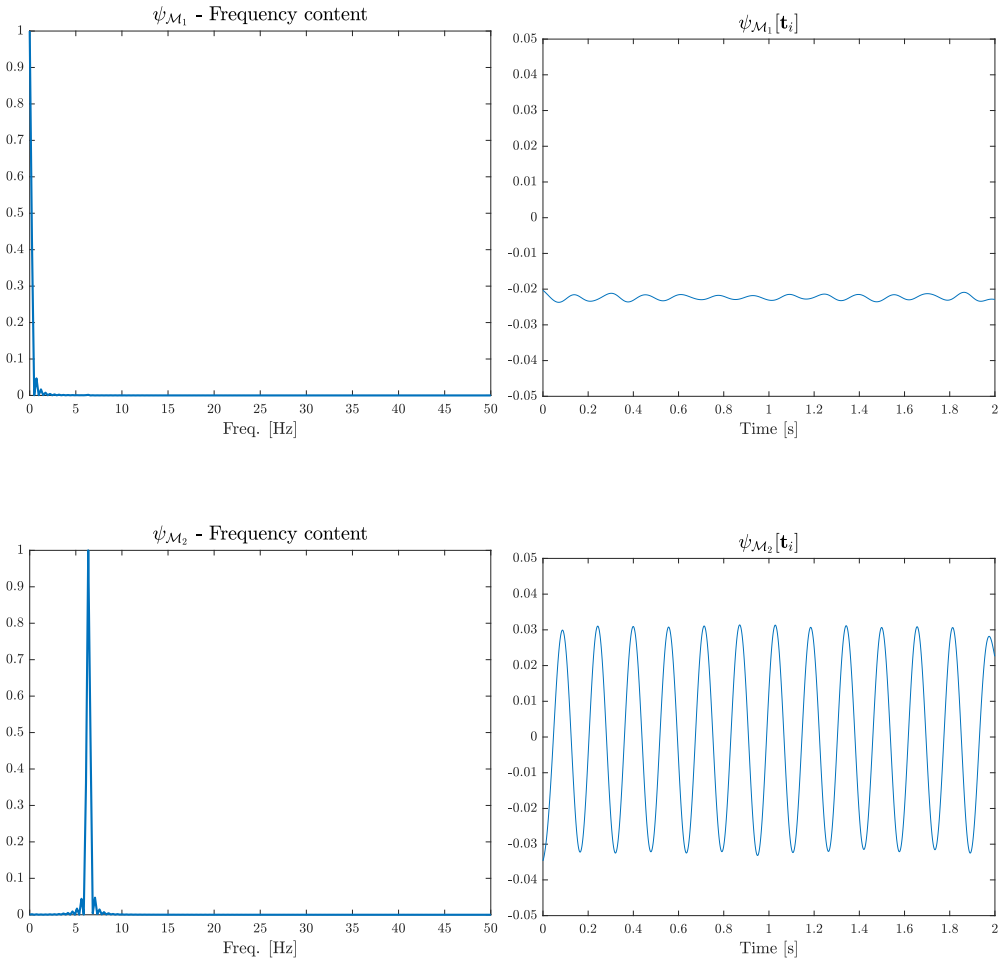

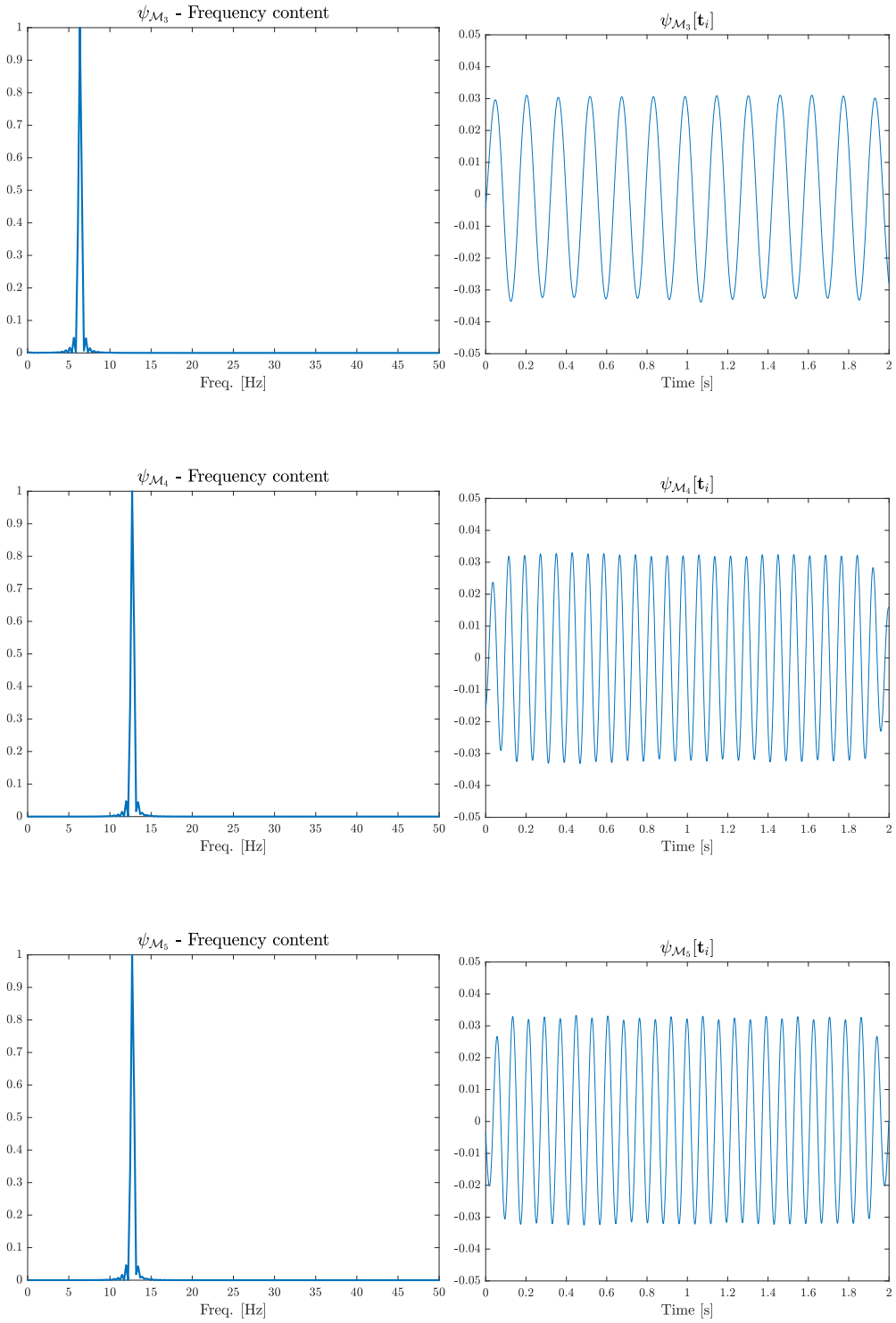

Figure 3.27: Temporal structures of the mPOD modes

In the Figure 3.27 are showed the temporal basis of the mPOD modes computed. As can be observed, the frequency content of the modes is the same that the showed in the Figure 3.11 that correspond to the POD modes of the analogous case. This means that the mPOD modes and the corresponding POD modes are represented by the same harmonics. Besides, the second and third mode are paired, as well as the fourth and fifth mode as it was commented previously. The reason of the pairing has already been commented in previous cases.

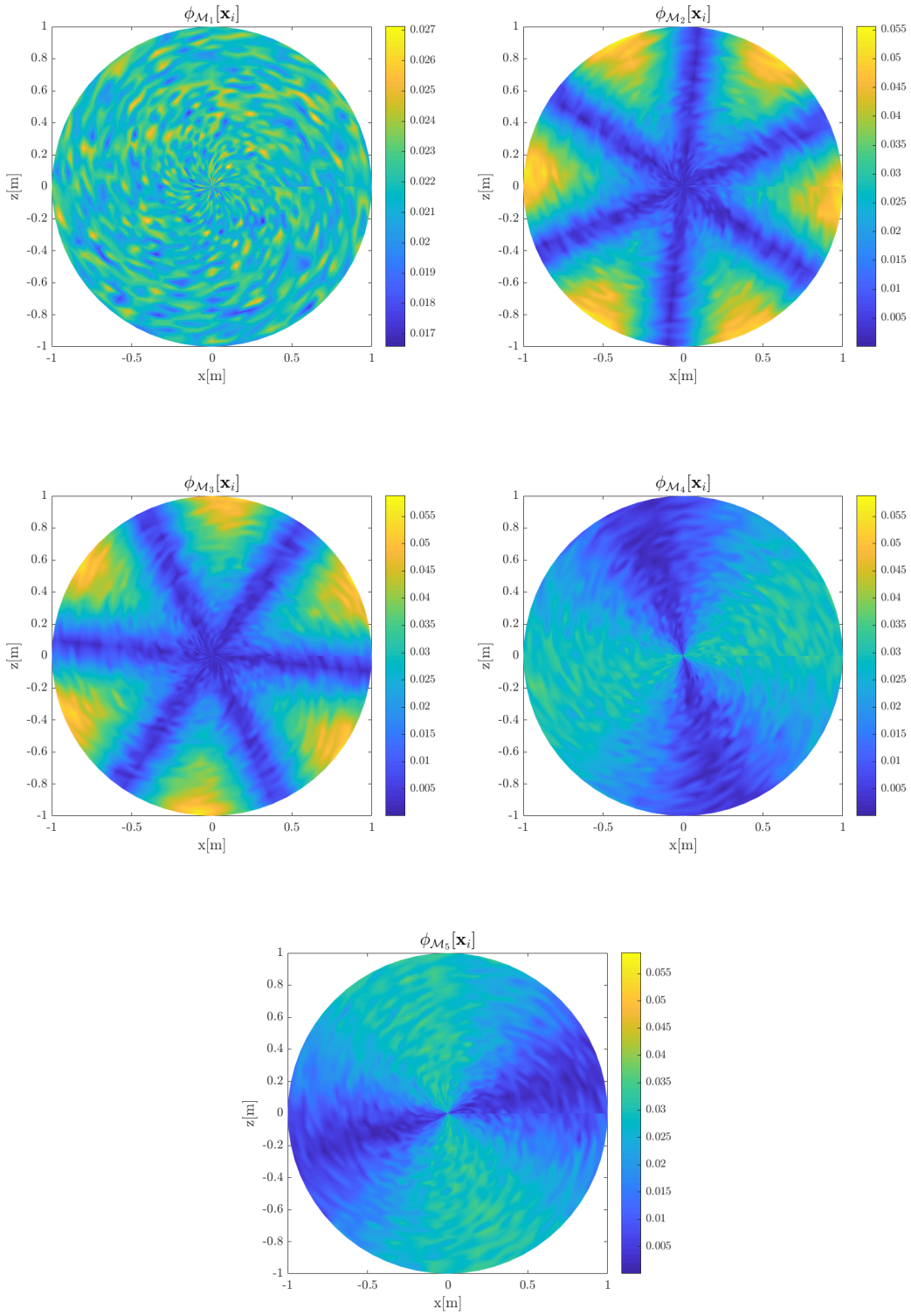

Figure 3.28: Spatial structures of the mPOD decomposition

The main difference between the POD results and the mPOD results is that in the last case, mPOD modes are much cleaner and do not show the noisy behaviour. This can be appreciated in the graphics on the right for all the modes in comparison with the modes obtained from POD. These results bring to light that the mPOD technique improves the POD when the signal or variable to post-process is noisy.

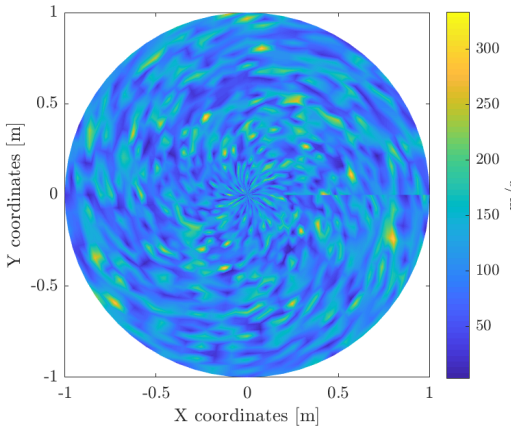

(a) Original flow field

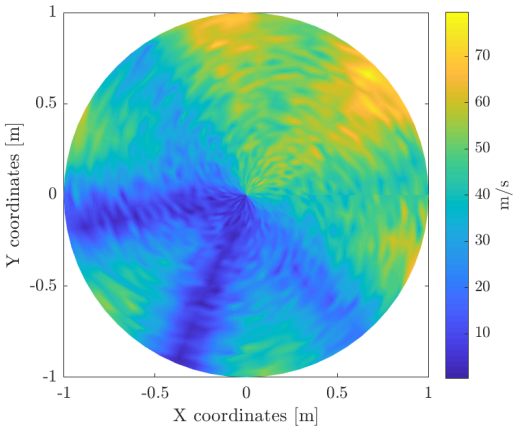

(b) Approximated flow field $N_m = 6$

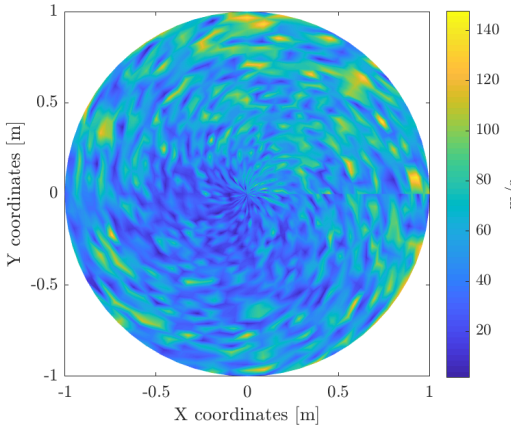

(c) Approximated flow field $N_m = 50$

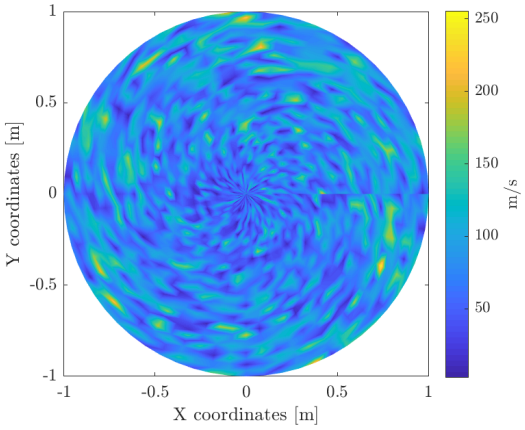

(d) Approximated flow field $N_m = 500$

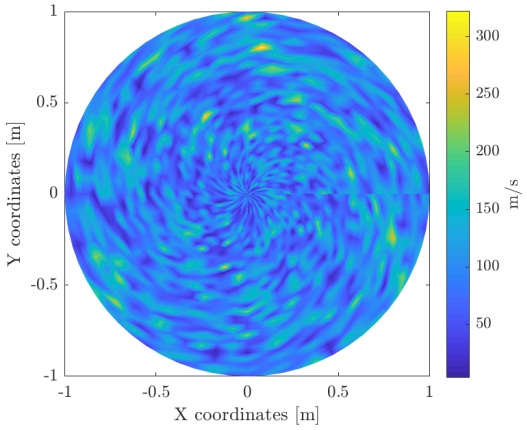

(e) Approximated flow field $N_m = 1000$

Figure 3.29: Different reconstructions of the flow field

The Figure 3.29 shows the reconstruction of the flow field from the mPOD computed modes. As it can be observed, with six modes the reconstruction is far away of the original flow field. This is caused because the mPOD modes not considered for the decomposition given that they do not have a representative energy content have a important role in small regions of the domain to achieve an accurate reconstruction.

In any experimental case, the signal acquired with any kind of sensor are most of the times a noisy signal due to the nature of the flow and the unsteady phenomena, even more when the experiment is conducted into a turbomachinery stage. With the previous results, it can be come to the conclusion that mPOD is better than the POD to post-process noisy signals and therefore to apply to experimental cases as the ones conducted for this project.

3.2.3 Same energy case

In the same way as it was done with the POD synthetic cases, the next one has been developed to test the capabilities of the mPOD of distinguishing between different scales with similar energy content.

The first step consists on analysing the spectra correlation matrix $\hat{K}$ to be able to define the frequency splitting vector. The Figure 3.30 shows the spectra of the correlation matrix on the left, and an enlarged region of it to appreciate better the details. In these graphics can be appreciated that there are some peaks that correspond with the dominant frequencies located at $f \simeq (1,\, 8,\, 50,\, 65)\, Hz$. Taking into account these results, the frequency splitting vector would be $f_v = (5,\, 10,\, 58)\, Hz$ in order to aisle the different scales.

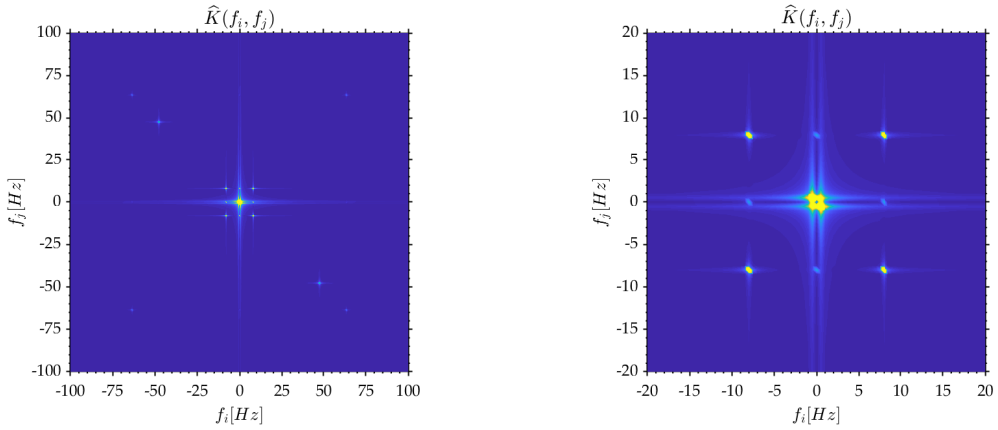

Figure 3.30: Spectra correlation matrix and a detail region

With the frequencies for the filter bank defined before, the transfer functions of the two-dimensional filters look like the ones showed in the Figure 3.31.

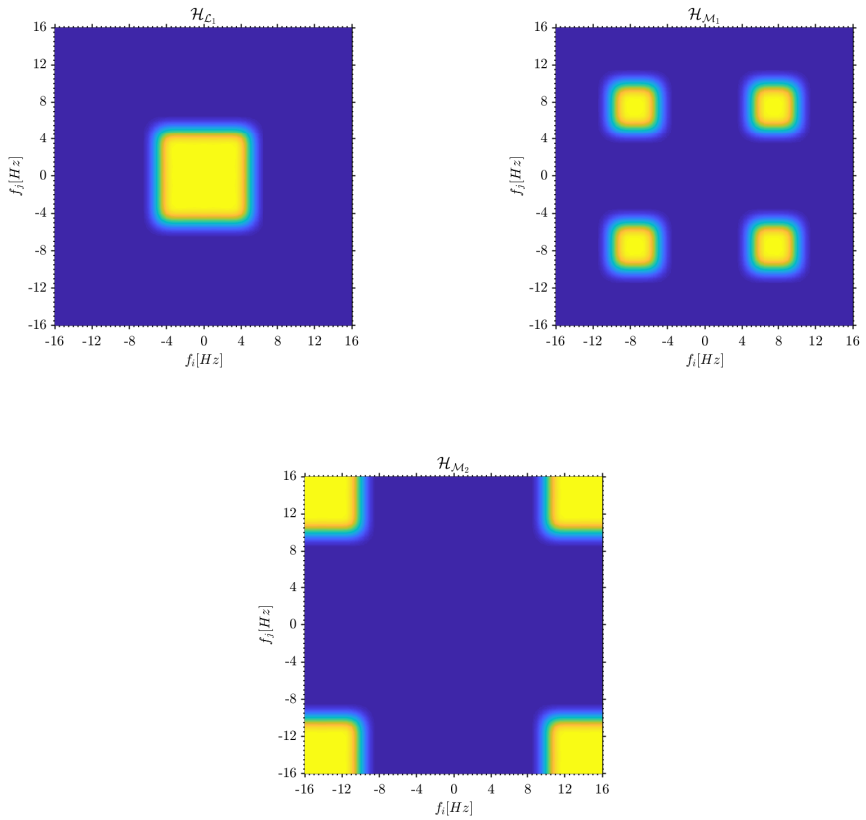

Figure 3.31: Two-dimensional filters

The analysis of the energy evolution of the mPOD modes allows to define the number of them to be computed. The Figure 3.32 shows that the first thirteenth modes contain around the 95% of the total energy.

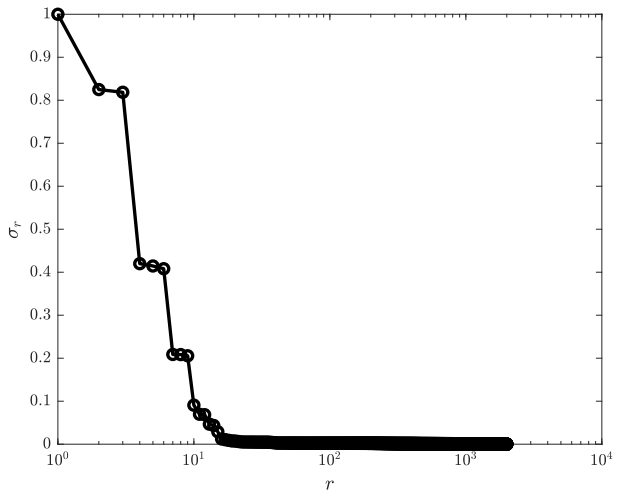

Figure 3.32: Energy evolution

In the graphics below, the temporal basis of the mPOD computed modes are showed. There are some interesting points to comment, however not all the graphics are showed to avoid an excess of results.

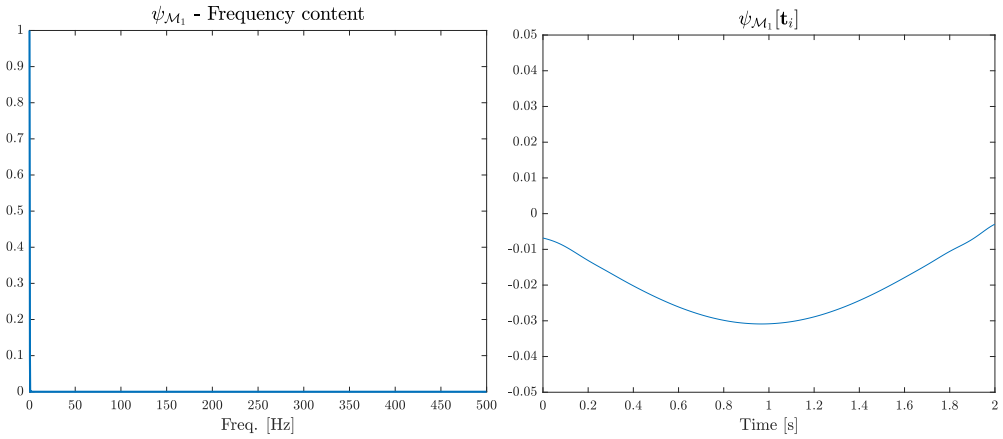
$\psi_{\mathcal{M}_1}$ - Frequency content
Freq. [Hz]
$\psi_{\mathcal{M}_1}[\mathbf{t}_i]$
Time [s]

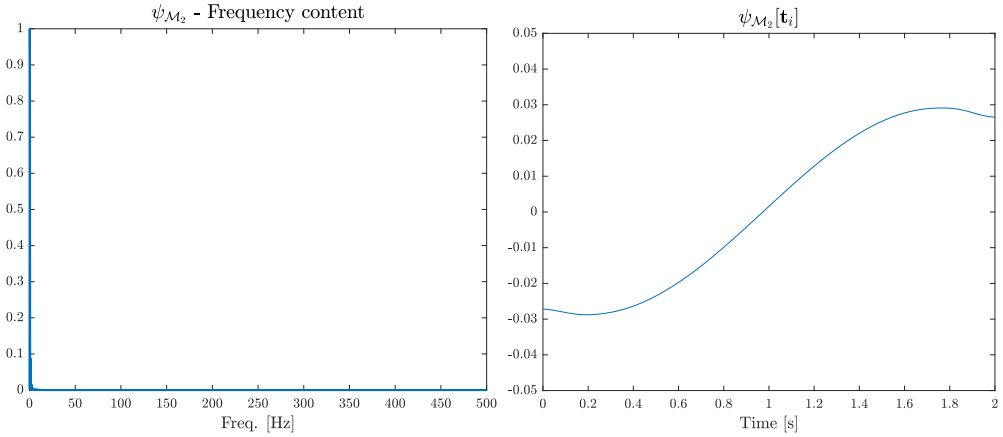
$\psi_{\mathcal{M}_2}$ - Frequency content
Freq. [Hz]
$\psi_{\mathcal{M}_2}[\mathbf{t}_i]$
Time [s]

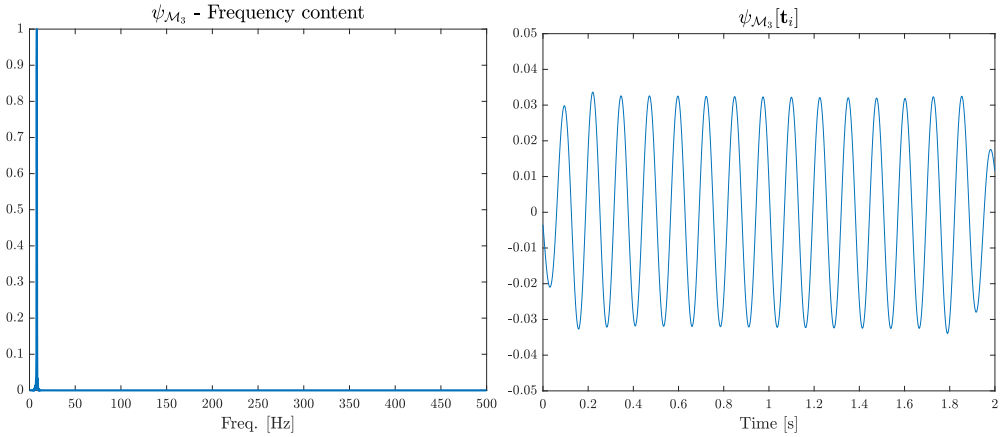
$\psi_{\mathcal{M}_3}$ - Frequency content
Freq. [Hz]
$\psi_{\mathcal{M}_3}[\mathbf{t}_i]$
Time [s]

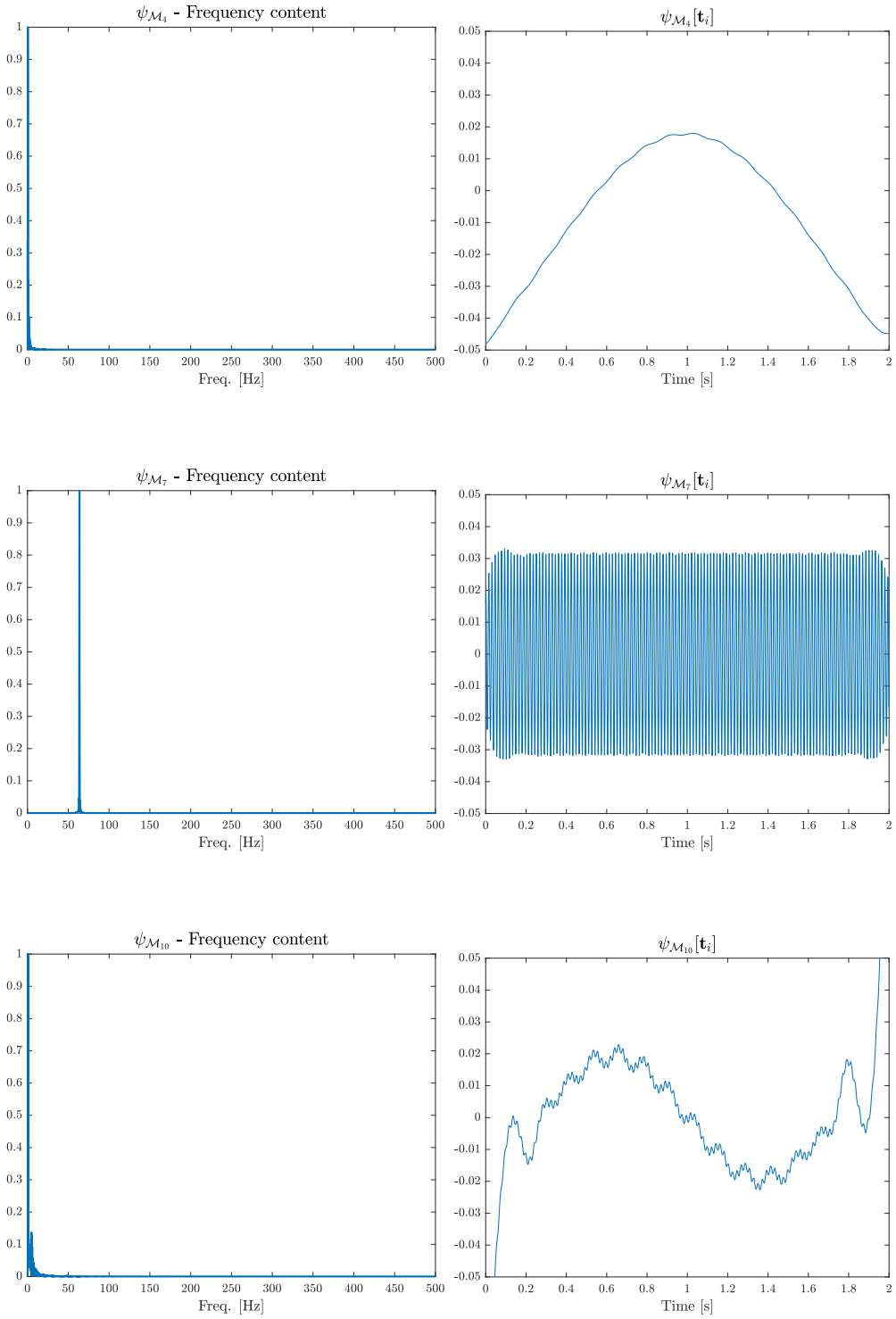

Figure 3.33: Temporal basis mPOD modes

As it can be appreciated in the Figure 3.33 the first, second and fourth mode correspond to very large scales or very low frequencies. Their frequency content is centered in the zero frequency, besides the time series plots show a very slow temporal evolution.

On the other hand, the rest of modes show a high frequency response. In spite of some of the modes have been purposely hidden, it is necessary to comment that the eighth and ninth

mode are paired with a phase delay, as well as the eleventh and twelfth modes. With the exception of the tenth mode, the rest of the mPOD computed modes show a purely harmonic behaviour without spectral mixing. The tenth mode has a really strong frequency content centered around $f = 0\,Hz$. Therefore, it can be said that this mode corresponds to a low frequency response and the very small oscillations can be dismissed.

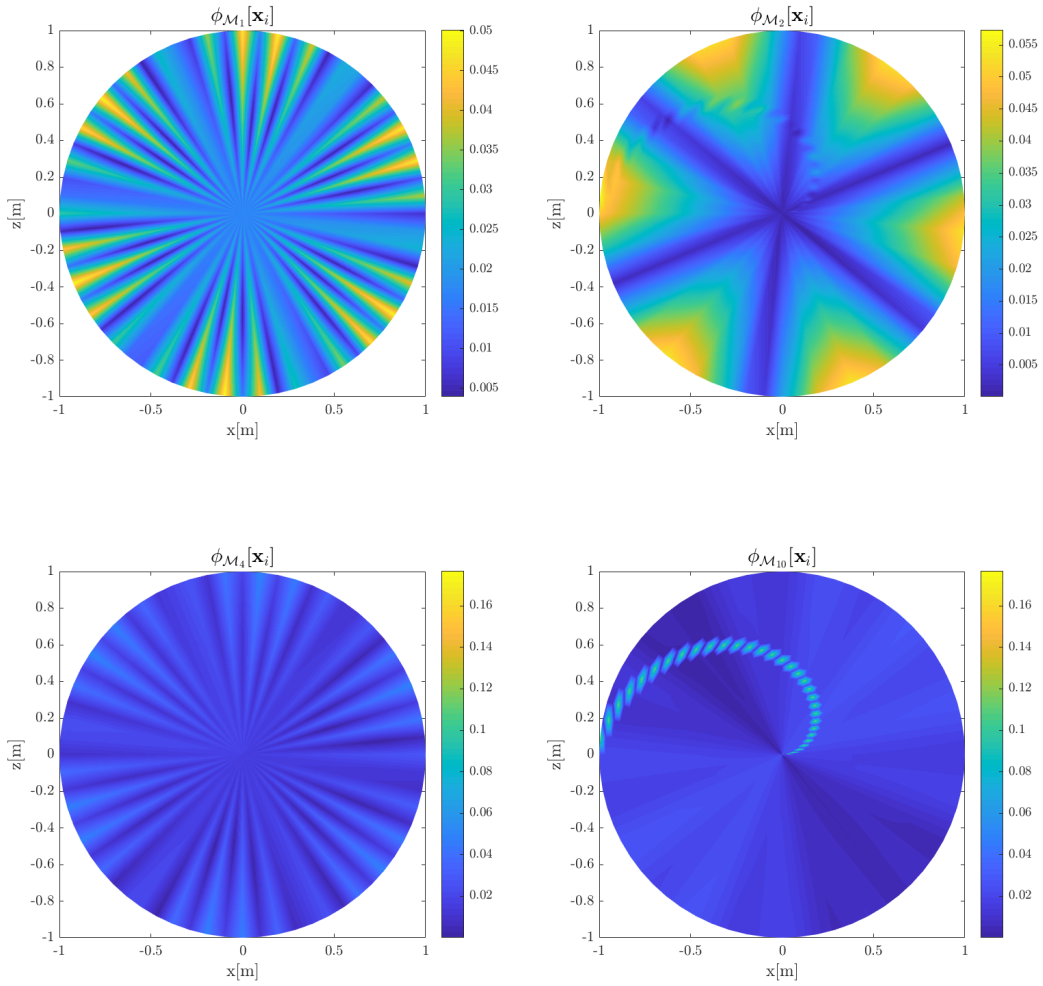

Figure 3.34: Spatial structures

The Figure 3.34 shows the spatial structures of some of the mPOD computed modes. These are the same modes than the ones shown in the Figure 3.17 with the purpose of making a comparison between them. The spatial structures of the POD modes show a mixing between different phenomena that in the mPOD modes does not appear. The most significant difference it can be observed in the first mode both in the spatial and temporal structures: the POD mode $\phi_{\mathcal{P}_1}$ show two different phenomena whereas the mPOD mode $\phi_{\mathcal{M}_1}$ the low frequency phenomenon has been isolated. The rest of the mPOD modes are apparently similar to the equivalent POD's but just with one of the phenomena. The tenth mode barely shows a bit of spectral mixing, but it is clear that one of the phenomena is much stronger.

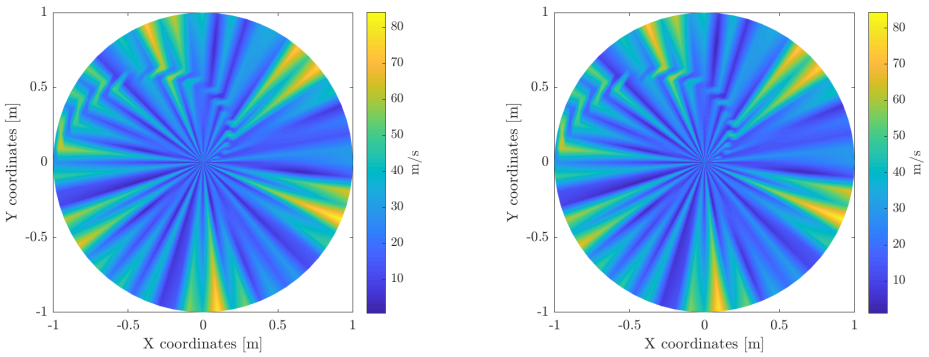

Figure 3.35: Original and reconstructed flow field

With all these modes, the recontruction of the flow field is quite precise and the accuracy obtained is high. This can be observed in the Figure 3.35.

With the results showed above and the corresponding comments, it has been demonstrated that mPOD is considerably better than POD in such cases like this one. Taking into account the purpose of the project and the nature of the flows inside the turbomachines, it is obvious that mPOD has to be considered as first option to post-process the raw signals obtained in experimental measurements.

3.3 Experimental case: PIV of an impinging jet

In order to giving a different point of sight for the application of POD and mPOD a different experimental case is presented. In this case, both techniques are applied over the experimental results obtained from the Particle Image Velocimetry (PIV) of an impinging jet flow onto a flat surface. This flow is considered to be statiscally stationary. It should be commented that this case correspond with one of the cases proposed by Mendez M. in his project [15].

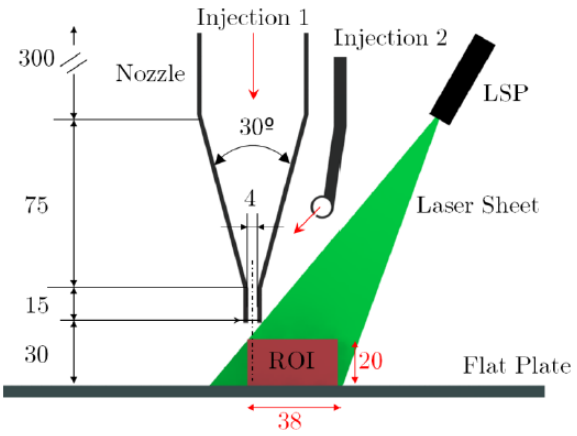

Figure 3.36: Experimental set-up

The Figure 3.36 shows the experimental dataset where it can be appreciated the location of the injector and the domain studied, also called Region of Interest (ROI). The purpose of

this section is showing the results of the POD and mPOD and the differences in the solutions. Therefore, explaining the experimental development is not the purpose and the reader is invited to read the original report for this.

However, it is necessary to give some data of the experimental domain as well as some specific data needed to the later analysis. The outlet nozzle of the injector has a diameter of $H = 4\,mm$ and it is located at $10\,mm$ of the ROI. In this case, the results corresponding with the temporal structures are given in terms of the Strouhal number $St = f_s H/U_0$. As it has been done in the previous cases, the results obtained with the POD are firstly showed and then the ones obtained with mPOD. The convenient comparisons will be done at the end of the mPOD section.

It should be commmented that in this case the experimental domain is a cartesian grid and the averaging process used in all the previous cases is not needed. Since in this case, the velocity field is the variable of interest and it is composed by both components, the data has to be arranged in a similar way as it was done in any of the synthetic cases.

In this case, the solutions of both techniques are presented together since it is easier to make the different comments. First of all, the mandatory step before selecting the number of modes to compute is checking their energy content. The Figure 3.37 shows the evolution of the energy in both cases of each mode normalized with the maximum energy.

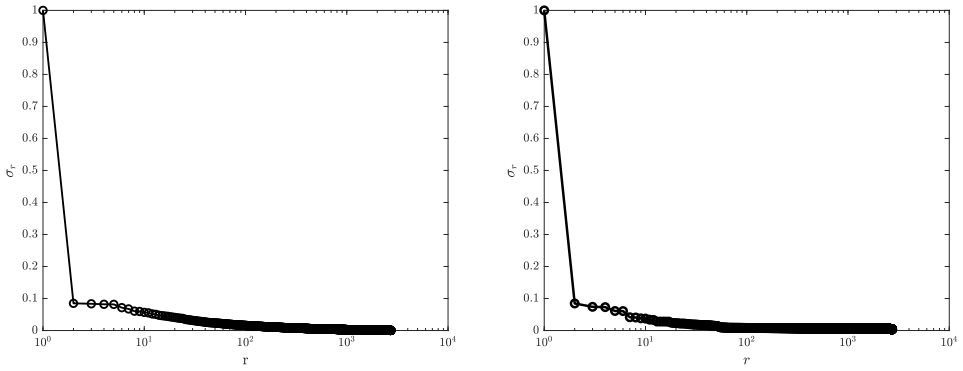

(a) POD modes energy (b) mPOD modes energy

Figure 3.37: Evolution of the energy

In both cases, the modes show a quite similar energy evolution and ten modes are computed since it can be achieved around the 95 % of the total energy. The first results presented below are corresponding to the POD results.

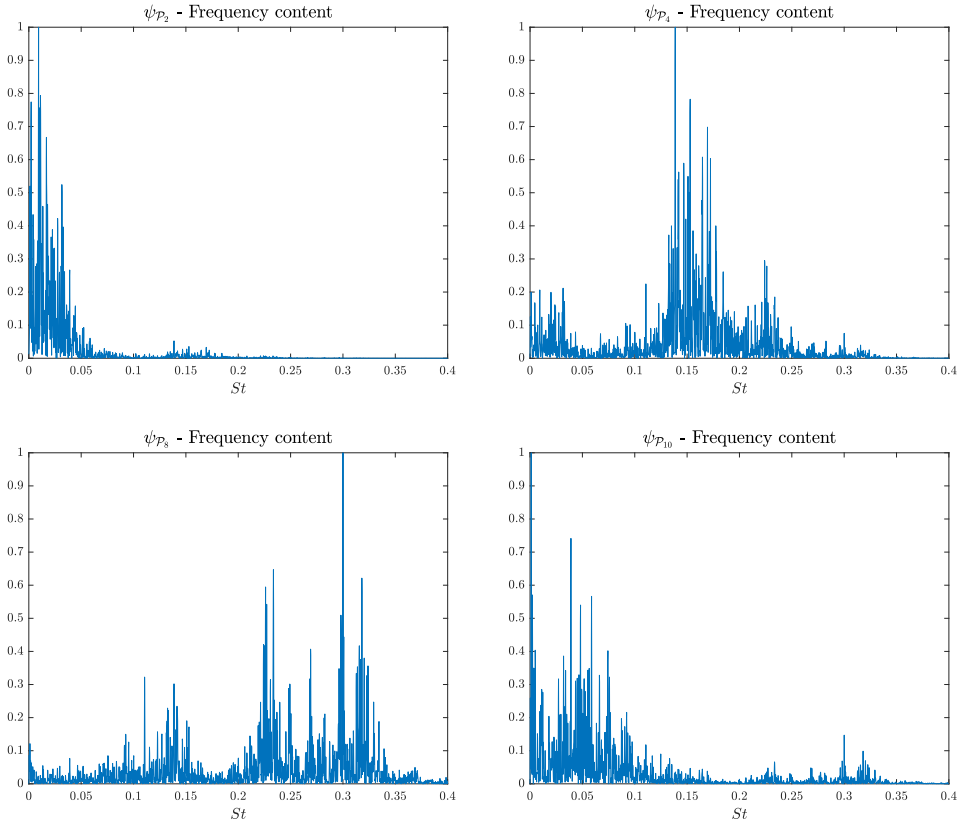

Figure 3.38: Temporal structures of significant POD modes

The Figure 3.38 shows the temporal basis of some of the POD modes computed. These modes are the most significant and the comments given about them can be extended to the rest. The temporal structures are plotted in terms of the *Strouhal* number, and therefore in terms of the frequency content instead of the temporal evolution. Taking into account that the original flow field is known and it can be visualized, is more interesting analyse the results in this way.

As it can be observed in all of the modes presented above, the spectral mixing appears in the frequency analysis. In the mode $\psi_{\mathcal{P}_2}$ the spectra mixing is not so evident as in the case of the mode $\psi_{\mathcal{P}_4}$ or $\psi_{\mathcal{P}_8}$. In any case, this results prove that POD applied over a stationary case composed by different scales with similar energy content generates modes with spectral mixing.

Concerning to the spatial structures, it has been showed the same modes as before. It can be distinguished two different regions in the spatial domain, a free-jet region close to the left boundary and a wall-jet region in the lower right area. In the Figure 3.39, it can be appreciated some interesting coherent structures that the POD modes are capable to detect. The second mode $\phi_{\mathcal{P}_2}$ is more related to the wall-jet region where the significant spectra is located at low-frequencies as $\psi_{\mathcal{P}_2}$ shows.

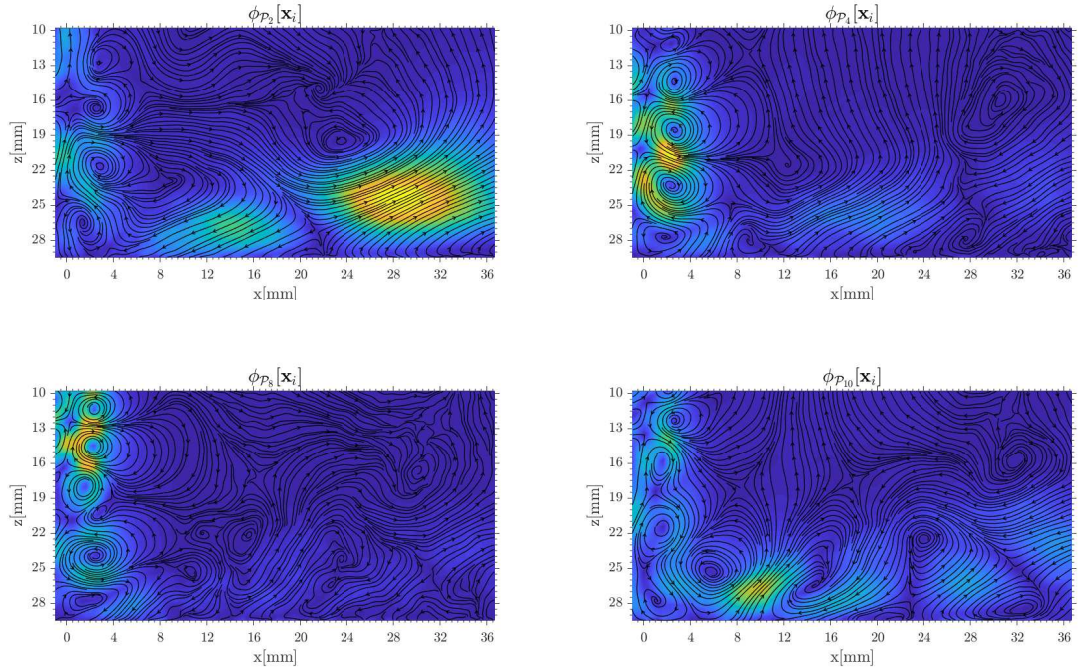

Figure 3.39: Spacial structures of significant POD modes

On the contrary, the mode $\phi_{\mathcal{P}_8}$ is more related with the free-jet flow and therefore its spectral content is located around $St \simeq 0.3$ as it has been demonstrated in the literature.

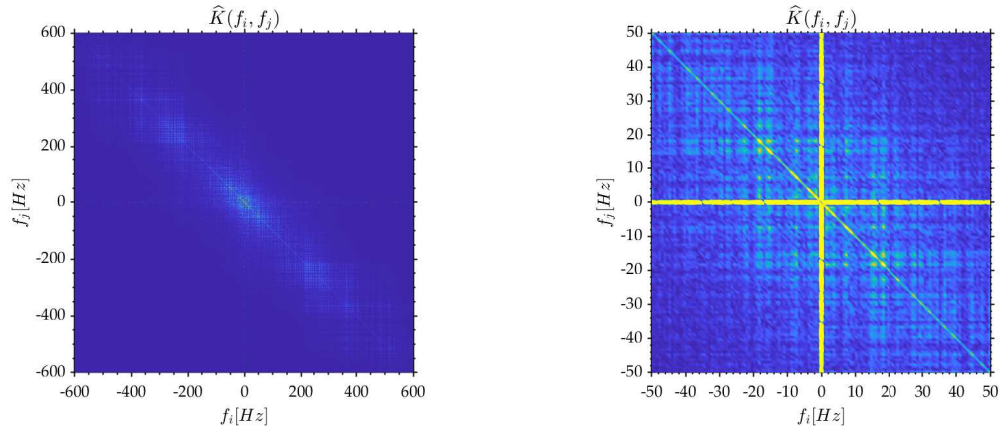

Figure 3.40: Spectra correlation matrix

Before computing the mPOD, it is necessary to check the spectra of the correlation matrix $\hat{K}$. The Figure 3.40 shows this spectra and an augmented part of it, where it can be observed that there is a dominant peak at $f = 12\,Hz$. It can also be said that there is a significant content located in the range $f \simeq 150 - 350\,Hz$. Taking this into account the filter bank is defined as $F_v = [160,\, 350,\, 815]\,Hz$.

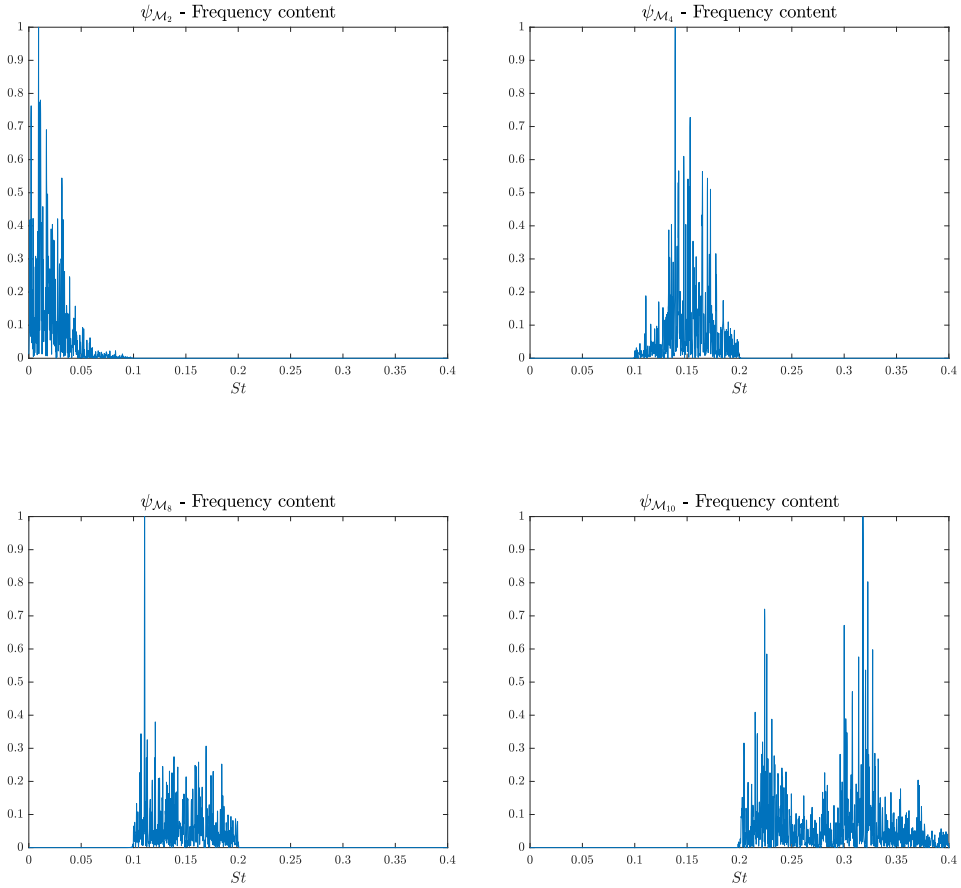

Figure 3.41: Temporal structures of significant mPOD modes

The Figure 3.41 shows the temporal structures of some of the computed modes in terms of the *Strouhal* number. In the different graphics can be observed the absence of spectral mixing. As the second and fourth mode have the same frequency content in both methods, the comparison in the spectra clearly demonstrates this. In the case of the eighth and tenth mode, the spectra is different in both methods so the comparison is not so clear.

According to the results obtained for the spatial structures, the second mode is highly related to the wall-jet region and thus the low-frequency content is dominant. The tenth mode is clerly related to the free-jet region and the dominant frequency is around $St \simeq 0.3$ as well as it happened with the POD modes. The fourth and the eighth mode are related with the region where the stagnation of the jet occurs and therefore the frequency content is similar.

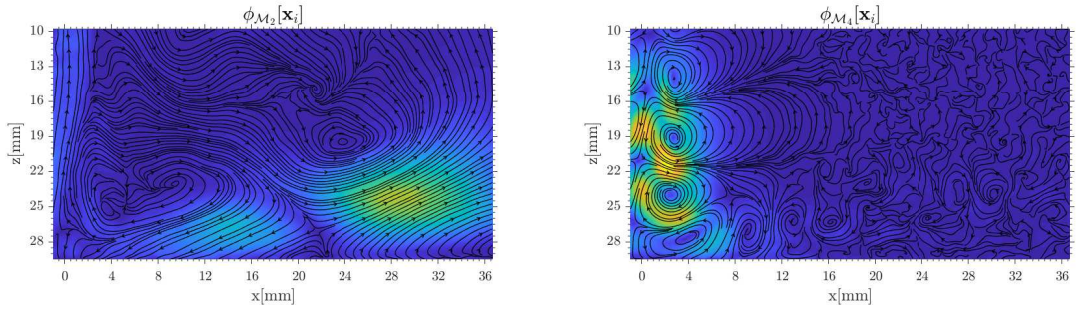

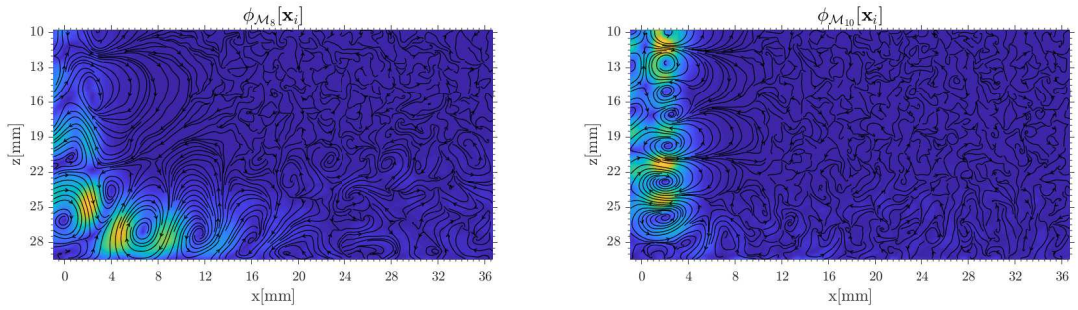

Figure 3.42: Spatial structures of significant mPOD modes

The main difference between the results showed above is that the POD is not capable of distinguish between different scales with similar energy content and therefore the spectral mixing appears. Concerning to the mPOD results, the number of scales in which split the spectra could be raised and this would lead to an improvement in the frequency resolution. As it has been commented several times before, one of the advantages of the mPOD is that it can be moved towards the DFT decomposition increasing the number of frequency bandwidths.

3.4 Experimental case: pressure field in an axial turbine

The present section shows the results obtained after applying the mPOD over real data of an axial turbomachine. The state-of-art aircraft engines usually operates at high temperatures and lean conditions in order to meet the emissions targets. The experiments were conducted as part of the European Comission FP7 project FACTOR (Full Aerothermal Combustor-Turbine interactiOns Research). The aim of this project was studying the aerodynamic and thermal features of the interaction between the combustor and the high-pressure turbine with the purpose of improving the integration between these two elements and the performance of the core engine. This project was developed by a consortium of European institutions and companies giving as a result a large quantity of interesting results.

The experiments were conducted in the turbine test rig facilities of the German Aerospace Center (DLR) in Göttingen, Germany. The different parts of the experimental set-up were constructed by the different partners of the consortium as well as the experimental probes. The Von Karman Intitute for Fluid Dynamics provided the fast-response aerodynamic probes to measure the pressure fluctuations, as well as the instrumentation of the rotating system. The data-driven decompositions commented in previous sections are going to be applied over the pressure field of the turbine and therefore some little changes in the code have to be done. In the synthetic cases as well as in the PIV case, the velocity field was composed by two components but the pressure is an scalar field so this is one of the main changes. The geometry of the experiments is largely different than the domain used in the synthetic cases but this will be commented with more details in the following sections.

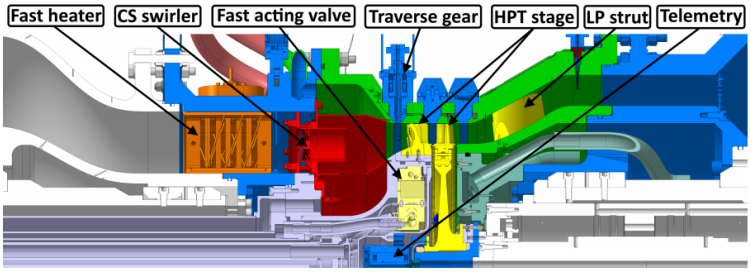

Figure 3.43: Cut-away view of the test section [8]

In the Figure 3.43, it can be seen a cut-away view of the test section. Different colors are used to distinguish different parts and also the company or institution responsible of its design.

Since the project is not only focused in the aerodynamic features but also on the thermal conditions of the combustor-turbine interaction, similar conditions of the actual flow during the performance of the engine have to be achieved. With this purpose a non-reacting combustor simulator was designed achieving high realistic boundary conditions for the experiments. This device is composed by a fast electrical heater and a swirling device.

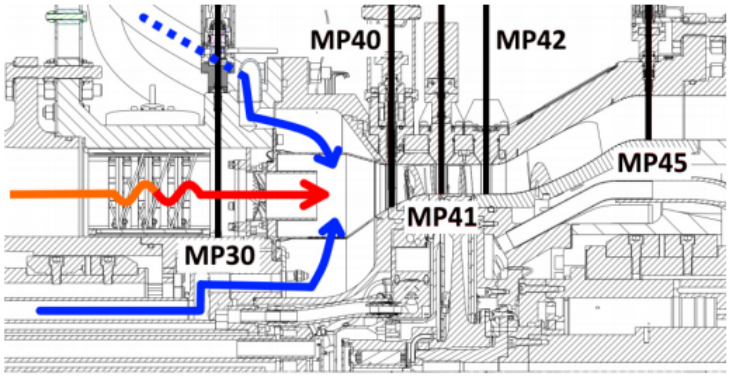

Figure 3.44: Flow distribution and measurement planes [8]

Some of the experiments were conducted with the heater on and some other with the device off. Since the main interest of this project is focused on the pressure field, the operation of the heater only had influence over the probes calibration.

In the Figure 3.44, it can be observed the combustor simulator location and the flow distribution. A cooling flow is injected downstream of the swirling device in order to simulate the real conditions. In this figure, it is also presented different measuring planes where data was acquired.

3.4.1 Measuring method

Once the experimental facility has been explained, the next step is to comment how the experiments were conducted. A single stage of a state-of-the-art turbine was tested and the pressure and temperature of the flow field was measured on several planes shown in the Figure 3.44. The different measuring planes were strategically placed to measure those variables and study the flow interaction in the interface combustor-turbine and its influence over the performance of the core engine. In this project, the data used corresponds to the pressure field in the plane $MP40$, and therefore just downstream of the combustor.

The rotor and stator stages have a total of 60 blades and the vanes have a constant height equal to $45\,mm$ from inlet to outlet while the pitch length is equal to $22.5\,mm$. The hub radius is equal to $223.463\,mm$ and the shroud radius $280\,mm$. All these parameters of the geometry will be used later to create the matrix areas to properly balance the inner products of the mPOD, in the same way as it was done in all the synthetic cases. All these data is presented in the Table 3.5.

R_{Hub}	$223.463\,mm$
R_{Shroud}	$280\,mm$
$Span$	$45\,mm$
$Pitch$	$22.5\,mm$
N_{blades}	60

Table 3.5: Turbine geometry

The pressure signal was acquired with a high-response probe with a sampling frequency of $F_s = 500\,kHz$ during two seconds in each position giving a total of one million of temporal samples. The pressure sensor gives as output a voltage signal and this has to be converted by means of a calibrating process to actual pressure values. This calibrating process is described by the expression 3.9 where V_p and V_s are the voltage signals and $P_{cal,i}$ are a series of calibration parameters that depend on the inlet conditions.

$$P = P_{cal,1} + P_{cal,2}V_p + P_{cal,3}V_s + P_{cal,4}V_pV_s + P_{cal,5}V_s^2 \tag{3.9}$$

The measurements were taken moving the probe point by point describing a spatial grid. The sensor was moved along the span, starting at a certain pitch position from the hub to the shroud. Then the sensor is placed in the next pitch position and moved from the shroud to the hub in the way back. This procedure was done along 41 span points and 42 pitch positions describing a *zigzag*. In total, the pressure was measured in 1722 points. Each time the probe was placed in a certain position it was necessary to wait until the flow field was stabilized before starting to take measurements. Due to the probe's dimensions, in the hub region was necessary to keep $2.5\,mm$ of distance. This cut off an interesting region of the domain from the point of view of results.

In the Figure 3.45, a sketch of the spatial grid described by the pressure probe is showed. It can be observed the direction followed by the probe marked with arrows along the span directions. Also, the measurement grid was undersampled to make easier the understanding of the procedure.

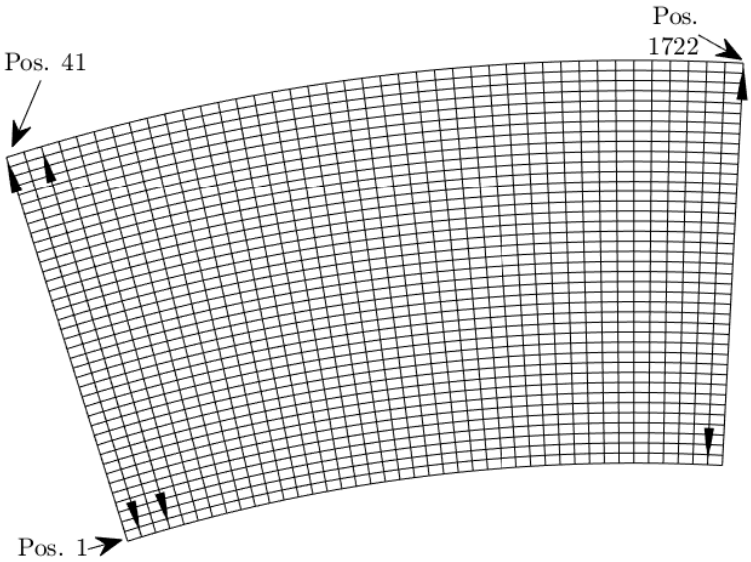

Figure 3.45: Spatial grid described by the probe

Apart from the measures of the pressure and temperature, a measure of the rotational speed of the rotor stage was also taken. This speed was measured by means of a sensor placed in one of the blades of the rotor stage and other sensor in a fixed blade of the stator. Each time both blades were aligned, the sensor goes to a high value and therefore, the signal indicates each time a whole revolution is given by the rotor. The Figure 3.46 shows the $1/rev$ signal.

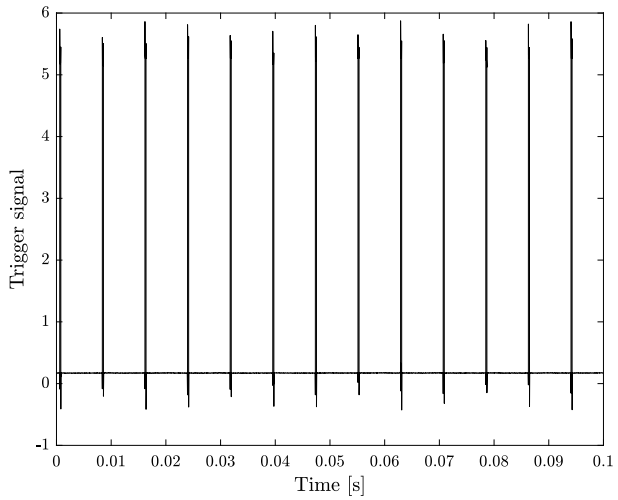

Figure 3.46: 1/rev signal

Analysing the previous graph, the BPF (Blade Passage Frequency) can be obtained. In MATLAB, an algorithm has been coded to detect when the $1/rev$ signal is on high value defining a trigger level. The code detects in which time this blade passage occurs and also it computes the time difference between two consecutive blade passages. This time difference is the time the rotor needs to give a revolution and therefore is an indicator of the rotational speed and the BPF.

$$\Delta t = 0.0078\,s \rightarrow BPF \simeq 128.34\,Hz \tag{3.10}$$

Given that the sampling frequency of the sensors is very high, they were able to detect any variation of the rotational speed and this is why in the expression 3.10 the symbol $\simeq$ is used even though the variations are less than 1%.

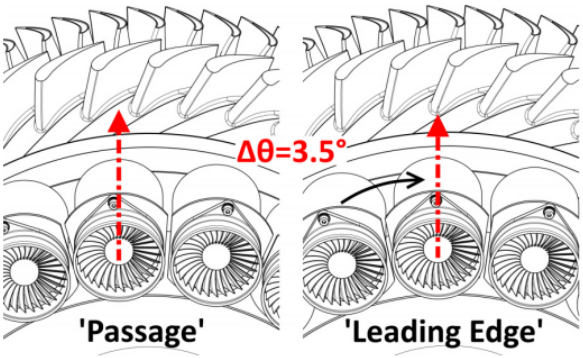

Figure 3.47: Different possitions of the combustor simulator [8]

The combustor simulator was able to slide in the rotational direction allowing different positions of the hot-streak core. During the experiments, two positions of the combustor were used. In the first position called *Passage (Pa)*, the core of the combustor is aligned with the passage between two blades. In the *Leading Edge (LE)* configuration, this core is oriented to the stagnation point of the blade. The Figure 3.47 shows both configurations.

Due to the process followed to take the measurements, the data had to be treated before using it for any purpose. Firstly, each measurement started at a different main blade position instead of starting the acquisition when this blade passes through the $1/rev$ sensor. On the other hand, the measurements were taken point-by-point what means that the raw data is not simultaneous and therefore the unsteady phenomena captured in one point is measured with certain delay in the next position.

The first issue was easily solved since the $1/rev$ signal was available and all the data was selected to start when the main blade is at the same position. This was done with a MATLAB algorithm that detects the peaks in the signal and extracts the pressure data according to the first passage.

To solve the second problem, a rephasing of the data had to be done. This procedure consisted on a FFT of the pressure data. The first measuring position is taken as reference and therefore the phase of the corresponding data is taken also as reference. This phase is imposed over the data on the rest of the positions and then, the IFFT (Inverse Fast Fourier Transform) is computed. The new pressure obtained in this inversion has the same phase in all the locations and therefore all the phenomena is supposed to be phased.

3.4.2 Frequency analysis

The next step consists on conducting an spectra analysis over some orderly distributed positions of the spatial grid. This analysis has been done making use of the standard Fast Fourier Transform (FFT) and the Power Spectral Density (PSD) following the Welbech's method which will be explained afterwards. It should be commented that the signal considered in these analysis only correspond to the oscillations of the pressure field since the mean value has been substracted.

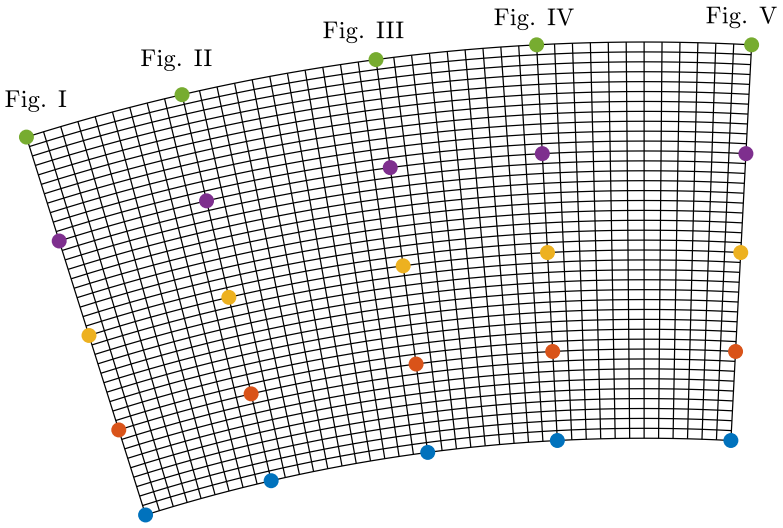

Figure 3.48: Positions where FFT and PSD have been computed

The Figure 3.48 shows the spatial grid of the experimental measures and the positions where both studies have been conducted, the colors used to mark the different points are the same used in the different graphics to differenciate the results of two different positions and make easier the comments.

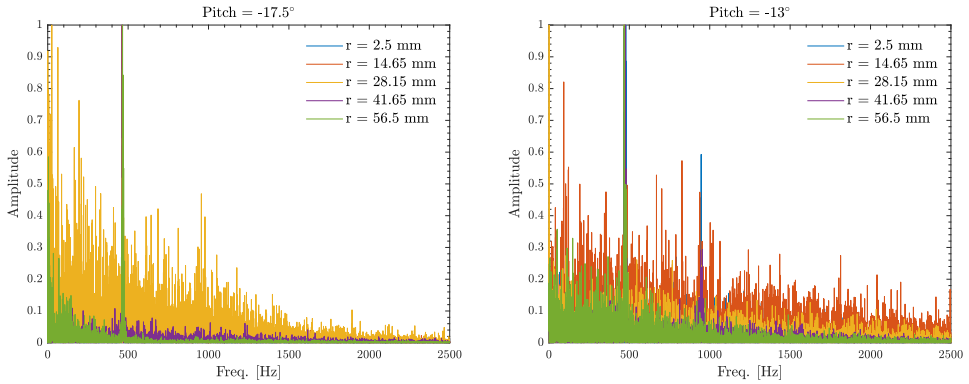

(a) Figure I

(b) Figure II

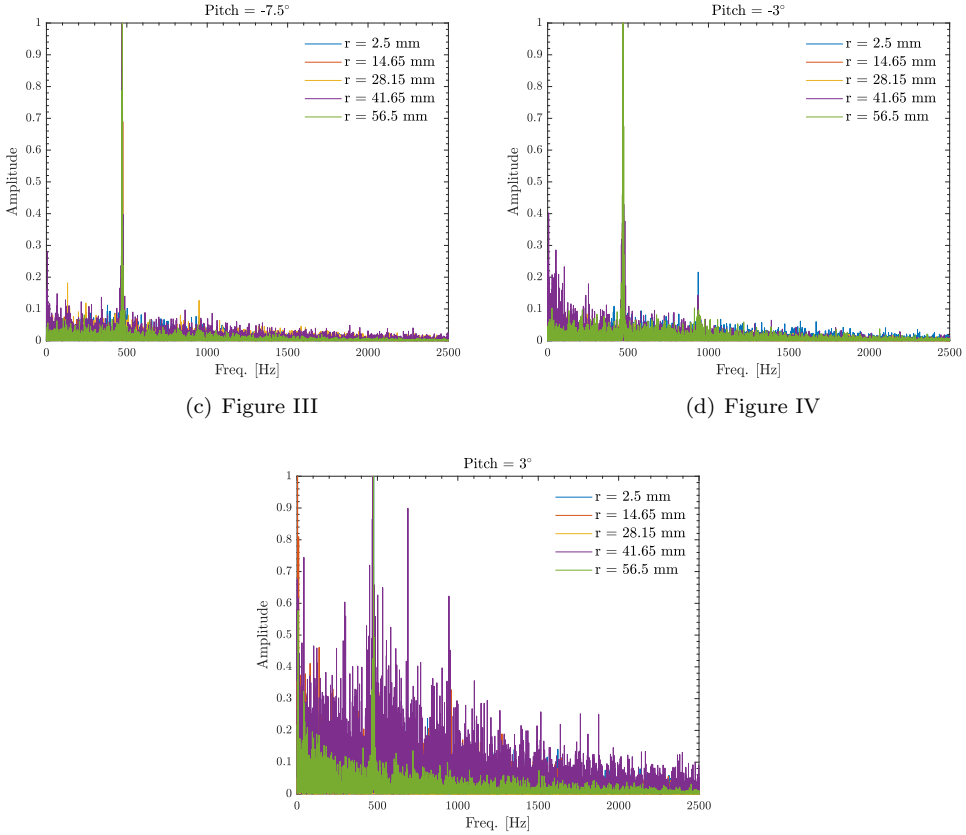

(c) Figure III

(d) Figure IV

(e) Figure V

Figure 3.49: Results of the FFT

Firstly, the results of the analysis done with the FFT are showed in the Figure 3.49. It is necessary to make some commentaries about the representation before starting to analyse the graphics. As it has been commented before, the colors used in these graphics are the same as in the Figure 3.48 to distinguish different radial positions in each plot. The legends of the figures make use of a radial coordinate r that is the distance from the hub of the turbine to the sensor. Therefore, the coordinate $r = 2.5\,mm$ is the closest position to the hub and $r = 56.5\,mm$ the closest one to the shroud.

The results presented show a general trend since all the plots present a dominant frequency placed around $f = 473\,Hz$. Besides, the Figures I, II and V show a high content at low frequencies specially in the middle radial positions. However, the Figures III and IV show a cleaner frequency content in all the radial positions.

To facilitate the understanding of the results and reduce the chaotic spectra that some positions have, it is opted to apply the Welbech's method of Power Spectral Density (PSD) [19]. In general terms, this method splits the signal into segments taking a modified periodogram of each section and the final periodogram is an averaging of these.

Assuming that each segment has a finite length L, an overlapping of D samples can be defined by the user and in this case has been selected to be the 50% of the window length. Before computing the average of the periodograms, each segment is windowed with a Hamming window of the same length L. To obtain the final results showed below, a parametrical study over the window length L has been conducted considering $L = [2000, 10000, 20000, 40000, 80000]$. The

largest L value would give the best spectral resolution but this could lead to a poor identification of the main peaks if the noise level keeps too high. In the end, $L = 80000$ was selected as it provides the highest value of the ratio between the main peak energy and the overall PSD.

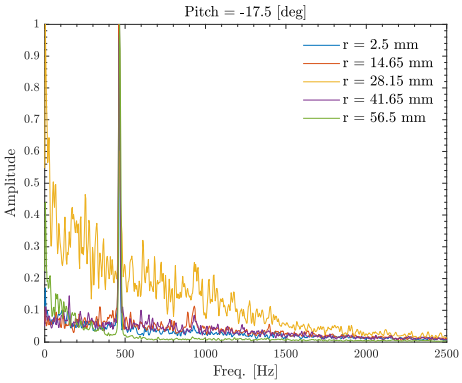

(a) Figure I

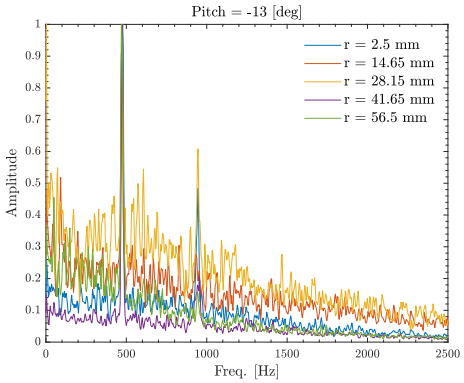

(b) Figure II

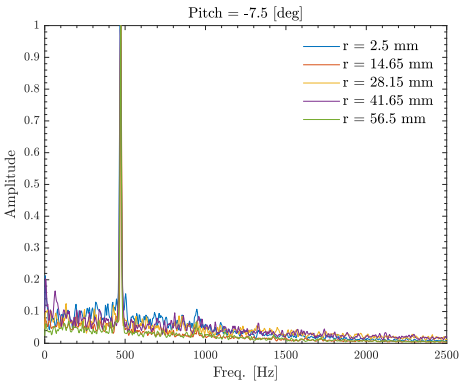

(c) Figure III

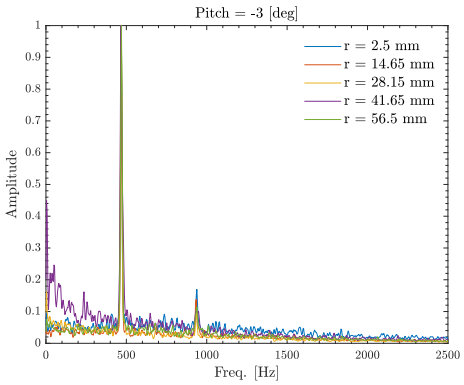

(d) Figure IV

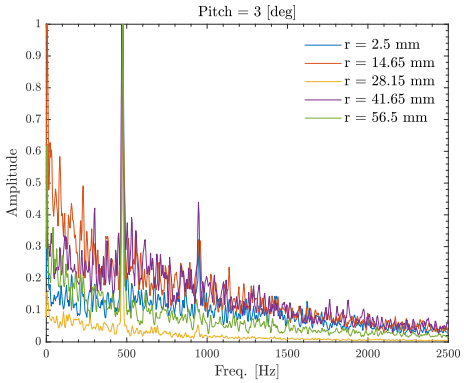

(e) Figure V

Figure 3.50: Results of the PSD

As it can be appreciated, in these new plots the results are less chaotic and its understanding and analysis is easier. A general comment for all the positions analysed is that the main frequency is located at $f = 473\,Hz$ as it had been commented before. In the positions corresponding to the figure II, IV and V a second harmonic at $f = 946\,Hz$ appears with a considerable energy content. Some positions of the figures I, II and V show a low-frequency

content quite important even though the mean pressure has been supressed. This positions are located at the middle span whereas the points closer to the hub and shroud do not present content in the low-frequency or high-frequency range.

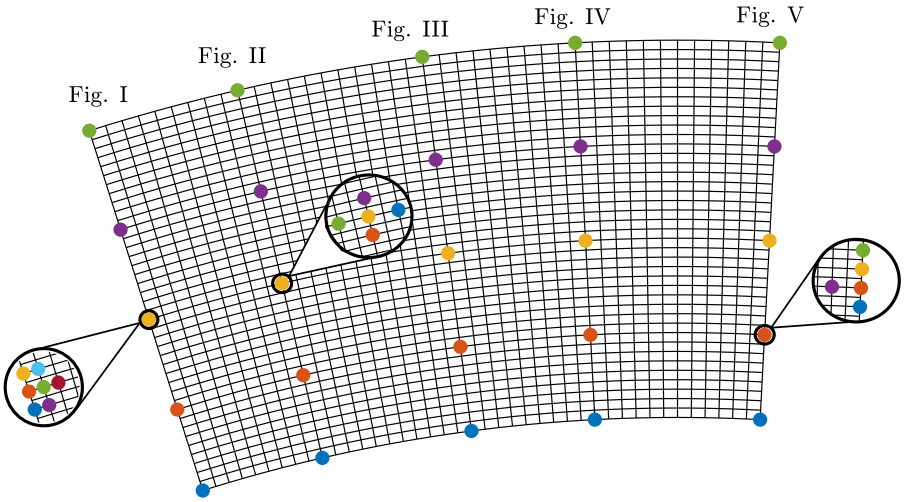

Figure 3.51: Positions where a thorough analysis has been conducted

A thorough analysis has been conducted in those positions in which the low-frequency content is important. After selecting those interesting points where the frequency content at low-frequencies show a complex behaviour, the PSD is applied to the surrounding nodes to see if the phenomena is punctual or it spans a bigger region. In the Figure 3.51 are showed the positions where a deeper evaluation has been done. The different colors in each enlarged region have been selected equal to its corresponding plot. A general comment that can be made about all the graphics showed is that in all of them the second harmonic at $f = 976\,Hz$ is pressent with greater or lesser intensity.

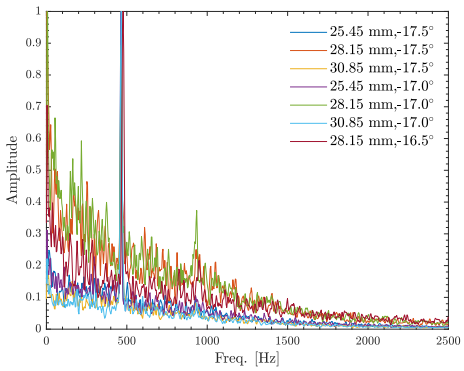

(a) Detail figure I

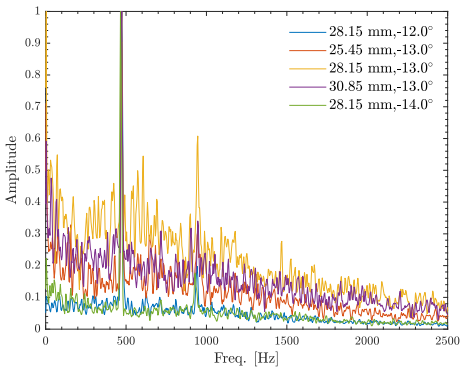

(b) Detail figure II

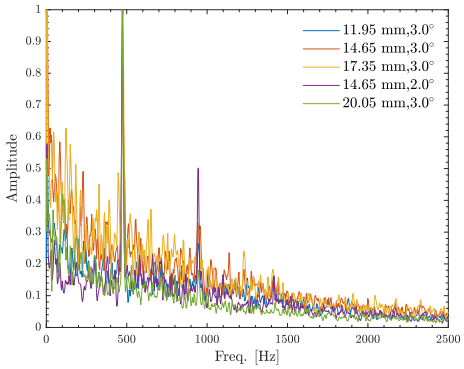

(c) Detail figure V

Figure 3.52: Detailed analysis of the positions marked

In the Figure 3.52a) it can be appreciated that it is in $r = 28.15\,mm$ at any of the three pitch positions where the low-frequency content is located. Besides, those three positions show an important peak at $f \simeq 3 - 4\,Hz$. On the contrary, none of the rest of the positions present that behaviour.

The Figure 3.52b) shows a different pattern, only the points located at pitch $-13.0°$ present a low-frequency content being stronger at $r = 28.15\,mm$ and at a frequency $f \simeq 3 - 4\,Hz$. Whereas the results in the other two positions are normal.

Finally, in the Figure 3.52c) only the positions located at $r = 14.65\,mm$ and $17.35\,mm$ at a pitch $3.0°$ show an important low-frequency content so most probably the phenomena is punctual without spanning to the sorrounding nodes.

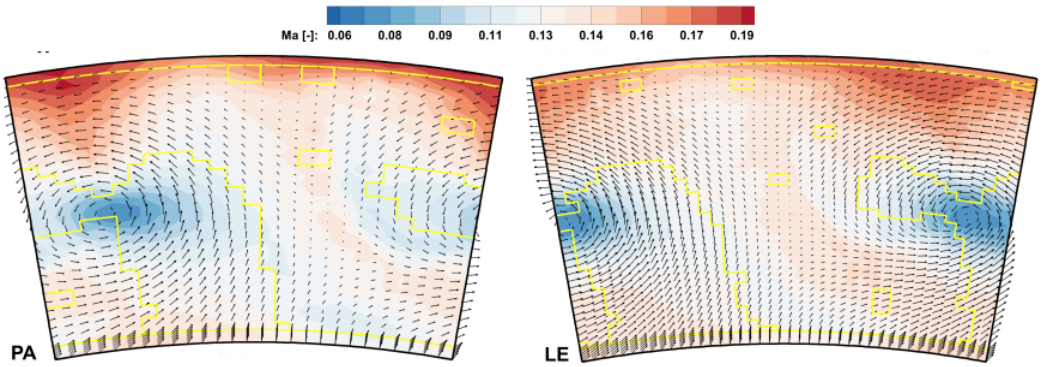

Figure 3.53: Mach contours in $MP40$ [8]

The Figure 3.53 shows the velocity field in terms of Mach number on the plane $MP40$. Both graphics correspond to the two different positions of the combustor simulator. For the data used in this project and therefore treated in the previous analysis, the combustor simulator was in the Passage (PA) position.

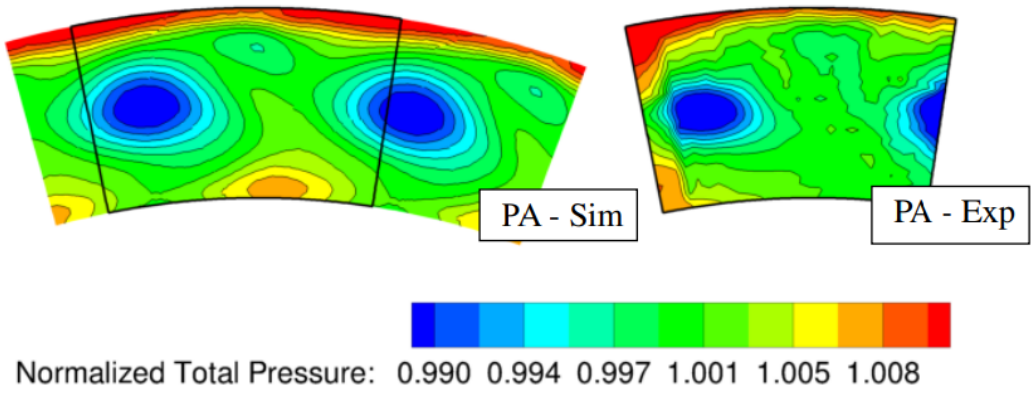

Figure 3.54: Numerical (left) and experimental (right) pressure maps [4]

Taking into account the positions were a thorough spectra analysis has been carried out, it can be observed that the vortex cores position coincides with those locations. In those positions, the low-frequency content can be related to those vortex and the lower speed in those regions. The existence of the vortex clearly affects the pressure field around its position. These results can be confirmed with the pressure contours presented in the Figure 3.54. This graphic shows the numerical and experimental pressure maps where it can be observed the position of the vortex. This vortex notoriously affects the pressure field creating a low-pressure region around the its core.

In the Figure 3.49 it could be observed that the spectra in all the shroud positions (green color) is less energetic in comparison with the rest of the positions. In the Mach contours and in the pressure maps, it can be observed that the shroud is a region with low velocity and high pressure.

The peaks in the spectra range could be related to the swirl introduced by the combustor simulator, as well as the vortex seen in the contour plots showed above. Since the measuring plane was upstream of the rotor stage, the BPF does not appear in the spectra. This is because the swirl of the flow is much stronger than the blade passage disturbance traveling upstream.

3.4.3 mPOD results

After having thoroughly analysed the spectra in those positions where the frequency content seemed to be more interesting, the next step is compute the mPOD. In this case, only the mPOD is applied since the POD has been demonstrated not being suitable for this kind of applications. As it has been commented before, little changes had to be made in the code not only to post-process the pressure field but also because the experimental spatial grid is quite different to the domain of the numerical cases.

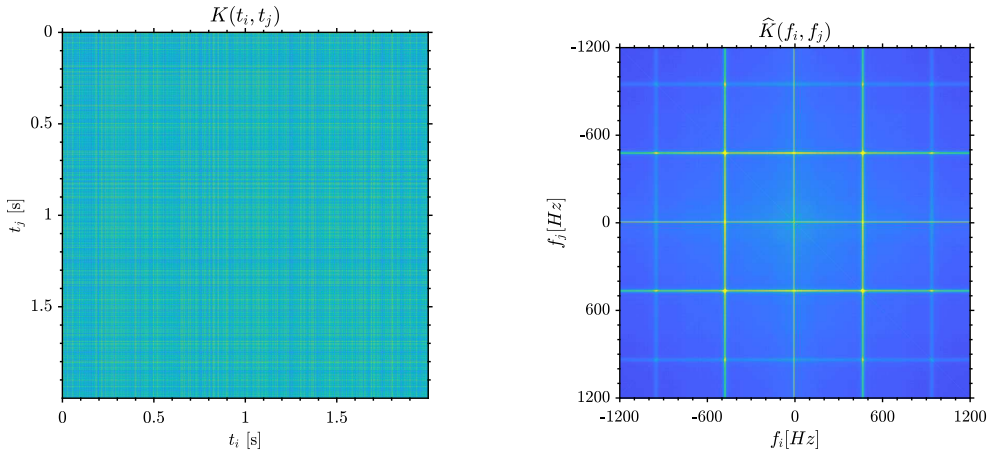

Figure 3.55: Correlation matrix (left) and its spectra (right)

The Figure 3.55 shows the correlation matrix K and its spectra $\hat{K}$. The temporal correlation matrix shows a regular pattern and a broad frequency range. The spectra correlation matrix presents a really strong peak located around $f \simeq 500\,Hz$ and also less important frequency content around $f \simeq 950\,Hz$. These results are consistent with the frequency analysis made in the previous section since all the studied positions showed a similar spectra. Taking this into account, the purpose of isolating the two phenomena leads to define the splitting frequency vector as $F_v = [100, 700, 1100]\,Hz$. This means that the data have been splitted into four scales before computing the decomposition.

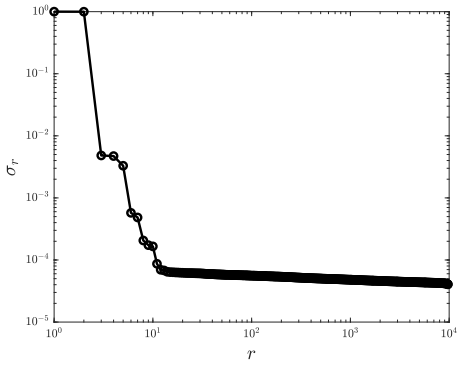

Figure 3.56: Energy content of mPOD modes

The next step after decomposing the data is to analyse the energy content of each mPOD mode. The Figure 3.56 shows this energy evolution normalized with the most energetic mode as well as it has been done previously. Once this modes have been computed, the corresponding temporal structures are shown in the Figure 3.57. This graphics are presented with the same structure as in previous sections even though the temporal evolution of the modes are not easily interpreted. In all the plots, the ordinate axis is dimensionless since it is normalized. Just the most interesting modes are showed.

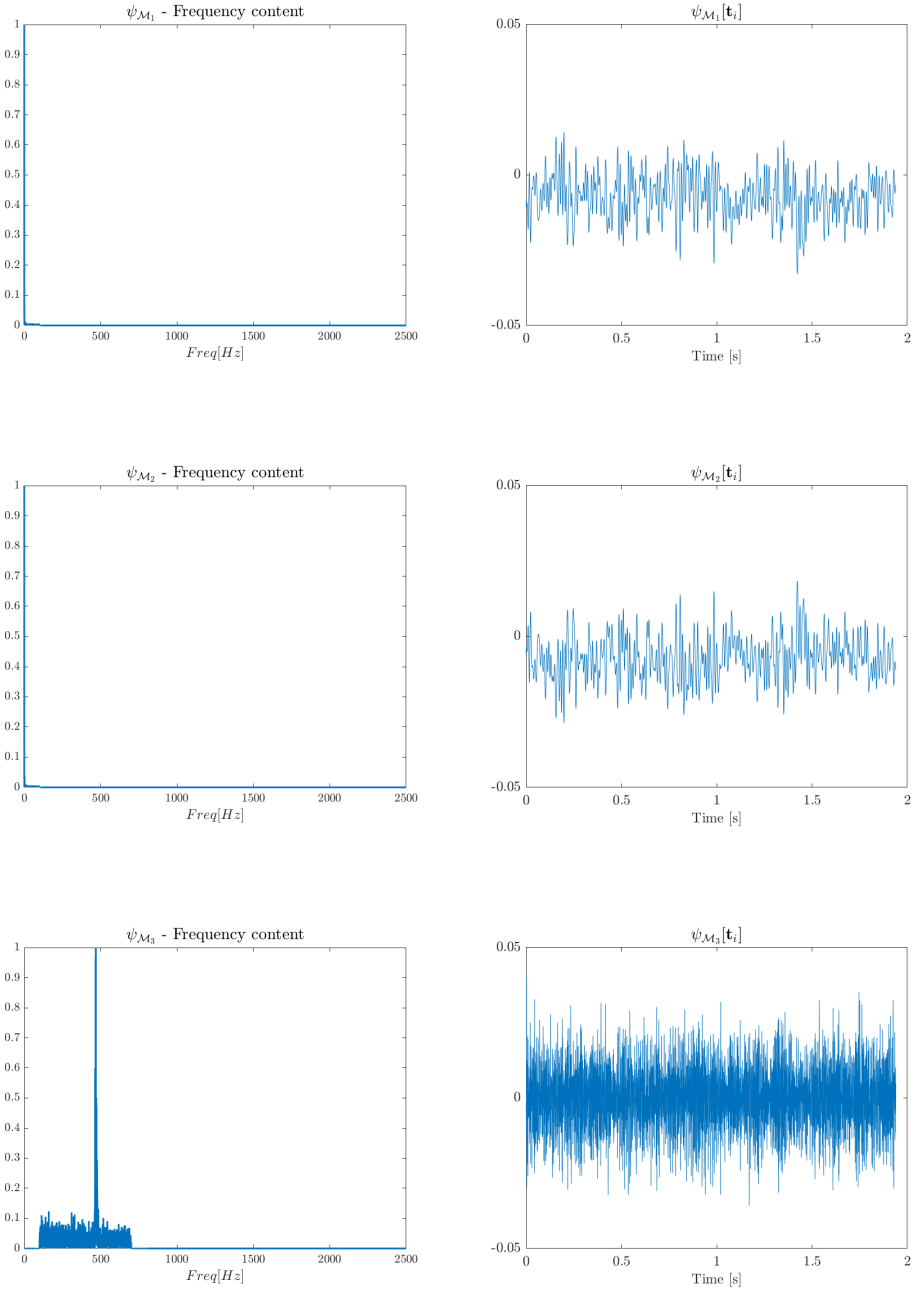

The temporal structures of the two first modes, $\psi_{\mathcal{M}_1}$ and $\psi_{\mathcal{M}_2}$, show a low-frequency content corresponding to the large scale movements. Besides, these two modes are the most energetic ones as it can be seen in the Figure 3.56. The third mode $\psi_{\mathcal{M}_3}$ clearly presents a spectra that corresponds to the second scale between $f = 100 - 700\,Hz$ with a strong peak at $f \simeq 500\,Hz$. This peak was expected since the analysis done showed it as well as the spectra correlation matrix.

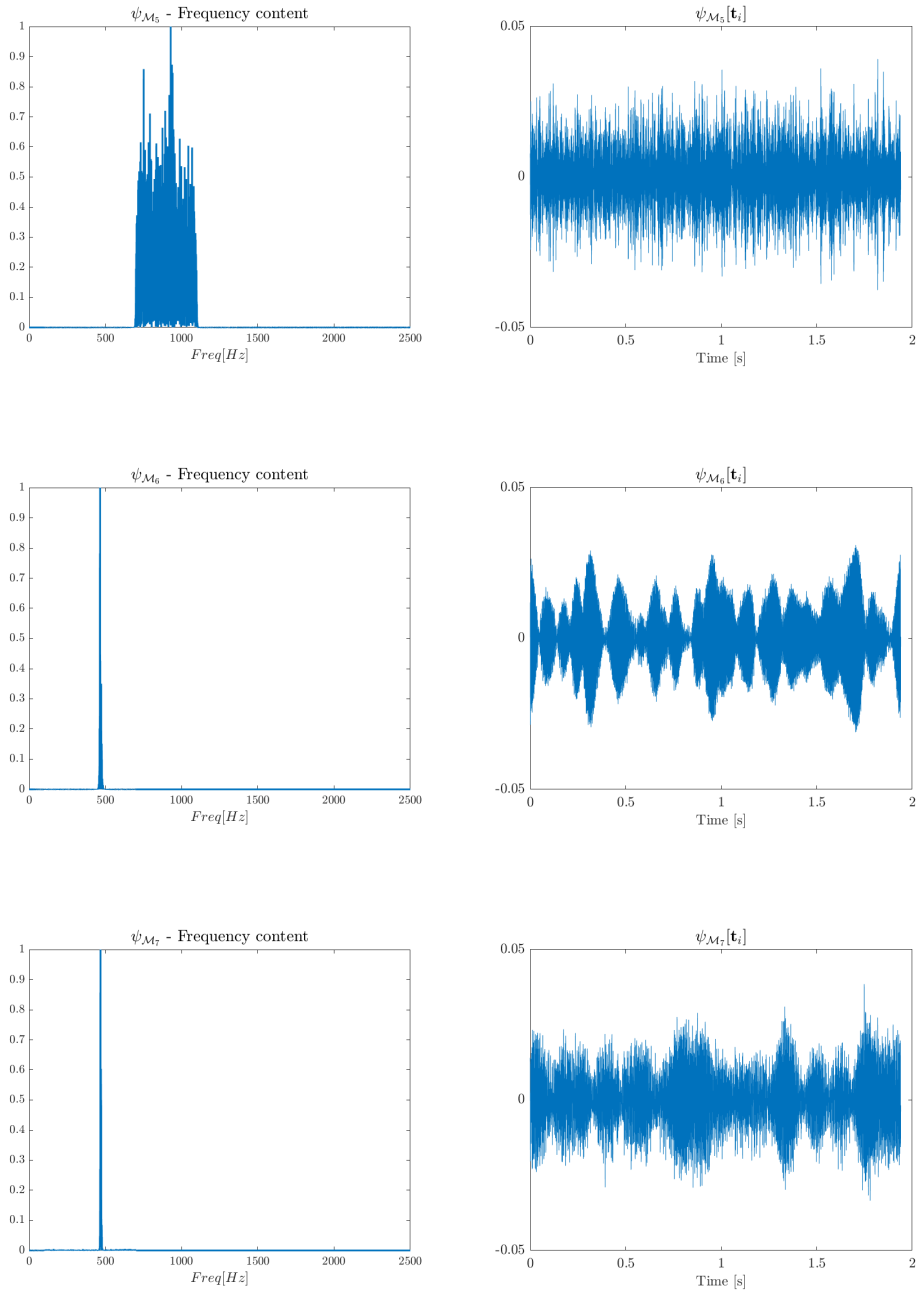

Figure 3.57: mPOD temporal structures

The fifth mode $\psi_{\mathcal{M}_5}$ corresponds to the third scale since its frequency content is limited to $f = 700 - 1100\,Hz$. At $f \simeq 950\,Hz$ it can be observed the most significant peak even though this mode shows a very energetic spectra without any predominant peak over the rest. As it could be observed in the Figures 3.50, 3.52 and 3.55, the harmonic present at this frequency has a low energy content in comparison with the strongest peak. In this mode, this peak is not dominant in the spectra range.

The sixth $\psi_{\mathcal{M}_6}$ and seventh $\psi_{\mathcal{M}_7}$ modes show a dominant peak located at $f \simeq 500\,Hz$. Taking into account the previous results, this two modes could be related to traveling structures and therefore are presented with a $\pi/2$ delay in the phase.

After having commented the temporal structures, the Figure 3.58 shows the spatial structures of the mPOD modes presented above.

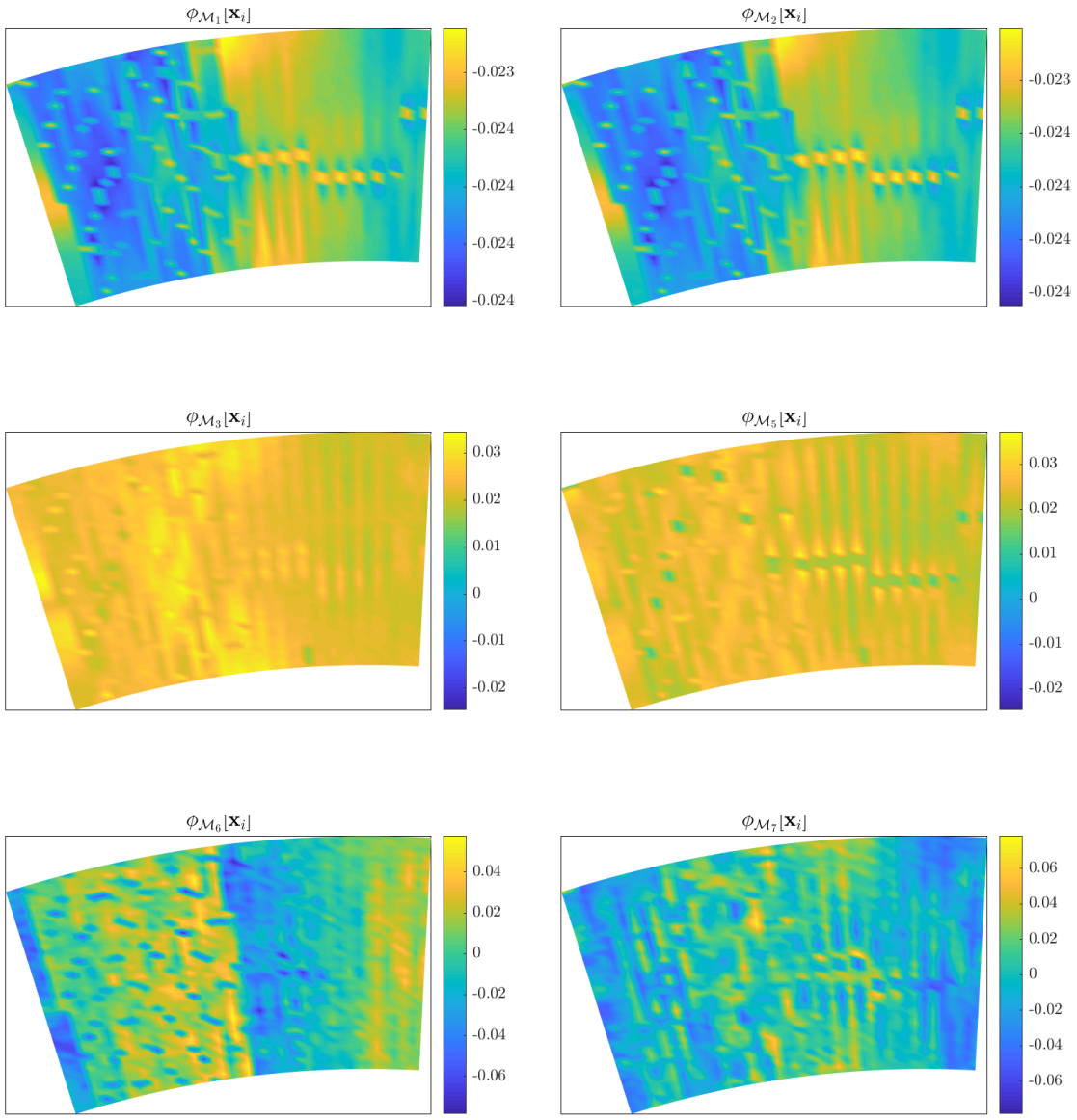

Figure 3.58: Spatial structures of the mPOD modes

It can be observed that the two first modes, $\phi_{\mathcal{M}_1}$ and $\phi_{\mathcal{M}_2}$, present a quite similar structures. On the other hand, even though the sixth $\phi_{\mathcal{M}_6}$ and seventh $\phi_{\mathcal{M}_7}$ mode have the same energy content, their spatial structures are different. All these graphics show somehow a pattern but of very difficult interpretation. Besides, all the spatial structures present unexpected and inconsistent bursts at different locations.

The results interpretation requires a deeper analysis of the experimental data because the two issues mentioned at the end of §3.4.1 could not have completely been solved. Besides, since the code has only been tested with one experimental case it cannot be discarded any coding error. It would be interesting to test the mPOD code with data acquired in different measuring planes to check if the spectra changes and also to confirm that the arisen problems are not due to any error in the acquisition process.

The results showed above are consistents in terms of spectra content. The point-by-point analysis done in the previous section, the spectra of the correlation matrix and the frequency content of the mPOD modes present the same frequency phenomena: the strongest peak at $f \simeq 500\,Hz$ and the harmonic at $f \simeq 950\,Hz$. It is important to remark that any of the mPOD modes show spectral mixing and therefore the pattern recognition is easier. One possible solution could be the refinement of the filter bank to narrow the frequency band-width of each scale and try to reduce the spectra range around the peaks.

Chapter 4

Conclussions and future work

The big-data revolution and the higher computational power have made that in experimental cases as well as in simulating processes, the quantity of saved data has considerably increased. In order to properly and efficiently treat all the data it is necessary to develop the so called data-driven techniques. There is a wide variety of techniques and each one follows different criteria to compute the decomposition. In this project, an extensive review of two techniques has been done. The mathematical basis of POD and mPOD has been reviewed as well as the corresponding matrix form of the decomposition to give to the reader a perspective and an idea of the code developed in MATLAB.

These types of techniques decompose the data in different modes each one composed by a temporal and an structural basis. The mPOD directly derives from the POD fulfilling the optimal energy criteria by which all the modes obtained in the decomposition are arranged in descending order of energy content. It has been commented and later demonstrated the limitations of this type of methods and therefore the necessity of hybrid methods capable of filling the gap between the energy-based and the spectral purity decompositions. Although this last type of methods have not been used in this project, a brief comment of their basis has been done.

The POD and mPOD have been firstly tested with a series of analitycal cases to compare the results of both techniques. In the first synthetic case, same results have been obtained with the two techniques due to the simplicity of the case and the fact that mPOD applies the POD over each scale obtained in the splitting process. If one of the scales contains all the energetic phenomena, both techniques match in their results. Therefore, the splitting of the data in different scales is interesting and useful if each scale contains different energetic phenomena.

For the second case, the same as the first one with added noise, the modes obtained with both decompositions were quite similar. The frequency content of all the modes were the same but the temporal series of the POD modes showed a noisy behaviour that the mPOD modes were capable of filter. This is one of the commented advantages of the mPOD over the POD: the higher filtering capability of the decomposition. In view of the results obtained, in this case the difference is not significant since the possible phenomena present in the data is totally distinguishable. Undoubtedly, this ability of the mPOD is very useful when a real signal is treated and it is pretended to detect significant patterns in the flow field.

In the third case, it has been proved the weaknesses of the energy-based decompositions. This is the POD's inability of differenciating between different phenomena with a similar energy content. Here is where mPOD has demonstrated that the convenience of splitting the data into different scales with a non-overlapping frequency content between them. Whereas the POD modes showed spectral mixing in the temporal structures, the mPOD ones have separated the different phenomena. Once again, this mPOD strength is really useful when real data is treated because two main aspects: not always the most energetic phenomena are the most physically important, and when it is pretended to detect significant structures or interesting patterns the spectral mixing could be limiting.

A different perspective has been tried by testing POD and mPOD on an experimental case of the PIV of an impinging jet. The differences between the code used in this case and the one used for the rest of the cases have been commented and they lie on the different domain in each case. The POD modes showed an spectral mixing in comparison with the modes obtained with mPOD. A general comment for the results obtained in this case and in the rest ones is that the modes related to travelling structures appear in pairs with a phase delay.

When a novel technique like mPOD is developed, there are always some further investigations that can be done in order to test and evaluate its validity. In this way, different and more complex synthetic cases can be set out to check the strengths and limitations of the technique. For sure, also different experimental cases can be tested with the same purpose. One really interesting use of the mPOD would be using it with numerical results from an CFD unsteady simulation takinkg into account that this technique requires the input data being ordered properly.

Since the technique has been coded in MATLAB, a possible work for the future could be the optimization of the code in order to speed up some processes of the code like the experimental file readings. The code is prepared to compute mPOD over the pressure field of an actual turbomachine, but it can also be prepared to treat the velocity or the temperature field.

The emission targets are becoming more restrictive and this is promoting new studies like the FACTOR project. The main goal of this work was improving the numerical and experimental characterization of the flow interface between the combustor and high pressure turbine in a core engine. Several measures of significant variables as well as different numerical simulations were carried out with this purpose. For this Thesis, the experimental data acquired in the FACTOR project has been used and treated. It was necessary to pre-process the raw data before using it to correct some deficiencies like missing data or the initial acquisition time.

A thorough analysis of the frequency content along several positions in the experimental grid has been done where both FFT and PSD techniques were used. This study showed a very strong peak at a frequency different from the BPF due to the measuring plane was located upstream of the rotor and downstream of the combustor simulator. This combustor is composed by a swirling device responsible of this frequency content, at sight of the obtained results. An harmonic of this frequency appears in some positions with less intensity.

After the spectra study, the mPOD was computed and the results are consistent in terms of spectra content since the coorelation matrix shows the same peaks that the previous analysis. In the same way, the spectra of the computed mPOD modes is quite similar since it appears the most significant peak and also the harmonic. The most energetic modes correspond to the large scale structures and therefore they present a very-low frequency content.

As it has been previously commented, even though the temporal structures show expected results, the spatial structures are very difficult to interpret and any clear pattern or structure

is clearly observed. The solution of this issue would require a deeper previous analysis. Also, it could be useful using a better solution for the experimental deficiencies commented. The lack of time it has made impossible checking different solutions or making a more thorough pre-analysis. For future works, it would be interesting analyse the code, since an error in the method cannot be dismissed, as well as testing the mPOD with experimental data acquired on different measuring planes. This would be useful to determine if the arisen problems are not related to the acquisition of the data.

Another possible work for the future could be post-process the data acquired in the rest of the measuring planes in the FACTOR project to see if the mPOD is capable of detecting the unsteady phenomena in different positions along the core engine.

References

[1] Paul G A. Cizmas and Antonio Palacios. "Proper orthogonal decomposition of turbine rotor-stator interaction". In: *Journal of propulsion and power* 19.2 (2003), pp. 268–281.

[2] L.; Schram C.; Lecture Series Directors David. *Advanced post-processing of experimental and numerical data*. Rhode-St-Genese, Belgium: von Karman Institute, 2014. URL: `http://koha.private.vki.eu/articles/`.

[3] Balazs Farkas, Nicolas Van de Wyer, and Jean-Francois Brouckaert. "Numerical Study on the Effect of Seal Leakage Flow on Low Pressure Axial Compressor Performance". In: *ASME Turbo Expo 2013: Turbine Technical Conference and Exposition*. American Society of Mechanical Engineers. 2013, V06AT35A039–V06AT35A039.

[4] F.; et al. Govert S.; Ferraro. *Investigation of combustor-turbine interaction in a rotating cooled transonic high-pressure turbine test rig: part II - Numerical modelling and simulation*. ASME Turbo Expo 2019: Turbomachinery Technical Conference and Exposition. 2019.

[5] Kenneth C Hall, Jeffrey P Thomas, and Earl H Dowell. "Proper orthogonal decomposition technique for transonic unsteady aerodynamic flows". In: *AIAA journal* 38.10 (2000), pp. 1853–1862.

[6] Philip Holmes et al. *Turbulence, coherent structures, dynamical systems and symmetry*. Cambridge university press, 2012.

[7] GRAU Katrin. *Applications of the proper orthogonal decomposition method*. Tech. rep. WN/CFD/07/97, 1997.

[8] C.; et al. Krumme A.; Buske. *Investigation of combustor-turbine interaction in a rotating cooled transonic high-pressure turbine test rig: part I - Experimental results*. ASME Turbo Expo 2019: Turbomachinery Technical Conference and Exposition. 2019.

[9] V-M Lei, ZS Spakovszky, and EM Greitzer. "A criterion for axial compressor hub-corner stall". In: *Journal of Turbomachinery* 130.3 (2008), p. 031006.

[10] John Leask Lumley. "The structure of inhomogeneous turbulent flows". In: *Atmospheric turbulence and radio wave propagation* (1967).

[11] J Marty and B Aupoix. "Interaction of shrouded stator flow and main flow and its influence on performances of a three-stage high pressure compressor". In: *Proceedings of the Institution of Mechanical Engineers, Part A: Journal of Power and Energy* 226.4 (2012), pp. 489–500.

[12] MA Mendez. *An Introduction to Multiscale Data Driven Modal Analysis and Model Reduction*. Seminar in Universidad Carlos III de Madrid. 2019.

[13] MA Mendez. *An Introduction to Reduced Order Modeling and Modal Analysis in Fluid Dynamics*. Lecture Series in Von Karman Institute for Fluid Dynamics. 2018.

[14] MA Mendez, M Balabane, and J-M Buchlin. "Multi-scale proper orthogonal decomposition (mPOD)". In: *AIP Conference Proceedings*. Vol. 1978. 1. AIP Publishing. 2018, p. 060018.

[15] MA Mendez, M Balabane, and J-M Buchlin. "Multi-scale proper orthogonal decomposition of complex fluid flows". In: *Journal of Fluid Mechanics* 870 (2019), pp. 988–1036.

[16] M.A. Mendez, M.T. Scelzo, and J.-M. Buchlin. "Multiscale modal analysis of an oscillating impinging gas jet". In: *Experimental Thermal and Fluid Science* 91 (2018), pp. 256–276. ISSN: 0894-1777. DOI: https://doi.org/10.1016/j.expthermflusci.2017.10.032. URL: http://www.sciencedirect.com/science/article/pii/S0894177717303370.

[17] M.L. Riethmuller and P.; Lecture Series Director Millan. *Post-processing of experimental and numerical data*. 2002.

[18] N Rochuon, I Trébinjac, and G Billonnet. "An extraction of the dominant rotor-stator interaction modes by the use of Proper Orthogonal Decomposition (POD)". In: *Journal of Thermal Science* 15.2 (2006), pp. 109–114.

[19] Peter Welch. "The use of fast Fourier transform for the estimation of power spectra: a method based on time averaging over short, modified periodograms". In: *IEEE Transactions on audio and electroacoustics* 15.2 (1967), pp. 70–73.

[20] Steven R Wellborn. "Details of axial-compressor shrouded stator cavity flows". In: *ASME Turbo Expo 2001: Power for Land, Sea, and Air*. American Society of Mechanical Engineers. 2001, V001T03A078–V001T03A078.